Shape optimization for thermoacoustic instability

with an adjoint Helmholtz solver

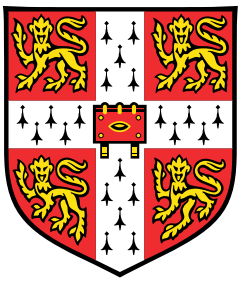

Stefano Falco

Department of Engineering
University of Cambridge

This dissertation is submitted for the degree of
Doctor of Philosophy

Jesus College

August 2021

To my family

Declaration

I hereby declare that except where specific reference is made to the work of others, the contents of this dissertation are original and have not been submitted in whole or in part for consideration for any other degree or qualification in this, or any other university. This dissertation is my own work and contains nothing which is the outcome of work done in collaboration with others, except as specified in the text and Acknowledgements. This dissertation contains fewer than 65,000 words including appendices, bibliography, footnotes, tables and equations and has fewer than 150 figures.

Stefano Falco
August 2021

Acknowledgements

These three and a half years in Cambridge have been the most challenging so far. I have had to learn a lot more about myself, and about thermoacoustics of course. A PhD is a long journey. It requires hard work, a bit of luck and great people.

I cannot begin to express my thanks to my supervisor, Prof Matthew Juniper, who has given me this opportunity. He has always been present and supportive despite my 'slow but steady progress'. He has been an invaluable guide every time I got stuck during my research.

I would also like to extend my deepest gratitude to my Master's thesis supervisor, Prof Flavio Giannetti, without whom I would never have thought of applying to Cambridge.

I also wish to thank Dr Laurent Gicquel for hosting me at CERFACS during my secondment.

Many thanks to my ISO-40 friends-and-colleagues: Alex, Ekrem, Filip, Francesco, Hans, Jack, José, Matthew, Max, Petr, Ubaid and Ushnish - our windowless office is a bit less depressing with you! - and to my Hopkinson Lab friends: Alberto, Antoine, Dante, Hassan, Pau, Roberto and Santi.

To my 'Marie Curie' friends at CERFACS: Abhijeet, Ermanno, Varun and Walter, who have contributed to make my stay in Toulouse so enjoyable.

To my Italian friends at Jesus: Andrea, for all the enlightening conversations, and Francesco. They have been absolutely essential during the COVID-19 pandemic.

And to my best housemates in Park St: Bee, Jed and Shona, one of the best people I know.

I gratefully acknowledge the European Union's Framework Programme for Research and Innovation Horizon 2020 under the Marie Skłodowska Curie grant agreement ANNULIGhT No 765998 for funding this project.

Abstract

Thermoacoustic instabilities, which occur due to the feedback between confined flames and acoustics, constitute a major threat to the safe operation of gas turbines and rocket engines. These oscillations can become large enough to cause noise, vibrations or, in the worst cases, extinction of the flame or structural damage. The fact that thermoacoustic systems are sensitive to small changes to their design and operating parameters means that instabilities can appear in the late stages of the design process, requiring costly re-design. In this thesis we address the problem of finding accurately and at reduced computational cost the design changes that most stabilize a thermoacoustic system in the linear regime.

We derive a Helmholtz equation with an unsteady heat release source and acoustic impedance boundary conditions. We apply the finite element method with P2 elements to discretize the weak formulation of the Helmholtz equation. We obtain a nonlinear eigenvalue problem for the complex angular frequency, ω, that we solve with the open-source computing platform FEniCS and the library for eigenvalue problems SLEPc. We then derive the formulae for the shape derivatives of the eigenvalues of the Helmholtz equation in Hadamard form for different boundary conditions and in the cases of simple and semi-simple degenerate eigenvalues. These formulae allow us to efficiently calculate the effect of arbitrary boundary perturbations on the frequency and growth rate of the thermoacoustic oscillations, by combining the direct and adjoint eigensolutions.

We apply this model and analysis to an electrically heated Rijke tube and a turbulent swirl combustor in 2D. Both systems exhibit an unstable longitudinal mode. We parametrize the shapes using B-splines, calculate the shape derivatives and apply the most stabilizing changes until we make the systems stable.

We then study the case of a 30kW laboratory-scale symmetric annular combustor (MICCA) with an unstable azimuthal mode (two-fold degenerate). We perform a shape sensitivity analysis considering both symmetry-breaking and symmetry-preserving boundary perturbations. The second type of changes do not cause the eigenvalues to split and are the most effective at reducing the instability. We then apply shape changes to the plenum and the combustion chamber to reduce the eigenvalue growth rates.

We show how adjoint-based sensitivity analysis can be combined with a Helmholtz solver to calculate the influence of the shape of the combustor on the stability of the thermoacoustic modes. By modifying the shape accordingly, we are able to suppress the instability or at least reduce the growth rate of the oscillations. This computational method shows how to significantly alter thermoacoustic oscillations by making small geometry changes. The framework in this thesis can handle arbitrarily complex three-dimensional geometries, which could be useful for the design of industrial combustion systems.

Table of contents

List of figures

List of tables

Chapter 1

Introduction

Thermoacoustic instabilities are a major threat to the safe operation of gas turbines and rocket engines. During the combustion process, chemical energy is converted into thermal energy. The fluctuations in the heat release rate excite acoustic waves that in turn interact with the flame (Culick, 2006; Lieuwen and Yang, 2005; Poinsot, 2017). If the pressure and the heat release rate oscillations are sufficiently in phase, then the acoustic energy grows, until is balanced by the energy loss due to damping or acoustic radiation from the boundaries (Rayleigh, 1878). These oscillations can become large enough to cause noise, vibrations or, in the worst cases, extinction of the flame or structural damage (Lieuwen and Yang, 2005). Thermoacoustic systems are sensitive to small changes to their design and operating parameters (Juniper and Sujith, 2018). They can appear in the late stages of the design process (Mongia et al., 2003), requiring costly re-design. Therefore, tools to find accurately and at reduced computational cost the design changes that most stabilize a thermoacoustic system in the linear regime would be desirable. In the preliminary design of aero engines, one of the first objectives is that the system is linearly stable to small perturbations in the operating range. A necessary condition for lineary stability is that the growth rate of the eigenvalues is negative.

Sensitivity analysis gives the influence of small parameter changes on the eigenvalues. Given an eigenvalue and one parameter, we can perturb the parameter, re-calculate the eigenvalue and then find the sensitivity with a finite difference (brute force). For N parameters, we solve the eigenvalue problem $N + 1$ times. Adjoints reduce the number of calculations to 2 (*direct* and *adjoint*), regardless of the number of parameters (Jameson, 2003; Luchini and Bottaro, 2014). This is convenient when the number of parameters is larger than the number of the quantities of interest, which in this case is the number of eigenvalues.

In this thesis it is shown how adjoint-based sensitivity analysis can be combined with a Helmholtz solver to calculate the influence of the shape of the combustor on the stability of

the thermoacoustic modes. By modifying the shape accordingly, we are able to suppress the instability or at least reduce the growth rate of the oscillations.

1.1 Low-order modelling

Experiments and simulations can reveal whether a given combustor is unstable, but they do not tell why it is unstable or how the instability can be controlled. In order to understand why the instabilities appear and how they can be controlled, we need other approaches such as low-order models.

When using low-order modelling, thermoacoustic systems are usually modelled as networks of elements or subsystems of varying geometric and physical complexity. The subsystems, and in particular their input-output relationships, can be characterized analytically, experimentally or numerically.

There are two possible classifications for thermoacoustic low-order models: time domain vs complex frequency domain and Riemann invariants or travelling waves vs modal decomposition. In the time domain, a state-space approach is used (Bothien et al., 2007; Emmert et al., 2016; Schuermans et al., 2003). In the simulation of limit cycles, only time-domain methods are able to retrieve the nonlinear coupling between modes and their dynamics. However, complex impedances are difficult to prescribe in the time domain. The analysis in this thesis is in the frequency domain and is therefore restricted to the linear behaviour of the systems being investigated.

1.1.1 Wave-based approach

A popular method of modelling thermoacoustic systems consists in deriving the Riemann invariants of the linearized Euler equations (LEE), assuming that the flame is compact, i.e. the characteristic length of the flame is short compared to the characteristic acoustic wavelength of the thermoacoustic system. In this way it is possible to include mean-flow effects such as entropy and vorticity waves. Dowling and Stow (2003); Stow and Dowling (2001) and Evesque and Polifke (2002) performed a linear stability analysis of the thermoacoustic network of an annular combustor using a wave-based approach. In both cases, the annular combustor consisted of burners connecting an annular plenum and an annular chamber. The burners were modelled as 1D axial elements. The dependence on the radial coordinate in the plenum and in the combustion chamber was neglected (thin annulus) and the travelling waves were assumed to be periodic in the azimuthal direction. Bauerheim et al. (2014) studied analytically the symmetry-breaking of an idealized annular combustor using a wave-based approach. The

model was quasi-one-dimensional, in the sense that the travelling waves were axial in the burners and azimuthal in the combustion chamber. In subsequent studies, they added an azimuthal mean flow in the combustion chamber (Bauerheim et al., 2015) and investigated the case of symmetry-breaking due to uncertain parameters using uncertainty quantification (UQ) (Bauerheim et al., 2016). Another example is the open-source research software OSCILOS, developed at Imperial College London, which was used to study limit cycles of non-pressurised and pressurised longitudinal combustors using flame describing functions (FDF) obtained from large eddy simulations (LES) (Han et al., 2015; Xia et al., 2019). There is a limit to the complexity of geometries and mode shapes that can be modelled using a wave-based approach, making it unsuitable for our purposes.

1.1.2 Modal expansion

Another method of modelling thermoacoustic systems consists in expanding the solutions of the Helmholtz equation on a modal basis. In the Galerkin method, the basis functions are the acoustic modes, which are solutions of the homogeneous Helmholtz equation with either homogeneous Dirichlet or Neumann boundary conditions. One of the advantages of this basis is that it is orthogonal. The Galerkin decomposition was applied in thermoacoustics for the first time by Zinn and Lores (1971) and by Culick (1988, 2006); Culick and Yang (1995) to study combustion instabilities in liquid rocket engines. It was applied then by Balasubramanian and Sujith (2008) and by Juniper (2011) to study thermoacoustic instabilities in a Rijke tube. Compared to the travelling-wave approach, this method is more prone to numerical errors. In particular, errors arise when attempting to capture velocity discontinuities across a heat source (Gibbs phenomenon). This issue was recently addressed and solved by Laurent et al. (2019) using an overcomplete frame modal expansion. Other modal expansions were used by Noiray et al. (2011) and Ghirardo et al. (2016) to study azimuthal instabilities. The basis functions can also be obtained solving the acoustics with a finite element method (FEM) (Bellucci et al., 2005; Schuermans et al., 2003). In this way it is possible to model non-plane waves in complex three-dimensional geometries.

1.2 Helmholtz solvers

Helmholtz solvers (Camporeale et al., 2011; Nicoud et al., 2007) have the advantage of being able to handle complex three-dimensional geometries. The base flow is set to zero (zero Mach number) and the unsteady heat release is modelled as a distributed acoustic source function of

the acoustic variables. Compared to network models, this approach is more versatile but the size of the problem is larger.

Helmholtz solvers can also be expanded/extended to include a wider range of physical mechanisms. They were combined with flame describing functions to assess combustion instability and study limit cycles in a premixed swirl combustor (Silva et al., 2013) and to perform a weakly nonlinear stability analysis of spinning and standing azimuthal modes in an annular combustor (Laera et al., 2017). Gullaud and Nicoud (2012) studied the effect of perforated plates on the acoustics of annular combustors using a model for the acoustic behaviour of the perforated plates. Giusti et al. (2013) simulated a full annular combustor, with and without flames, analysing the influence of multi-perforated liners modelled assigning an equivalent impedance to the corresponding surfaces. Motheau et al. (2014a) simulated a mixed acoustic-entropy combustion instability in a combustor terminated by a nozzle, using a 'delayed entropy coupled boundary condition' (DECBC) (Motheau et al., 2014b), implemented in a Helmholtz solver. Ni et al. (2018) developed a methodology to include flow–acoustic interactions in a Helmholtz solver, quantifying their impact on the thermoacoustic modes of a real industrial combustor. Mensah et al. (2016) used Bloch functions to efficiently compute the thermoacoustic modes of annular combustion chambers.

The choice of a Helmholtz solver is a trade-off between the ability to model complex three-dimensional geometries and the computational cost. Network models are computationally cheaper. However, in the case of the wave-based approach, they are unable to model complex three-dimensional geometries. Shape optimization has already been implemented in thermoacoustic networks based on Riemann invariants, but this approach is limited to simple geometries. Modal decomposition is able in some cases to model non-plane waves in complex three-dimensional geometries, but the dependence of the solution on the shape is involved.

1.3 Large eddy simulation

Large eddy simulation (LES) simulates the unsteady reacting flow in the combustor with high accuracy, albeit at significant cost (Gicquel et al., 2012; Poinsot, 2017). LES can be used for thermoacoustic combustion instabilities in two ways: brute force LES (Staffelbach et al., 2009; Wolf et al., 2012) and forced open-loop LES (Giauque et al., 2005; Martin et al., 2006). The first method consists in setting a large computational domain, accounting for all the geometrical elements of the engine, matching all the boundary conditions and running the LES to compute the self-excited oscillations. The second computes the flame transfer or describing function (FTF/FDF) of a given flame subjected to acoustic forcing for use in a low-order model or acoustic solver.

1.4 Adjoint-based sensitivity analysis in fluid mechanics

This section is intended as a short review of adjoint methods in hydrodynamic stability. These seminal studies laid the foundations for the application of adjoint methods in thermoacoustics, reviewed in Section 1.5. Hill (1992) studied how to restabilize vortex shedding in the flow past a circular cylinder by adding a second smaller cylinder in the wake of the first. He used the adjoint eigenfunction of the unstable mode to create a map of the sensitivity. The theoretical results of Hill were in good agreement with the experimental and numerical results in (Strykowski and Sreenivasan, 1990), even though they omitted the influence on the steady base flow, which was later introduced by Marquet et al. (2008). In a following study, Hill (1995) used the adjoint eigenfunctions to calculate the receptivity of the Tollmien-Schlichting waves in Blasius boundary layers to time-harmonic forcing by sources of momentum, mass and vorticity and to boundary motions as well as acoustic waves. In a similar fashion, Luchini and Bottaro (1998) calculated the receptivity of the Görtler vortices and Pralits et al. (2000) calculated the sensitivity of two- and three-dimensional disturbances in a compressible boundary layer to changes in wall and momentum forcing. Giannetti and Luchini (2006), calculated the receptivity of an incompressible boundary layer (generation of Tollmien-Schlichting waves) at the leading-edge of a flat plate. Notably, the study by Hill (1992) was revisited by Giannetti and Luchini (2007), who introduced the notion of structural sensitivity in global analysis to determine the wavemaker region, which is the region of local absolute instability[1] (Huerre and Monkewitz, 1990), where the flow is more sensitive to momentum forcing and mass injection. The structural sensitivity gives the spatial perturbation of the governing equations able to produce the greatest eigenvalue drift.

Bottaro et al. (2003) performed a sensitivity analysis of the eigenvalues of the Orr-Sommerfeld operator, describing the stability of exponentially growing disturbances, to non-infinitesimal base flow perturbations in a plane Couette flow. They also calculated the optimal (most destabilizing) base flow perturbation. The analysis was generalized by Marquet et al. (2008), who used a global approach to calculate the sensitivity to base-flow perturbations and for the passive control of globally unstable flows to steady forcing in the form of small control devices. Their results were in qualitative agreement with the experimental results of Strykowski and Sreenivasan (1990).

Tammisola et al. (2014) were the first to calculate the second-order global eigenvalue drift due to spanwise wavy blowing-suction perturbations, combining the adjoint eigenfunction with the first-order global eigenfunction correction. Giannetti et al. (2010) calculated the structural sensitivity of the secondary instability in the wake of a circular cylinder using Floquet theory.

[1] a velocity profile is said to be locally absolutely unstable if localized disturbances spread upstream and downstream and contaminate the entire parallel flow

The articles by Sipp et al. (2010), Luchini and Bottaro (2014), and Camarri (2015) review adjoint methods for flow control of non-reacting fluids in depth.

In the low Mach number limit (the density is temperature-dependent and the pressure is temperature-independent) Qadri (2014); Qadri et al. (2018, 2013) studied structural sensitivity and passive control of the spiral vortex breakdown in swirling flows and of low-density jets, combining the direct and adjoint global modes. In compressible flows, structural and base-flow sensitivity were calculated for an axisymmetric blunt-based afterbody modelling an ideal rocket shape and a sphere (Meliga et al., 2010a) and open-loop control of afterbody flows (Meliga et al., 2010b). For low-Mach number reacting flows, in particular lifted jet diffusion flames, Qadri et al. (2015) combined direct and adjoint global modes to identify the wavemaker region and designed passive strategies to control the oscillations.

1.5 Adjoint-based sensitivity analysis in thermoacoustics

In this section we review adjoint methods, in particular adjoint-based sensitivity analysis, in thermoacoustics, with emphasis on Helmholtz solvers and shape sensitivity analysis and optimization. Magri and Juniper (2013) applied adjoint-based sensitivity analysis to the eigenvalues of a simple thermoacoustic system: a Rijke tube with a hot wire modelled as a time delay system. They calculated both the structural sensitivity and the sensitivity to model parameters such as time delay and position of the hot wire. The structural sensitivity allowed them to find the most stabilizing linear feedback mechanisms. Experiments were conducted in order to validate the theoretical and numerical results (Jamieson et al., 2017; Rigas et al., 2016). The results were in good agreement in the case of an adiabatic mesh, while, in the case of a second hot wire, the growth and decay rates matched but not the frequency. Magri and Juniper (2014) performed a similar analysis for a compact diffusion flame in a duct. They also calculated the receptivity to species injection.

Orchini and Juniper (2016) used the adjoint eigenvector to calculate the sensitivity with respect to the convection speed parameter of a thermoacoustic network with a laminar conical premixed flame. The sensitivity analysis of a low-order thermoacoustic network using a wave-based approach was performed in Aguilar et al. (2017), first considering a zero Mach number mean flow and then removing this hypothesis and adding a moving flame and a choked outlet. The same authors applied adjoint-based sensitivity analysis and gradient-based optimization to network models of a longitudinal (Aguilar and Juniper, 2020) and an annular combustor (Aguilar and Juniper, 2018), managing to stabilize all the modes by making small changes to the geometry.

Adjoint methods were also used for speeding up uncertainty quantification in thermoacoustic systems. First- and second-order perturbations in nonlinear degenerate eigenvalue problems (Magri et al., 2016a) were used in the network model of an annular combustor (Magri et al., 2016b).

The first *adjoint thermoacoustic Helmholtz solvers* were used for uncertainty quantification in a longitudinal combustor with second-order single-parameter perturbation theory in (Silva et al., 2017) and with second-order multi-parameter perturbation theory in (Mensah et al., 2018a), and for the optimal placement and tuning of acoustic dampers in an annular combustor (Mensah and Moeck, 2017), using first-order multi-parameter perturbation theory).

Mensah et al. (2019a) studied the effects of symmetry-breaking on the thermoacoustic modes of a rotationally symmetric annular combustor using high-order degenerate perturbation theory and using the same high-order perturbation theory Orchini et al. (2020a) identified the exceptional points (Mensah et al., 2018b; Orchini et al., 2020b), which correspond to defective eigenvalues, in the thermoacoustic spectrum of a longitudinal and an annular combustor.

Mensah et al. (2019b) performed a preliminary shape sensitivity analysis of a Rijke tube using a parameter-free approach and a three-dimensional Helmholtz solver. They computed the eigenvalue shape derivatives for prescribed nodal displacements at the inlet and outlet boundaries. Falco and Juniper (2021a) performed shape optimization of a Rijke tube and a turbulent swirl combustor using a parametric approach and a two-dimensional Helmholtz solver. By applying small geometry modifications, they managed to stabilize both systems. Unlike the method applied by Mensah et al. (2019b), the method of Falco and Juniper (2021a) provides gradient information, i.e. the most sensitive regions. Unlike shape derivatives, the gradient is independent of the particular direction of the perturbation.

The theory, numerical methods and technical challenges of developing adjoint thermoacoustic Helmholtz solvers were detailed in (Juniper, 2018) for the one-dimensional case. An in-depth review of the use of adjoints in thermoacoustics can be found in (Magri, 2019).

1.6 Shape sensitivity and optimization for eigenvalue stability

In this section we briefly review shape optimization and shape sensitivity of eigenvalues in hydrodynamic stability problems. The goal, as in thermoacoustics, is to evaluate the influence of the shape on the frequency and growth rate of the unstable modes. This constitutes a starting point, as well as a reference, for this thesis. Heuveline and Strauß (2009) applied shape optimization for hydrodynamic stability to the eigenvalues of the linearized Navier-Stokes

equations. They studied the flow around a bluff body in a channel. They minimized the drag force, constraining the volume and ensuring that the eigenvalues were stable. The resulting bodies were long and flat. The shape was parametrized using Bézier curves, and the shape derivatives were calculated with finite difference.

Nakazawa and Azegami (2016) were the first to apply adjoint-based shape optimization for stability. They studied a two-dimensional Poisuille flow in a channel with a sudden expansion. The critical Reynolds number was increased from 40 to 45. They applied a smoothing (traction) method to the shape gradients. With a similar approach, Kiriyama et al. (2018) stabilized the global mode of the flow in the wake of a cylinder. More recently, Boujo et al. (2019) used adjoints to calculate the second-order sensitivity of the eigenvalues to wall deformations in a laminar flow around a cylinder. They found the optimal wall deformations to stabilize the flow.

Brewster and Juniper (2020) developed a method to calculate the shape gradients of the frequency and the growth rate of unstable eigenvalues obtained from global stability analysis. They applied the method to the problem of the flow around a cylinder at $Re = 50$. They showed that the deformations affect the hydrodynamic oscillations mainly through their effect on the steady base flow and that subtle deformations at the rear of the cylinder have a large effect on the growth rate. Martinez-Cava et al. (2020) developed a method to calculate the shape gradients of the least stable global mode of the steady compressible Navier-Stokes and the Reynolds-averaged Navier-Stokes (RANS) equations using a discrete approach. They studied two cases: a laminar flow around a cylinder and a turbulent flow to control the buffet onset on a NACA0012 airfoil, and suppressed the instabilities.

In microfluidics, Kungurtsev and Juniper (2019) optimized the design of an inkjet printhead applying adjoint-based shape optimization. They increased the decay rate of the oscillating flow of 50% while keeping the viscous dissipation of the steady flow constant. They used B-splines to parametrize the shape.

1.7 Summary of the thesis

Shape sensitivity analysis for eigenvalue stability has only recently been applied in thermoacoustics using a wave-based approach (Aguilar and Juniper, 2018, 2020). Unlike thermoacoustic networks, Helmholtz solvers have the advantage of being able to handle complex three-dimensional geometries. Adjoint-based sensitivity analysis for perturbations applied to the operator is easy to implement when using the finite element method and it has been widely explored in recent years (Mensah, 2019). Shape sensitivity analysis for eigenvalue stability has the same advantages. The difference is that the perturbations are applied to the domain and

the boundary conditions. This problem has been studied in hydrodynamic stability but not in thermoacoustics.

In this thesis, we develop the theory to efficiently calculate the first-order shape sensitivity and the shape derivatives of the eigenvalues of the thermoacoustic Helmholtz equation. In Chapter 2 we derive the Helmholtz equation with unsteady heat release, the flame response to acoustics, the boundary conditions and the Rayleigh criterion. In Chapter 3 we derive the weak formulation of the Helmholtz equation, apply the finite element method to discretize the weak form and derive the adjoint equation in its continuous and discrete form. We dedicate the last part of the chapter to the eigensolvers used to solve the nonlinear eigenvalue problem arising from the finite element discretization. In Chapter 4 we introduce the basic concepts and definitions of the shape derivatives and derive the formulae for the shape derivatives of the eigenvalues of the Helmholtz equation for different boundary conditions and in the cases of simple and semi-simple degenerate eigenvalues. In Chapter 5 we apply the theory developed in the previous chapters to two thermoacoustic systems: an electrically heated Rijke tube and a turbulent swirl combustor. We parametrize the shape using B-splines, calculate the shape derivatives and apply the most stabilizing changes until we eventually stabilize the systems. In Chapter 6 we study the case of a symmetric annular combustor with an unstable azimuthal mode (two-fold degenerate). We first perform a shape sensitivity analysis considering symmetry-breaking boundary perturbations. Then we perform the same analysis considering symmetry-preserving boundary perturbations. The second type of changes do not cause the eigenvalues to unfold and are the most effective at reducing the instability. We then apply shape changes to the plenum and the combustion chamber to reduce the eigenvalue growth rates. In Chapter 7, we draw some conclusions and suggest possible directions for future work. Appendix A contains a summary of the first-order perturbation theory used to speed up and the eigensolver and Appendix B contains some of the relevant definitions on B-splines curves.

Chapter 2

Thermoacoustic Helmholtz equation

2.1 Helmholtz equation for reacting flows

We start by considering a compressible, reacting, inviscid flow. The fluid is a homogeneous gas mixture, modelled as a calorically perfect gas. We write the mass, momentum and energy equations in convective form

$$\frac{\mathrm{D}\rho}{\mathrm{D}t} + \rho\boldsymbol{\nabla}\cdot\boldsymbol{u} = 0 \tag{2.1a}$$

$$\rho\frac{\mathrm{D}\boldsymbol{u}}{\mathrm{D}t} + \boldsymbol{\nabla}p = 0 \tag{2.1b}$$

$$\rho\frac{\mathrm{D}e}{\mathrm{D}t} + p\boldsymbol{\nabla}\cdot\boldsymbol{u} = \dot{q} \tag{2.1c}$$

And the equation of state

$$p = \rho r T \tag{2.2}$$

ρ is the density, $\boldsymbol{u}$ is the velocity, p is the pressure and T is the temperature. e is the internal energy per unit mass and $\dot{q}$ is the heat release rate per unit volume. $\mathrm{D}(\cdot)/\mathrm{D}t = \partial(\cdot)/\partial t + \boldsymbol{u}\cdot\boldsymbol{\nabla}(\cdot)$, is the material derivative. In addition, $r = c_p - c_v$, is the specific gas constant and $\gamma = c_p/c_v$, is the heat capacity ratio, where c_p and c_v are the specific heats at constant pressure and volume, respectively. For a calorically perfect gas, the specific heats are constant.

We take the total derivative[1] of Eq. (2.2)

$$\frac{\mathrm{d}p}{p} = \frac{\mathrm{d}\rho}{\rho} + \frac{\mathrm{d}T}{T} \tag{2.3}$$

[1] or differential, not to be confused with the material derivative

We recall the definition of specific enthalpy

$$h = e + \frac{p}{\rho} \tag{2.4}$$

And write it in differential form

$$\mathrm{d}h = \mathrm{d}e + \frac{1}{\rho}\,\mathrm{d}p - \frac{p}{\rho^2}\,\mathrm{d}\rho \tag{2.5}$$

For a calorically perfect gas

$$\mathrm{d}h = c_p\,\mathrm{d}T \tag{2.6}$$

Combining Eqs. (2.3), (2.5) and (2.6), we obtain

$$\mathrm{d}e = \frac{1}{\gamma - 1}\left(\frac{1}{\rho}\,\mathrm{d}p - \frac{p}{\rho^2}\,\mathrm{d}\rho\right) \tag{2.7}$$

We substitute Eq. (2.7) into Eq. (2.1c), taking the material derivatives instead of the differentials, and subtract Eq. (2.1a). We obtain the energy equation for the pressure

$$\frac{\mathrm{D}p}{\mathrm{D}t} + \gamma p \boldsymbol{\nabla} \cdot \boldsymbol{u} = (\gamma - 1)\dot{q} \tag{2.8}$$

We write the fundamental thermodynamic relation for the specific internal energy

$$\mathrm{d}e = T\,\mathrm{d}s + \frac{p}{\rho^2}\,\mathrm{d}\rho \tag{2.9}$$

where s is the specific entropy. We substitute Eq. (2.9) into Eq. (2.1c) and subtract Eq. (2.1a). We obtain a conservation law for the entropy

$$\frac{\mathrm{D}s}{\mathrm{D}t} = \frac{r}{p}\dot{q} \tag{2.10}$$

We want to study the evolution of small perturbations superimposed on top of a zero Mach number base flow. The flow variables are decomposed as $(\cdot)(\boldsymbol{x},t) = \bar{(\cdot)}(\boldsymbol{x}) + \epsilon(\cdot)'(\boldsymbol{x},t)$, with $\epsilon \ll 1$. The bar, $\bar{(\cdot)}$, denotes a steady mean quantity and the prime, $(\cdot)'$, an unsteady perturbation quantity. For the velocity, $\bar{\boldsymbol{u}} = 0$, and $\boldsymbol{u} = \boldsymbol{u}'$, with $\sqrt{\boldsymbol{u}' \cdot \boldsymbol{u}'}/\bar{c}$ of order ϵ. $\bar{c} = \sqrt{\gamma\bar{p}/\bar{\rho}}$, is the mean speed of sound. According to the order-of-magnitude analysis in (Nicoud et al., 2007), the zero Mach number assumption is valid if $M \ll L_f/L_a$, where M is the Mach number, L_f is the flame thickness and L_a is the acoustic wavelength. We linearize the momentum, energy and entropy equations, Eqs. (2.1b), (2.8) and (2.10). At order ϵ^0 (zeroth order), we obtain $\boldsymbol{\nabla}\bar{p} = 0$,

and $\bar{\dot{q}} = 0$. The mean pressure is constant and the steady effect of the flame is contained in the mean density field, $\bar{\rho}$. At order ϵ^1 (first order), the equations are

$$\frac{\partial \boldsymbol{u}'}{\partial t} + \frac{1}{\bar{\rho}}\boldsymbol{\nabla} p' = 0 \tag{2.11a}$$

$$\frac{\partial p'}{\partial t} + \gamma \bar{p}\boldsymbol{\nabla}\cdot\boldsymbol{u}' = (\gamma - 1)\dot{q}' \tag{2.11b}$$

$$\frac{\partial s'}{\partial t} + \boldsymbol{u}'\cdot\boldsymbol{\nabla}\bar{s} = \frac{r}{\bar{p}}\dot{q}' \tag{2.11c}$$

We write the fundamental thermodynamic relation for the specific enthalpy

$$\mathrm{d}h = T\,\mathrm{d}s + \frac{1}{\rho}\,\mathrm{d}p \tag{2.12}$$

Combining (2.12) with (2.6), we obtain

$$\mathrm{d}s = c_p\frac{\mathrm{d}T}{T} - r\frac{\mathrm{d}p}{p} \tag{2.13}$$

Taking the gradients instead of the differentials, we obtain for the mean quantities (zeroth order)

$$\boldsymbol{\nabla}\bar{s} = c_p\frac{\boldsymbol{\nabla}\bar{T}}{\bar{T}} = -c_p\frac{\boldsymbol{\nabla}\bar{\rho}}{\bar{\rho}} \tag{2.14}$$

From Eq. (2.11c), we see that entropy fluctuations (hot spots) are generated in the reaction zone, even ignoring the unsteady effect of the flame, i.e. $\dot{q}' = 0$. In fact, from Eq. (2.14), the mean entropy gradient is proportional to the mean temperature (density) gradient and, at least in the reaction zone, the mean temperature gradient is not orthogonal to the velocity fluctuations. Therefore, the second term in Eq. (2.11c) is not zero and there is generation of entropy fluctuations. However, under the assumption of zero Mach number base flow, the entropy fluctuations do not propagate, and therefore do not modify the fluctuating quantities downstream of the flame (Nicoud and Wieczorek, 2009).

If we take $\partial(2.11\text{b})/\partial t - \gamma\bar{p}\boldsymbol{\nabla}\cdot(2.11\text{a})$, we obtain an inhomogeneous wave equation for the pressure perturbation

$$\frac{\partial^2 p'}{\partial t^2} - \boldsymbol{\nabla}\cdot\left(\bar{c}^2\boldsymbol{\nabla}p'\right) = (\gamma - 1)\frac{\partial \dot{q}'}{\partial t} \tag{2.15}$$

It is worth mentioning that we can model distributed acoustic losses due to damping by adding a term proportional to $\partial p'/\partial t$ to the left-hand side of Eq. (2.15). We use the method of

separation of variables, assuming that the fluctuations are harmonic in time

$$(\cdot)'(\boldsymbol{x},t) = \mathrm{Re}\left\{\hat{(\cdot)}(\boldsymbol{x})e^{-i\omega t}\right\} \tag{2.16}$$

where ω is the complex angular frequency. The real part of ω is the angular frequency and the imaginary part is the growth rate. The momentum equation in the complex frequency domain then reads

$$-i\omega\hat{\boldsymbol{u}} + \frac{1}{\bar{\rho}}\boldsymbol{\nabla}\hat{p} = 0 \tag{2.17}$$

From Eq. (2.15) we obtain an inhomogeneous Helmholtz equation

$$\boldsymbol{\nabla}\cdot\left(\bar{c}^2\boldsymbol{\nabla}\hat{p}\right) + \omega^2\hat{p} = i\omega(\gamma-1)\hat{q} \tag{2.18}$$

The complex angular frequency, ω, is the eigenvalue and the pressure perturbation, $\hat{p}$, is the eigenfunction of Eq. (2.18). An eigenvalue is linearly unstable if the growth rate is positive.

2.2 Flame response

The focus of this section is the unsteady heat release rate perturbation term, $\dot{q}'$, in the time domain, Eq. (2.15), and $\hat{q}$, in the complex frequency domain, Eq. (2.18). We model the flame as a linear time-invariant (LTI) system, with an associated transfer function. The flame transfer function (FTF) models the input-output relationship between velocity fluctuations and heat release rate fluctuations. The input can also be fluctuations of pressure or equivalence ratio. In premixed flames, the heat release rate depends on the flame surface, which is mainly controlled by the fresh gas flow rate (Nicoud et al., 2007). For this reason, we will only consider FTFs that have velocity fluctuations as input. Examples of FTF are widely available in the literature. They are derived theoretically for laminar premixed flames (Cuquel et al., 2013; Schuller et al., 2003), laminar non-premixed flames (Magina et al., 2013; Magina and Lieuwen, 2016) and turbulent premixed swirling flames (Candel et al., 2014; Palies et al., 2011b). They can also be obtained from experiments and simulations, in particular LES (Merk et al., 2019) and DNS (Mejia et al., 2018). Nonlinear effects such as saturation, which is responible for the establishment of limit cycles, can be modelled with the so-called flame describing function (FDF) (Dowling, 1997; Noiray et al., 2008), which depends on the amplitude of the perturbation as well as on the frequency.

During the experiments, we measure the frequency response (gain and phase) of the flame to velocity perturbations. The flame is subjected to harmonic excitations, with the forcing signal neither growing nor decaying. In this way, we obtain the flame response at real-valued

frequencies (the frequency response). If the amplitude of the forcing signal is small, then the response is linear. On the other hand, if the amplitude is big, the response is nonlinear. We want to extrapolate the frequency response data, measured at real-valued frequencies, into the complex plane. This will give the flame transfer function.

For the linear response of the flame to velocity perturbations, we adopt a formulation that is similar to the adaptation proposed in (Juniper, 2018). The local heat release rate perturbation, $\hat{q}$, is proportional to the weighted integral of the the component of the velocity perturbation, $\hat{\boldsymbol{u}}$, along the unit vector $\boldsymbol{n}_r$ (reference direction), in the reference region.

$$\hat{q} = \frac{\dot{Q}_t}{U_b} v(\boldsymbol{x}) F(\omega) \int w(\boldsymbol{\xi}) \hat{\boldsymbol{u}}(\boldsymbol{\xi}) \cdot \boldsymbol{n}_r \, \mathrm{d}V \tag{2.19}$$

where $\int v \, \mathrm{d}V = \int w \, \mathrm{d}V = 1$. $\dot{Q}_t$ is the total thermal power of the flame and U_b is the bulk flow velocity in the injector. v is the heat release rate distribution, $F(\omega)$ is the flame transfer function and w is a weight function, which is non-zero in the reference region. If for example the weight function, w, is the Dirac delta function, δ_D, we obtain

$$\hat{q} = \frac{\dot{Q}_t}{U_b} v(\boldsymbol{x}) F(\omega) \int \delta_D(\boldsymbol{\xi} - \boldsymbol{x}_r) \hat{\boldsymbol{u}}(\boldsymbol{\xi}) \cdot \boldsymbol{n}_r \, \mathrm{d}V = \frac{\dot{Q}_t}{U_b} v(\boldsymbol{x}) F(\omega) \hat{\boldsymbol{u}}(\boldsymbol{x}_r) \cdot \boldsymbol{n}_r \tag{2.20}$$

$\hat{\boldsymbol{u}}(\boldsymbol{x}_r) \cdot \boldsymbol{n}_r$ is the component of the velocity perturbation along the unit vector $\boldsymbol{n}_r$, evaluated at the reference point $\boldsymbol{x}_r$. The global heat release rate perturbation is given by

$$\hat{Q} = \int \hat{q} \, \mathrm{d}V = \frac{\dot{Q}_t}{U_b} F(\omega) \hat{\boldsymbol{u}}(\boldsymbol{x}_r) \cdot \boldsymbol{n}_r \tag{2.21}$$

We combine Eq. (2.19) with the linearized momentum equation written in the complex frequency domain, Eq. (2.17), to obtain the flame response as a function of the pressure gradient, and substitute into Eq. (2.18).

$$\boldsymbol{\nabla} \cdot \left(\bar{c}^2 \boldsymbol{\nabla} \hat{p} \right) + \omega^2 \hat{p} = \frac{\dot{Q}_t}{U_b} (\gamma - 1) v(\boldsymbol{x}) F(\omega) \int w(\boldsymbol{\xi}) \frac{1}{\bar{\rho}(\boldsymbol{\xi})} \boldsymbol{\nabla} \hat{p}(\boldsymbol{\xi}) \cdot \boldsymbol{n}_r \, \mathrm{d}V \tag{2.22}$$

We combine Eq. (2.20) with Eq. (2.17) and substitute into Eq. (2.18).

$$\boldsymbol{\nabla} \cdot \left(\bar{c}^2 \boldsymbol{\nabla} \hat{p} \right) + \omega^2 \hat{p} = \frac{\dot{Q}_t}{U_b} \frac{\gamma - 1}{\bar{\rho}(\boldsymbol{x}_r)} v(\boldsymbol{x}) F(\omega) \boldsymbol{\nabla} \hat{p}(\boldsymbol{x}_r) \cdot \boldsymbol{n}_r \tag{2.23}$$

Both Eqs. (2.22) and (2.23) will be used in the remainder of this thesis. In Section 2.2.1 and 2.2.2, we will use the following notational conventions: either $u' = \boldsymbol{u}'(\boldsymbol{x}_r, t) \cdot \boldsymbol{n}_r$ or $u' = \int w(\boldsymbol{\xi}) \boldsymbol{u}'(\boldsymbol{\xi}, t) \cdot \boldsymbol{n}_r \, \mathrm{d}V$, and either $\hat{u} = \hat{\boldsymbol{u}}(\boldsymbol{x}_r) \cdot \boldsymbol{n}_r$ or $\hat{u} = \int w(\boldsymbol{\xi}) \hat{\boldsymbol{u}}(\boldsymbol{\xi}) \cdot \boldsymbol{n}_r \, \mathrm{d}V$.

2.2.1 $n - \tau$ model

In the $n - \tau$ model, originally proposed by Crocco and Cheng (1956), the heat release rate fluctuation at time t is proportional to the axial component of the velocity fluctuation at a point in the injector at time $t - \tau$. In the time domain, the global heat release rate perturbation[2] reads

$$\dot{Q}' = nu'(t - \tau) \tag{2.24}$$

$n = \dot{Q}_t / U_b N$ is the dimensional interaction index, where N is the nondimensional interaction index, and τ is the time delay. In the complex frequency domain, the local heat release rate perturbation is

$$\hat{q} = \frac{\dot{Q}_t}{U_b} v(\boldsymbol{x}) N e^{i\omega\tau} \hat{u} \tag{2.25}$$

Both N and τ can depend on the position, $\boldsymbol{x}$, for example when obtained from large eddy simulation. Here the spatial dependence of N is included in v.

If we compare Eq. (2.25) with Eq. (2.19) or Eq. (2.20), we see that N is the gain and $\omega\tau$ is the phase of the flame transfer function. The fact that the gain is constant with respect to the frequency is only a rough approximation. In fact, flames are sensitive to low-frequency perturbations and attenuate high-frequency perturbations, thereby acting as low-pass filters. At low frequencies, the slope of the phase can be assumed to be constant.

2.2.2 State-space representation

In this subsection we describe how to obtain an analytic flame transfer function from an experimental frequency response. The frequency response is given at real-valued frequencies, while the transfer function is defined in the complex plane. We want to approximate the experimental data on the real axis and extrapolate them into the complex plane. One big advantage of the transfer function being analytic is that we can calculate its exact derivatives with respect to the complex angular frequency ω. This is important when applying perturbation theory.

Following (Mensah et al., 2019a), we approximate the frequency response of the flame with a continuous time-invariant linear state-space model

$$\begin{cases} \dfrac{\mathrm{d}}{\mathrm{d}t}\mathbf{x} = \mathbf{A}\mathbf{x} + \mathbf{b}u' \\ \dot{q}' = \mathbf{c}^T\mathbf{x} + du' \end{cases} \tag{2.26}$$

[2] $\dot{Q}' = \int \dot{q}' \, \mathrm{d}V$

where $\mathbf{x}$ is the state vector, u' is the input and $\dot{q}'$ is the output. The first equation is the state equation and the second is the output equation. We Laplace transform[3] Eq. (2.26) and substitute the state vector from the state equation into the output equation. The output equation now reads

$$\hat{q} = \underbrace{\left[\mathbf{c}^T\left(-i\omega\mathbf{I} - \mathbf{A}\right)^{-1}\mathbf{b} + d\right]}_{F(\omega)}\hat{u} \tag{2.27}$$

In Eq. (2.27), $\hat{q}$ and $\hat{u}$ are to be intended as scaled by $\dot{Q}_t$ and U_b, respectively. The parameters of the state-space model are identified by applying the Vector Fitting algorithm (Gustavsen, 2006; Gustavsen and Semlyen, 1999) This is a well-known technique that has already been used in thermoacoustics in a number of studies, the first being (Bothien et al., 2007), for the characterization of acoustic subsystems in time domain modelling.

2.3 Boundary conditions

In acoustics, the impedance is a measure of how much flow fluctuations are impeded when pressure fluctuations act on a surface. The specific acoustic impedance is defined as the nondimensional ratio of the acoustic pressure to the normal component of the acoustic velocity (Rienstra and Hirschberg, 2004).

$$Z = \frac{\hat{p}}{\bar{\rho}\bar{c}\hat{\boldsymbol{u}}\cdot\boldsymbol{n}} \tag{2.28}$$

where $\boldsymbol{n}$ denotes the outward unit normal. In general, Z depends on the position and on the frequency. If we combine Eq. (2.28) with the linearized momentum equation in the complex frequency domain, Eq. (2.17), we obtain the Robin boundary condition

$$\boldsymbol{\nabla}\hat{p}\cdot\boldsymbol{n} - \frac{i\omega}{\bar{c}Z}\hat{p} = 0 \tag{2.29}$$

We can assume that the impedance is constant at low frequencies (Levine and Schwinger, 1948). For plane acoustic waves, the impedance can be expressed as a function of the reflection coefficient, which is defined as the ratio of the amplitude of the reflected wave to the amplitude of the incident wave.

$$Z = \frac{1+R}{1-R} \tag{2.30}$$

We can derive other boundary conditions as special cases of Eq. (2.29).

[3] $s = -i\omega$

(a) At fully reflecting outlets, the pressure is imposed and therefore the pressure fluctuations are zero. $Z = 0$ and, for plane waves, $R = -1$. We obtain the Dirichlet boundary condition[4], $\hat{p} = 0$.

(b) At rigid walls or at fully reflecting inlets, the velocity is imposed and therefore the velocity fluctuations are zero. $Z \to \infty$ and $R = 1$. We obtain the Neumann boundary condition[5], $\boldsymbol{\nabla}\hat{p} \cdot \boldsymbol{n} = 0$.

(c) There can also be non-reflecting or anechoic boundaries, where $Z = 1$ and $R = 0$.

2.4 Acoustic energy balance

The modal analysis indicates whether or not a thermoacoustic system is linearly stable. The acoustic energy balance provides information about the stabilizing (or destabilizing) mechanism. In this section we derive the stability criterion, based on the acoustic energy, for a system governed by the inhomogeneous Helmholtz equation, Eq. (2.18). We consider the flame response model of Section 2.2, and acoustic impedance boundary conditions, and discuss the role of different terms on the stability of the system. In the energy norm, we will not consider the contribution given by the entropy fluctuations (Nicoud and Poinsot, 2005). If we take $\bar{\rho}\boldsymbol{u}' \cdot$ (2.1b) + $(1/\gamma\bar{p})$(2.1c), we obtain

$$\frac{\partial e'}{\partial t} + \boldsymbol{\nabla} \cdot (p'\boldsymbol{u}') = \frac{\gamma - 1}{\gamma \bar{p}} p' \dot{q}' \tag{2.31}$$

where $e' = \bar{\rho}\boldsymbol{u}'^2/2 + (1/\gamma\bar{p})p'^2/2$ is the acoustic energy density and $p'\boldsymbol{u}'$ is the acoustic energy flux (Poinsot and Veynante, 2012). If we average over the volume and over one period of oscillation, we obtain the stability criterion

$$\frac{\gamma - 1}{\gamma \bar{p}} \int_\Omega \int_0^T p' \dot{q}' \, \mathrm{d}t \, \mathrm{d}V < \int_{\partial\Omega} \int_0^T p' \boldsymbol{u}' \cdot \boldsymbol{n} \, \mathrm{d}t \, \mathrm{d}S \tag{2.32}$$

Assuming that p', $\boldsymbol{u}' \cdot \boldsymbol{n}$ and $\dot{q}'$ are harmonic in time, we can write them in the form

$$(\cdot)'(\boldsymbol{x}, t) = \left|\hat{(\cdot)}(\boldsymbol{x})\right| \cos\left(2\pi f t - \angle\hat{(\cdot)}(\boldsymbol{x})\right) e^{\lambda t} \tag{2.33}$$

which is equivalent to Eq. (2.16). f and λ are the frequency and the growth rate of the eigenvalue, $\omega = 2\pi f + i\lambda$, respectively, and $\angle\hat{(\cdot)}$ is the phase angle. Before substituting the

[4]Also called zero pressure, pressure node, sound soft boundary condition

[5]Also called zero normal velocity, velocity node, pressure antinode, sound hard boundary condition

expressions for p', $\boldsymbol{u}' \cdot \boldsymbol{n}$ and $\dot{q}'$ into (2.32), we write the trigonometric identity

$$\cos(2\pi f t - \angle\hat{p}) \cos(2\pi f t - \angle\hat{q}) = \frac{1}{2}\left[\cos(4\pi f t - \angle\hat{p} - \angle\hat{q}) + \cos(\angle\hat{q} - \angle\hat{p})\right] \tag{2.34}$$

Equation (2.32) becomes

$$\frac{\gamma - 1}{\gamma \bar{p}} \int_\Omega |\hat{p}||\hat{q}| \cos(\angle\hat{q} - \angle\hat{p}) \, \mathrm{d}V < \int_{\partial\Omega} |\hat{p}||\hat{\boldsymbol{u}} \cdot \boldsymbol{n}| \cos(\angle\hat{\boldsymbol{u}} \cdot \boldsymbol{n} - \angle\hat{p}) \, \mathrm{d}S \tag{2.35}$$

In fact, the integral containing $\cos(4\pi f t - \angle\hat{p} - \angle\hat{q})e^{2\lambda t}$ is zero, regardless of the values assumed by the two phase angles (and analogously the integral containing $\cos(4\pi f t - \angle\hat{p} - \angle\hat{\boldsymbol{u}} \cdot \boldsymbol{n})e^{2\lambda t}$). If the pressure and heat release rate oscillations are sufficiently in phase, then the acoustic energy grows, unless (or until) balanced by the loss due to acoustic radiation from the boundaries or damping, which is not modelled here. We substitute $\hat{q}$ from Eq. (2.20) and $\hat{\boldsymbol{u}} \cdot \boldsymbol{n}$ from Eq. (2.28) into Eq. (2.35), and obtain

$$(\gamma - 1)\frac{\dot{Q}_t}{U_b}|F(\omega)| \int_\Omega v(\boldsymbol{x})|\hat{p}||\hat{\boldsymbol{u}}(\boldsymbol{x}_r) \cdot \boldsymbol{n}_r| \cos(\angle\hat{q} - \angle\hat{p}) \, \mathrm{d}V < \int_{\partial\Omega} \frac{\bar{c}}{|Z|}\left|\hat{p}^2\right| \cos(\angle Z) \, \mathrm{d}S \tag{2.36}$$

where $\angle\hat{q} = \angle F(\omega) + \angle\hat{\boldsymbol{u}}(\boldsymbol{x}_r) \cdot \boldsymbol{n}_r$. The left-hand side depends on the phase angle difference between the heat release rate perturbation and the pressure perturbation, $\angle\hat{q} - \angle\hat{p}$. It also depends on the modulus of the flame transfer function, $F(\omega)$, of the pressure, $\hat{p}$, in the flame volume and of the component of the velocity along the reference direction at the reference point, $\hat{\boldsymbol{u}}(\boldsymbol{x}_r) \cdot \boldsymbol{n}_r$. The right-hand side depends on the modulus of the pressure at the boundary and on the impedance, Z. The sign of the left-hand side depends exclusively on the phase between $\hat{p}$ and $\hat{q}$. The right-hand side, which equals zero for Dirichlet and Neumann boundary conditions, represents the work done by the oscillating fluid on the surroundings.

2.5 Nondimensionalization

The first application in this thesis is the electrically heated Rijke tube modelled in Juniper (2018). This was also one of the test cases for the verification of the finite element solver. In Juniper (2018), the equations are written in nondimensional form. We explain here how the momentum equation, Eq. (2.17), the inhomogeneous Helmholtz equation, Eq. (2.23) and the Robin boundary conditions, Eq. (2.29) are nondimensionalized.

The reference length, L, is the characteristic acoustic wavelength of the thermoacoustic system, e.g. the acoustic wavelength in a Rijke tube. The reference time is L/c_a, where $c_a = \sqrt{\gamma p_a/\rho_a}$ is the speed of sound in the ambient fluid. ρ_a is the ambient density and p_a is the ambient pressure. We denote the nondimensional quantities by a tilde $\tilde{(\cdot)}$. The independent and dependent variables are nondimensionalized as follows

$$x = \tilde{x}L, \quad t = \tilde{t}\frac{L}{c_a}, \quad \rho = \tilde{\rho}\frac{\rho_a}{\gamma}, \quad \boldsymbol{u} = \tilde{\boldsymbol{u}}c_a, \quad p = \tilde{p}p_a \tag{2.37}$$

The reference density appears naturally when scaling the momentum equation, Eq. (2.17), with the velocity and pressure scales. The nondimensionalization is the same for the mean quantities and for the perturbation quantities ($\bar{c} = \tilde{\bar{c}}c_a$). When we nondimensionalize Eq. (2.23), the complex angular frequency is scaled as $\omega = \tilde{\omega}c_a/L$. The remaining dimensional quantities are scaled as $\dot{Q}_t = \tilde{\dot{Q}}_t p_a L^2 c_a$, $U_b = \tilde{U}_b c_a$ and $v = \tilde{v}/L^3$ ($w = \tilde{w}/L^3$). When using the $n-\tau$ model, the dimensional interaction index is scaled as $n = \tilde{n}p_a L^2$, and the time delay as $\tau = \tilde{\tau}L/c_a$. With this choice of the reference quantities, Eqs. (2.17), (2.23) and (2.29) remain the same, with the only difference that all the variables are now nondimensional.

Chapter 3

Adjoint equations, finite element method and eigensolvers

In this chapter we derive the continuous adjoint of the thermoacoustic Helmholtz equation. We apply the Bubnov-Galerkin finite element method to the weak formulation of the thermoacoustic Helmholtz equation. And finally we derive the discrete adjoint. When applying the Bubnov-Galerkin finite element method, there is no difference between the discretization of the continuous adjoint and the discrete adjoint. The continuous adjoint will be used to derive the shape derivatives. The discrete adjoint is used in the code and will be used to improve the convergence of the eigensolver. Similar derivations can be found in (Mensah, 2019) and, for the 1D case, in (Juniper, 2018). The final part of the chapter is about the nonlinear eigenvalue problem and the algorithms used to solve it.

3.1 Weak formulation and continuous adjoint

In this section we write the weak formulation of the thermoacoustic Helmholtz equation and derive the continuous adjoint. Details about the theory and the application of adjoint equations in stability analysis in fluid dynamics can be found in (Luchini and Bottaro, 2014) and in thermoacoustics in (Juniper and Sujith, 2018; Magri, 2019). We start with the direct equation in strong form. The direct equation is the Helmholtz equation with unsteady heat release, in the domain Ω, and the boundary conditions are Dirichlet, Neumann and Robin, applied on separate

subsets of the boundary, $\partial\Omega = \partial\Omega_D \cup \partial\Omega_N \cup \partial\Omega_R$.

$$\boldsymbol{\nabla}\cdot\left(\bar{c}^2\boldsymbol{\nabla}\hat{p}\right) + \omega^2\hat{p} = \frac{\dot{Q}_t}{U_b}(\gamma-1)v(\boldsymbol{x})F(\omega)\int_\Omega w(\boldsymbol{\xi})\frac{1}{\bar{\rho}}\boldsymbol{\nabla}\hat{p}\cdot\boldsymbol{n}_r\,\mathrm{d}V\,, \quad \text{in } \Omega \tag{3.1a}$$

$$\hat{p} = 0, \quad \text{on } \partial\Omega_D \tag{3.1b}$$

$$\frac{\partial\hat{p}}{\partial n} = 0, \quad \text{on } \partial\Omega_N \tag{3.1c}$$

$$\frac{\partial\hat{p}}{\partial n} - \frac{i\omega}{\bar{c}Z}\hat{p} = 0, \quad \text{on } \partial\Omega_R \tag{3.1d}$$

Equation (3.1a) is in strong form. We want to write it in weak form and find the adjoint equation. First we need, however, to define what is a weak formulation and what is an adjoint operator. We begin by defining the space of complex-valued square-integrable functions, $L^2(\Omega) = \left\{v : \Omega \to \mathbb{C} \mid \int_\Omega |v|^2\,\mathrm{d}V < \infty\right\}$. We specify the inner product

$$\langle u|v\rangle_{L^2(\Omega)} = \int_\Omega u^* v\,\mathrm{d}V\,, \quad u, v \in L^2(\Omega) \tag{3.2}$$

And the norm

$$\|v\|_{L^2(\Omega)} = \sqrt{\langle v|v\rangle_{L^2(\Omega)}}, \quad v \in L^2(\Omega) \tag{3.3}$$

$\langle\cdot|\cdot\rangle$ is a sesquilinear form. From now on we will drop the subscript $(\cdot)_{L^2(\Omega)}$. We write Eq. (3.1a) as

$$\mathcal{L}(\omega)\hat{p} = 0 \tag{3.4}$$

$\mathcal{L}$ is a linear differential operator. ω and $\hat{p}$ are the eigenvalues and the eigenfunctions of $\mathcal{L}$, respectively. The operator is nonlinear with respect to ω and linear with respect to $\hat{p}$. We multiply Eq. (3.4) by the complex conjugate of a *test* function, $\hat{p}^\dagger$, and integrate over the domain Ω to obtain the weak formulation (after integration by parts)

$$\left\langle\hat{p}^\dagger\middle|\mathcal{L}\hat{p}\right\rangle = 0 \tag{3.5}$$

$\hat{p}$ is labelled a *trial* function. A solution of Eq. (3.4), the strong formulation, is also a solution of Eq. (3.5), the weak formulation. The opposite is not necessarily true. The adjoint of the direct operator $\mathcal{L}$ is defined such that

$$\left\langle\hat{p}^\dagger\middle|\mathcal{L}\hat{p}\right\rangle = \left\langle\mathcal{L}^\dagger\hat{p}^\dagger\middle|\hat{p}\right\rangle + b.t. \tag{3.6}$$

$\mathcal{L}^\dagger$ is the adjoint operator. $\hat{p}$ is the *direct* eigenfunction and $\hat{p}^\dagger$ is the *adjoint* eigenfunction. The boundary terms on the right-hand side, $b.t.$ arise from integration by parts. We will use

the same symbols for the trial function and the adjoint eigenfunction and for the test function and the direct eigenfunction. We derive the weak formulation and the adjoint of Eq. (3.1a) separately for the left-hand side and the right-hand side.

3.1.1 Left-hand side

The left-hand side in strong form is

$$\boldsymbol{\nabla} \cdot \left(\bar{c}^2 \boldsymbol{\nabla} \hat{p}\right) + \omega^2 \hat{p} = 0 \tag{3.7}$$

We multiply by the complex conjugate of the test function $\hat{p}^\dagger$, and integrate over Ω.

$$\int_\Omega \hat{p}^{\dagger^*} \boldsymbol{\nabla} \cdot \left(\bar{c}^2 \boldsymbol{\nabla} \hat{p}\right) \mathrm{d}V + \omega^2 \int_\Omega \hat{p}^{\dagger^*} \hat{p} \, \mathrm{d}V = 0 \tag{3.8}$$

We integrate by parts the first term of Eq. (3.8)

$$-\int_\Omega \bar{c}^2 \boldsymbol{\nabla} \hat{p}^{\dagger^*} \cdot \boldsymbol{\nabla} \hat{p} \, \mathrm{d}V + \int_{\partial\Omega} \hat{p}^{\dagger^*} \bar{c}^2 \frac{\partial \hat{p}}{\partial n} \, \mathrm{d}S + \omega^2 \int_\Omega \hat{p}^{\dagger^*} \hat{p} \, \mathrm{d}V = 0 \tag{3.9}$$

The trial function $\hat{p}$ does not have to be twice-differentiable. We define the function spaces[1] $H^1(\Omega) = \{v : \Omega \to \mathbb{C} \mid \|\boldsymbol{\nabla} v\| < \infty, \|v\| < \infty\}$ and $H_0^1(\Omega) = \left\{v \in H^1(\Omega) \mid v|_{\partial\Omega_D} = 0\right\}$. Although it is not a strict requirement, the trial function $\hat{p}$ and the test function $\hat{p}^\dagger$ will belong to the same function space, H_0^1. Therefore, after applying the boundary conditions, the weak formulation of Eq. (3.7) is

$$-\int_\Omega \bar{c}^2 \boldsymbol{\nabla} \hat{p}^{\dagger^*} \cdot \boldsymbol{\nabla} \hat{p} \, \mathrm{d}V + \omega \int_{\partial\Omega_R} \frac{i\bar{c}}{Z} \hat{p}^{\dagger^*} \hat{p} \, \mathrm{d}S + \omega^2 \int_\Omega \hat{p}^{\dagger^*} \hat{p} \, \mathrm{d}V = 0 \tag{3.10}$$

In order to find the adjoint, we integrate by parts the first term of Eq. (3.9) a second time

$$\int_\Omega \boldsymbol{\nabla} \cdot \left(\bar{c}^2 \boldsymbol{\nabla} \hat{p}^{\dagger^*}\right) \hat{p} \, \mathrm{d}V + \int_{\partial\Omega} \hat{p}^{\dagger^*} \bar{c}^2 \frac{\partial \hat{p}}{\partial n} \, \mathrm{d}S - \int_{\partial\Omega} \frac{\partial \hat{p}^{\dagger^*}}{\partial n} \bar{c}^2 \hat{p} \, \mathrm{d}S + \omega^2 \int_\Omega \hat{p}^{\dagger^*} \hat{p} \, \mathrm{d}V = 0 \tag{3.11}$$

We can eliminate the boundary terms from Eq. (3.11), i.e. second and third integral, by choosing the following boundary conditions for the adjoint: $\hat{p}^\dagger = 0$ on $\partial\Omega_D$, $\partial\hat{p}^\dagger / \partial n = 0$ on $\partial\Omega_N$ and $\partial\hat{p}^\dagger / \partial n + i\omega^* / (\bar{c} Z^*) \hat{p}^\dagger = 0$ on $\partial\Omega_R$. The strong formulation of the adjoint equation is

$$\boldsymbol{\nabla} \cdot \left(\bar{c}^2 \boldsymbol{\nabla} \hat{p}^\dagger\right) + \omega^{*^2} \hat{p}^\dagger = 0 \tag{3.12}$$

[1] Hilbert spaces

In this case, the adjoint operator is self-adjoint if the impedance, Z, is purely imaginary. An operator is self-adjoint if the direct and the adjoint operator are the same.

3.1.2 Right-hand side

The right-hand side in strong form is

$$(\gamma - 1)\frac{\dot{Q}_t}{U_b} v(\boldsymbol{x}) F(\omega) \int_\Omega w(\boldsymbol{\xi}) \frac{1}{\bar{\rho}} \boldsymbol{\nabla} \hat{p} \cdot \boldsymbol{n}_r \, \mathrm{d}V(\boldsymbol{\xi}) \tag{3.13}$$

For now we will drop the constant factor $(\gamma - 1)\dot{Q}_t / U_b$, to keep the notation simple. We multiply Eq. (3.13) by the complex conjugate of the test function $\hat{p}^\dagger$, and integrate over Ω.

$$\int_\Omega \hat{p}^{\dagger^*} v(\boldsymbol{x}) F(\omega) \left(\int_\Omega w(\boldsymbol{\xi}) \frac{1}{\bar{\rho}} \boldsymbol{\nabla} \hat{p} \cdot \boldsymbol{n}_r \, \mathrm{d}V(\boldsymbol{\xi}) \right) \mathrm{d}V(\boldsymbol{x}) \tag{3.14}$$

Then we move the integral in the variable $\boldsymbol{\xi}$ outside the integral in the variable $\boldsymbol{x}$ and obtain the weak form

$$F(\omega) \int_\Omega v(\boldsymbol{x}) \hat{p}^{\dagger^*} \, \mathrm{d}V(\boldsymbol{x}) \int_\Omega w(\boldsymbol{\xi}) \frac{1}{\bar{\rho}} \boldsymbol{\nabla} \hat{p} \cdot \boldsymbol{n}_r \, \mathrm{d}V(\boldsymbol{\xi}) \tag{3.15}$$

In order to find the adjoint equation, we need to express the second integral in Eq. (3.15) as a functional of $\hat{p}$ instead of $\boldsymbol{\nabla}\hat{p}$. We integrate by parts remembering that, by construction, $w|_{\partial\Omega} = 0$.

$$\int_\Omega w(\boldsymbol{\xi}) \frac{1}{\bar{\rho}} \boldsymbol{\nabla} \hat{p} \cdot \boldsymbol{n}_r \, \mathrm{d}V = - \int_\Omega \boldsymbol{\nabla} \left(w(\boldsymbol{\xi}) \frac{1}{\bar{\rho}} \right) \cdot \boldsymbol{n}_r \hat{p} \, \mathrm{d}V + \underbrace{\int_{\partial\Omega} w(\boldsymbol{\xi}) \frac{1}{\bar{\rho}} \hat{p} \, \mathrm{d}V}_{=0} \tag{3.16}$$

We substitute Eq. (3.16) into Eq. (3.15) and obtain the weak form

$$- F(\omega) \int_\Omega v(\boldsymbol{x}) \hat{p}^{\dagger^*} \, \mathrm{d}V(\boldsymbol{x}) \int_\Omega \boldsymbol{\nabla} \left(w(\boldsymbol{\xi}) \frac{1}{\bar{\rho}} \right) \cdot \boldsymbol{n}_r \hat{p} \, \mathrm{d}V(\boldsymbol{\xi}) \tag{3.17}$$

This time we move the integral in $\boldsymbol{x}$ inside the integral in $\boldsymbol{\xi}$ and then swap the symbols $\boldsymbol{x}$ and $\boldsymbol{\xi}$

$$- \int_\Omega \boldsymbol{\nabla} \left(w(\boldsymbol{x}) \frac{1}{\bar{\rho}} \right) \cdot \boldsymbol{n}_r F(\omega) \left(\int_\Omega v(\boldsymbol{\xi}) \hat{p}^{\dagger^*} \, \mathrm{d}V(\boldsymbol{\xi}) \right) \hat{p} \, \mathrm{d}V(\boldsymbol{x}) \tag{3.18}$$

The strong formulation of the adjoint equation is

$$- \boldsymbol{\nabla} \left(w(\boldsymbol{x}) \frac{1}{\bar{\rho}} \right) \cdot \boldsymbol{n}_r F^*(\omega) \int_\Omega v(\boldsymbol{\xi}) \hat{p}^\dagger \, \mathrm{d}V(\boldsymbol{\xi}) \tag{3.19}$$

We need to write $1/\bar{\rho}(\boldsymbol{x}_r)\boldsymbol{\nabla}\hat{p}(\boldsymbol{x}_r)\cdot\boldsymbol{n}_r$ as an integral in order to derive the adjoint equation.

3.1.3 Full equation

Using the bra-ket notation, we can write the identity between the two sesquilinear forms

$$\left\langle \hat{p}^\dagger \middle| \boldsymbol{\nabla}\cdot\left(\bar{c}^2\boldsymbol{\nabla}\hat{p}\right) + \omega^2\hat{p} - (\gamma-1)\frac{\dot{Q}_t}{U_b}v(\boldsymbol{x})F(\omega)\int_\Omega w(\boldsymbol{\xi})\frac{1}{\bar{\rho}}\boldsymbol{\nabla}\hat{p}\cdot\boldsymbol{n}_r\,\mathrm{d}V(\boldsymbol{\xi})\right\rangle = \\ -\left\langle \boldsymbol{\nabla}\cdot\left(\bar{c}^2\boldsymbol{\nabla}\hat{p}^\dagger\right) + {\omega^*}^2\hat{p}^\dagger - (\gamma-1)\frac{\dot{Q}_t}{U_b}\boldsymbol{\nabla}\left(w(\boldsymbol{x})\frac{1}{\bar{\rho}}\right)\cdot\boldsymbol{n}_r F^*(\omega)\int_\Omega v(\boldsymbol{\xi})\hat{p}^\dagger\,\mathrm{d}V(\boldsymbol{\xi}) \middle| \hat{p}\right\rangle \quad (3.20)$$

In the direct problem, the source term is proportional to the gradient of the direct eigenfunction evaluated in the reference region, and acts in the heat release region. In the adjoint problem, the source term is proportional to the adjoint eigenfunction evaluated in the heat release region and acts in the reference region. The role of the two regions (or subdomains) is reversed. The spectrum of the adjoint operator is the complex conjugate of the spectrum of the direct operator.

3.2 Finite element method

In this section we apply the Bubnov-Galerkin finite element method to the weak formulation of the direct equation, Eq. (3.1a). A good introduction to the theory and the application of the finite element method can be found in Larson and Bengzon (2013). We discretize the left-hand side and the right-hand side separately.

3.2.1 Left-hand side

We write the left-hand side again in weak form, Eq. (3.9)

$$-\int_\Omega \bar{c}^2\boldsymbol{\nabla}\hat{p}^{\dagger *}\cdot\boldsymbol{\nabla}\hat{p}\,\mathrm{d}V + \int_{\partial\Omega}\hat{p}^{\dagger *}\bar{c}^2\frac{\partial\hat{p}}{\partial n}\,\mathrm{d}S + \omega^2\int_\Omega \hat{p}^{\dagger *}\hat{p}\,\mathrm{d}V = 0$$

We consider a triangulation[2] $\mathcal{K}$ of Ω. V_h is the space of piecewise continuous polynomials on $\mathcal{K}$ and $V_{h,0}\subset V_h$ is the subspace $V_{h,0} = \{v\in V_h : v|_{\partial\Omega_D} = 0\}$. We do not specify the order of the polynomials. ϕ_j is a basis of $V_{h,0}$, with $j = 1,\ldots,N$, where N is the number of degrees of freedom. We replace the trial function $\hat{p}$ and the test function $\hat{p}^\dagger$ with $\hat{p}_h$, $\hat{p}_h^\dagger\in V_{h,0}$. In the Bubnov-Galerkin finite element method, the trial and the test function belong to the same

[2] also called mesh

function space. We write $\hat{p}_h$ and $\hat{p}_h^\dagger$ as linear combinations of the bases of $V_{h,0}$.

$$\hat{p}_h(\boldsymbol{x}) = \sum_{j=1}^{N} \hat{p}_j \phi_j(\boldsymbol{x}) \tag{3.21a}$$

$$\hat{p}_h^\dagger(\boldsymbol{x}) = \sum_{j=1}^{N} \hat{p}_k^\dagger \phi_k(\boldsymbol{x}) \tag{3.21b}$$

We substitute Eqs. (3.21) into Eq. (3.9) and obtain

$$\hat{p}_k^{\dagger *} \left(- \int_\Omega \bar{c}^2 \boldsymbol{\nabla} \phi_k \cdot \boldsymbol{\nabla} \phi_j \, \mathrm{d}V + \int_{\partial\Omega} \phi_k \bar{c}^2 \frac{\partial \phi_j}{\partial n} \, \mathrm{d}S + \omega^2 \int_\Omega \phi_k \phi_j \, \mathrm{d}V \right) \hat{p}_j = 0 \tag{3.22}$$

We have used the Einstein summation convention. In Eq. (3.22), the second integral is zero on the Dirichlet boundary: $\phi_k = 0 \; \forall k : \boldsymbol{x}_k \in \partial\Omega_D$, and on the Neumann boundary: $\hat{p}_j \, \partial\phi_j / \partial n = 0 \; \forall j : \boldsymbol{x}_j \in \partial\Omega_N$. On the Robin boundary: $\hat{p}_j \, \partial\phi_j / \partial n = i\omega/(\bar{c}Z) \hat{p}_j \phi_j \; \forall j : \boldsymbol{x}_j \in \partial\Omega_R$. The discretization reads

$$\hat{p}_k^{\dagger *} \left(- \int_\Omega \bar{c}^2 \boldsymbol{\nabla} \phi_k \cdot \boldsymbol{\nabla} \phi_j \, \mathrm{d}V + \omega \int_{\partial\Omega_R} \frac{i\bar{c}}{Z} \phi_k \phi_j \, \mathrm{d}S + \omega^2 \int_\Omega \phi_k \phi_j \, \mathrm{d}V \right) \hat{p}_j = 0 \tag{3.23}$$

We define the matrices

$$A_{kj} = - \int_\Omega \bar{c}^2 \boldsymbol{\nabla} \phi_k \cdot \boldsymbol{\nabla} \phi_j \, \mathrm{d}V \tag{3.24a}$$

$$B_{kj} = \int_{\partial\Omega_R} \frac{i\bar{c}}{Z} \phi_k \phi_j \, \mathrm{d}S \tag{3.24b}$$

$$C_{kj} = \int_\Omega \phi_k \phi_j \, \mathrm{d}V \tag{3.24c}$$

A_{kj} and C_{kj} are real symmetric matrices (the Dirichlet boundary conditions are enforced symmetrically). If Z is not purely imaginary, B_{kj} is complex and non-Hermitian[3].

3.2.2 Right-hand side

For the right-hand side we follow exactly the same steps. We write the right-hand side again in weak form, Eq. (3.15).

$$F(\omega) \int_\Omega v(\boldsymbol{x}) \hat{p}^{\dagger *} \, \mathrm{d}V \int_\Omega w(\boldsymbol{x}) \frac{1}{\bar{\rho}} \boldsymbol{\nabla} \hat{p} \cdot \boldsymbol{n}_r \, \mathrm{d}V$$

[3] A Hermitian matrix (or self-adjoint matrix) is a complex square matrix that is equal to its own conjugate transpose.

We replace the trial function $\hat{p}$ and the test function $\hat{p}^\dagger$ with $\hat{p}_h$, $\hat{p}_h^\dagger \in V_{h,0}$, and write them as linear combinations of the bases of $V_{h,0}$.

$$\hat{p}_k^{\dagger *} F(\omega) \int_\Omega v(\boldsymbol{x}) \phi_k \, \mathrm{d}V \int_\Omega w(\boldsymbol{x}) \frac{1}{\bar{\rho}} \boldsymbol{\nabla} \phi_j \cdot \boldsymbol{n}_r \, \mathrm{d}V \, \hat{p}_j \tag{3.25}$$

The discretization then reads

$$D_{kj} = \frac{\dot{Q}_t}{U_b} (\gamma - 1) F(\omega) \underbrace{\int_\Omega v(\boldsymbol{x}) \phi_k \, \mathrm{d}V}_{a_k} \underbrace{\int_\Omega w(\boldsymbol{x}) \frac{1}{\bar{\rho}} \boldsymbol{\nabla} \phi_j \cdot \boldsymbol{n}_r \, \mathrm{d}V}_{b_j} \tag{3.26}$$

The matrix D_{kj} is given by the outer product between two vectors, a_k and b_j. D_{kj} is neither symmetric nor Hermitian. Both $v(\boldsymbol{x})$ and $w(\boldsymbol{x})$ must have compact support on Ω in order for D_{kj} to be sparse. If $w(\boldsymbol{x}) = \delta_D(\boldsymbol{x} - \boldsymbol{x}_r)$

$$\hat{p}_k^{\dagger *} F(\omega) \int_\Omega v(\boldsymbol{x}) \phi_k \, \mathrm{d}V \, \frac{1}{\bar{\rho}(\boldsymbol{x}_r)} \boldsymbol{\nabla} \phi_j(\boldsymbol{x}_r) \cdot \boldsymbol{n}_r \hat{p}_j \tag{3.27}$$

And

$$D_{kj} = \frac{\dot{Q}_t}{U_b} (\gamma - 1) F(\omega) \underbrace{\int_\Omega v(\boldsymbol{x}) \phi_k \, \mathrm{d}V}_{a_k} \underbrace{\frac{1}{\bar{\rho}(\boldsymbol{x}_r)} \boldsymbol{\nabla} \phi_j(\boldsymbol{x}_r) \cdot \boldsymbol{n}_r}_{b_j} \tag{3.28}$$

3.2.3 Full equation

The full discretization of Eq. (2.1) in compact form reads

$$\hat{p}_k^{\dagger *} \underbrace{\left(A_{kj} + \omega B_{kj} + \omega^2 C_{kj} - D_{kj}(\omega) \right)}_{L_{kj}(\omega)} \hat{p}_j = 0 \tag{3.29}$$

It is a nonlinear eigenvalue problem for ω. $L_{kj}(\omega)\hat{p}_j$ has to be equal to zero regardless of $\hat{p}_k^{\dagger *}$. $\hat{p}_j$ is the right eigenvector and $\hat{p}_k^{\dagger *}$ is the left eigenvector.

3.3 Discrete adjoint

We can either derive the adjoint equation and then discretize it or we can discretize and then derive the adjoint. In the first case, we find the continuous adjoint. In the second, we find the discrete adjoint. When using the Bubnov-Galerkin finite element method, there is no difference

between the discrete adjoint and the discretization of the continuous adjoint, i.e. the matrices are identical. In this section, we derive the discrete adjoint of Eq. (3.1).

Given two vectors $\mathbf{u}, \mathbf{v} \in \mathbb{C}^n$, we define the inner product $\langle \mathbf{v} | \mathbf{u} \rangle = \mathbf{v}^H \mathbf{u}$, where the superscript H denotes the conjugate transpose of a vector or a matrix. If $\mathbf{L} \in \mathbb{C}^{n \times n}$ is the discrete direct operator and $\mathbf{L}^\dagger \in \mathbb{C}^{n \times n}$ is the discrete adjoint operator

$$\left\langle \mathbf{p}^\dagger \middle| \mathbf{L}\mathbf{p} \right\rangle = \left\langle \mathbf{L}^\dagger \mathbf{p}^\dagger \middle| \mathbf{p} \right\rangle \tag{3.30}$$

where $\mathbf{p}$ is the direct eigenvector and $\mathbf{p}^\dagger$ is the adjoint eigenvector.

$$(\mathbf{p}^\dagger)^H \mathbf{L}(\omega)\mathbf{p} = ((\mathbf{L}(\omega))^H \mathbf{p}^\dagger)^H \mathbf{p} = ((\mathbf{L}^\dagger(\omega^*))\mathbf{p}^\dagger)^H \mathbf{p} \tag{3.31}$$

Therefore, the adjoint of a matrix is its conjugate transpose and the adjoint eigenvector, $\mathbf{p}^\dagger$, is the left eigenvector of $\mathbf{L}$. The spectrum of the discrete adjoint operator $\mathbf{L}^\dagger$ is the complex conjugate of the spectrum of $\mathbf{L}$. The direct eigenproblem in matrix notation reads

$$\mathbf{L}(\omega)\mathbf{p} = \left(\mathbf{A} + \omega \mathbf{B} + \omega^2 \mathbf{C} - \mathbf{D}(\omega)\right)\mathbf{p} = 0 \tag{3.32}$$

And the adjoint eigenproblem

$$\mathbf{L}^\dagger(\omega^*)\mathbf{p}^\dagger = \left(\mathbf{A} + \omega^* \mathbf{B}^{\mathrm{H}} + \omega^{*^2} \mathbf{C} - (\mathbf{D}(\omega))^H\right)\mathbf{p}^\dagger = 0 \tag{3.33}$$

The conjugate transpose of Eq. (3.29) is

$$\hat{p}_j^* \underbrace{\left(A_{jk} + \omega^* B_{jk}^* + \omega^{*^2} C_{jk} - D_{jk}^*(\omega)\right)}_{L_{jk}^*(\omega)} \hat{p}_k^\dagger = 0 \tag{3.34}$$

The discretization matrices of the adjoint eigenproblem are

$$A_{jk} = A_{kj} \tag{3.35a}$$

$$B_{jk}^* = -\int_{\partial\Omega_R} \frac{i\bar{c}}{Z^*} \phi_j \phi_k \, \mathrm{d}S \tag{3.35b}$$

$$C_{jk} = C_{kj} \tag{3.35c}$$

$$D_{jk}^* = \frac{\dot{Q}_t}{U_b}(\gamma - 1)F^*(\omega) \underbrace{\frac{1}{\bar{\rho}(\boldsymbol{x}_r)} \nabla \phi_j(\boldsymbol{x}_r) \cdot \boldsymbol{n}_r}_{b_j} \underbrace{\int_\Omega v(\boldsymbol{x}) \phi_k \, \mathrm{d}V}_{a_k} \tag{3.36}$$

3.4 Eigensolver

In this section, we give the basic definitions of nonlinear eigenvalue problems for finite-dimensional linear operators. Useful references are (Güttel and Tisseur, 2017; Mehrmann and Voss, 2004).

Given a matrix-valued function $\mathbf{L}\colon \mathbb{C} \to \mathbb{C}^{n\times n}$, the nonlinear eigenvalue problem consists in finding the eigenvalues $\omega \in \mathbb{C}$ and the non-zero eigenvectors $\mathbf{p} \in \mathbb{C}^n$ such that

$$\mathbf{L}(\omega)\mathbf{p} = 0 \tag{3.37}$$

In other words, if we consider a family of linear operators $\mathbf{L}(z)$, which is a family of mappings from a scalar to a matrix, the eigenvalues are the scalars, ω, such that the matrix $\mathbf{L}(z)$ is non-invertible. The eigenvectors associated with the eigenvalue ω are the non-zero vectors in the nullspace of $\mathbf{L}(\omega)$, also called eigenspace and denoted by $\text{null}(\mathbf{L}(\omega))$. $\mathbf{L}$ depends nonlinearly on z and is linear with respect to $\mathbf{p}$. $(\omega, \mathbf{p})$ is an eigenpair of $\mathbf{L}$ and the set of all eigenvalues is the specturm of $\mathbf{L}$.

The eigenvalues, ω, of $\mathbf{L}$ are the solutions of the scalar equation $f(z) = \det(\mathbf{L}(z)) = 0$. The algebraic multiplicity of an eigenvalue, ω, is defined as the multiplicity of the root of $\det(\mathbf{L}(z))\big|_{z=\omega}$, i.e., the smallest integer $j \geq 1$ such that $\partial^j / \partial z^j \ \det(\mathbf{L}(z))\big|_{z=\omega} \neq 0$. Unlike in linear eigenvalue problems, in nonlinear eigenvalue problems the algebraic multiplicity can be greater than the dimension of the problem, n. The geometric multiplicity of an eigenvalue, ω, is defined as the dimension of the nullspace of $\mathbf{L}(\omega)$, denoted by $\dim(\text{null}(\mathbf{L}(\omega)))$. The eigenvectors belonging to distinct eigenvalues are not necessarily linearly independent. An eigenvalue, ω, is called semi-simple if its algebraic multiplicity is equal to its geometric multiplicity. It is called simple if its algebraic multiplicity is one and degenerate if its algebraic multiplicity is greater than one. Problems with symmetries such as rotationally symmetric annular combustors have degenerate eigenvalues. An eigenvalue is called defective if its algebraic multiplicity is greater than its geometric multiplicity.

3.4.1 Fixed-point iteration

At each iteration we solve a generalized eigenvalue problem for f^2.

$$\mathbf{L}(f;\omega)\mathbf{p} = \left(\mathbf{A} + \omega^{[k]}\mathbf{B} + f^2(\omega^{[k]})\mathbf{C} - \mathbf{D}(\omega^{[k]})\right)\mathbf{p} = 0 \tag{3.38}$$

f is the eigenvalue and $\omega^{[k]}$ is a parameter. At the zeroth iteration, $\omega^{[k]} = 0$. Therefore, there is no unsteady heat release, and we apply Neumann boundary conditions instead of Robin boundary conditions on $\partial\Omega_R$. In the simplest version of the fixed-point iteration, $\omega^{[k+1]} = f(\omega^{[k]})$, and

the iteration might not converge to a fixed point. According to Banach's fixed-point theorem, a necessary condition for the mapping, f, to converge to a fixed point, ω, is that $|f'(\omega)| < 1$. ω is then an attracting fixed point. In this case, there is no guarantee that $|f'(\omega)| < 1$. In order to improve the convergence, we can use a relaxation method.

$$\omega^{[k+1]} = g(\omega^{[k]}; \alpha) \equiv \alpha f(\omega^{[k]}) + (1 - \alpha)\omega^{[k]} \tag{3.39}$$

g is a mapping and α is a relaxation factor. A sequence $\omega^{[k]}$ converges to a fixed point ω at a rate of convergence m if there exists $G > 0$ such that

$$|\omega^{[k+1]} - \omega| \leq G|\omega^{[k]} - \omega|^m \tag{3.40}$$

Furthermore, the rate of convergence is equal to the smallest positive integer, m, satisfying $\partial^m/\partial z^m \; g(z = \omega) \neq 0$. If $g'(\omega) = 0$, the rate of convergence is superlinear.

$$g'(\omega^{[k]}; \alpha) = \alpha f'(\omega^{[k]}) + 1 - \alpha = 0 \tag{3.41}$$

From Eq. (3.41) we obtain that

$$\alpha = \frac{1}{1 - f'(\omega^{[k]})} \tag{3.42}$$

We can approximate $f'(\omega^{[k]})$ with a backward difference[4], or we can use perturbation theory (see Appendix A). The exact derivative of f with respect to ω is

$$f'(\omega) = -\frac{\mathbf{p}^{\dagger H} \; \partial \mathbf{L}(f;\omega)/\partial\omega \; \mathbf{p}}{\mathbf{p}^{\dagger H} \; \partial \mathbf{L}(f;\omega)/\partial f \; \mathbf{p}} \tag{3.43}$$

Combining Eq. (3.43) with Eq. (3.38), we obtain

$$f'(\omega) = -\frac{\mathbf{p}^{\dagger H}\big(\mathbf{B} - \mathbf{D}'(\omega)\big)\mathbf{p}}{\mathbf{p}^{\dagger H} 2f\mathbf{C}\mathbf{p}} \tag{3.44}$$

See Algorithm 1. The fixed-point iteration can be implemented in more than one way. Instead of a linear eigenvalue problem, we can choose to solve at each iteration a quadratic eigenvalue problem for f.

$$\mathbf{L}(f;\omega)\mathbf{p} = \big(\mathbf{A} + f(\omega^{[k]})\mathbf{B} + f^2(\omega^{[k]})\mathbf{C} - \mathbf{D}(\omega^{[k]})\big)\mathbf{p} = 0 \tag{3.45}$$

[4] $\frac{f(\omega^{[k]}) - f(\omega^{[k-1]})}{\omega^{[k]} - \omega^{[k-1]}}$

The derivative of f with respect to ω will be

$$f'(\omega) = \frac{\mathbf{p}^{\dagger H}\mathbf{D}'(\omega)\mathbf{p}}{\mathbf{p}^{\dagger H}\left(\mathbf{B} + 2f\mathbf{C}\right)\mathbf{p}} \tag{3.46}$$

If we use Eq. (3.44) or (3.46), at each iteration we need the left eigenvector. We can either solve the adjoint eigenproblem or, if available, we can extract the left eigenvector from the eigensolver. SLEPc EPS class for linear eigenvalue problems includes this option, although it is not accurate when the eigenvalue is degenerate. For a two-fold degenerate eigenvalue, one of the two left eigenvectors is not computed with sufficient accuracy. SLEPc PEP class for polynomial eigenvalue problems does not include this option.

Algorithm 1: Fixed-point iteration

function `Eigensolver(`**A**, **B**, **C**, **D**, *tol*, *maxiter*`):`
- $k \leftarrow -1$
- $\omega^{[k]} \leftarrow 0$
- Solve $\mathbf{L}(f;\omega^{[k]})\mathbf{p} = 0$ to find f^2 and $\mathbf{p}$
- $\omega^{[k+1]} = f$
- $\Delta\omega \leftarrow 2 \times tol$
- **while** $|\Delta\omega| > tol$ **and** $k < maxiter$ **do**
  - $k \leftarrow k + 1$
  - Solve $\mathbf{L}(f;\omega^{[k]})\mathbf{p} = 0$ to find f^2 and $\mathbf{p}$
  - Solve $(\mathbf{L}(f;\omega^{[k]}))^H\mathbf{p}^\dagger = 0$ to find f^{*2} and $\mathbf{p}^\dagger$
  - $f' \leftarrow -\dfrac{\mathbf{p}^{\dagger H}\,\partial/\partial\omega\,\mathbf{L}(f;\omega^{[k]})\mathbf{p}}{\mathbf{p}^{\dagger H}\,\partial/\partial f\,\mathbf{L}(f;\omega^{[k]})\mathbf{p}}$
  - $\alpha \leftarrow \dfrac{1}{1-f'}$
  - $\omega^{[k+1]} \leftarrow \alpha f + (1-\alpha)\omega^{[k]}$
  - $\Delta\omega \leftarrow \omega^{[k+1]} - \omega^{[k]}$
- **end**
- **return** $\omega^{[k+1]}$, $\mathbf{p}$, $\mathbf{p}^\dagger$

end

3.4.2 Newton's method

Perturbation theory enables us to calculate the exact derivative of the eigenvalues of a linear operator with respect to any parameter, provided that the dependence of the operator on the parameter is analytic. This is explained in Appendix A. In his thesis, Mensah (2019) developed a

Newton's method for nonlinear eigenvalue problems exploiting the knowledge of the eigenvalue derivative. The rate of convergence of this method is quadratic.

At each iteration we solve an auxiliary generalized eigenvalue problem for λ.

$$\mathbf{L}(\omega)\mathbf{p} = \lambda\mathbf{C}\mathbf{p} \tag{3.47}$$

We want to find ω such that $\lambda = 0$. As with the fixed-point iteration, here ω takes the role of a parameter. If we linearize $\lambda = 0$ with respect to ω, we obtain

$$\lambda(\omega + \Delta\omega) \simeq \lambda(\omega) + \lambda'(\omega)\Delta\omega = 0 \tag{3.48}$$

Therefore, at each iteration step we update ω as

$$\omega^{[k+1]} = g(\omega^{[k]}) \equiv \omega^{[k]} - \frac{\lambda(\omega^{[k]})}{\lambda'(\omega^{[k]})} \tag{3.49}$$

g is a mapping. g' is guaranteed to be 0 at a fixed point. Using perturbation theory, the first derivative of λ with respect to ω is

$$\lambda'(\omega) = \frac{\mathbf{p}^{\dagger H}\mathbf{L}'(\omega)\mathbf{p}}{\mathbf{p}^{\dagger H}\mathbf{C}\mathbf{p}} \tag{3.50}$$

The matrices are defined as follows

$$\mathbf{L}(\omega) = \mathbf{A} + \omega\mathbf{B} + \omega^2\mathbf{C} - \mathbf{D}(\omega) \tag{3.51}$$

$$(\mathbf{L}(\omega))^H = \mathbf{A} + \omega^*\mathbf{B}^H + \omega^{*2}\mathbf{C} - (\mathbf{D}(\omega))^H \tag{3.52}$$

$$\mathbf{L}'(\omega) = \mathbf{B} + 2\omega\mathbf{C} - \mathbf{D}'(\omega) \tag{3.53}$$

See Algorithm 2. For a degenerate eigenvalue with multiplicity m, λ can be expressed as

$$\lambda(\omega) = (\omega - a)^m h(\omega) \tag{3.54}$$

where a is the fixed point and h is a function. In this case, the derivative of the mapping at the fixed point takes the value

$$g'(a) = \frac{m-1}{m} \tag{3.55}$$

which obviously is not zero, and the convergence of the method is not quadratic. This can be fixed using the mapping

$$\omega^{[k+1]} = g(\omega^{[k]}) \equiv \omega^{[k]} - m\frac{\lambda(\omega^{[k]})}{\lambda'(\omega^{[k]})} \tag{3.56}$$

which gives

$$g'(a) = 0 \tag{3.57}$$

Newton's method is only the first of a class of methods called Householder's methods. The second order method, called Halley's method, has cubic convergence. It requires the knowledge of the second-order derivative of λ and the eigenvector corrections. We will not consider these as we will not go beyond first-order perturbations.

Algorithm 2: Newton's method

function `Eigensolver(`**A**, **B**, **C**, **D**, $\omega^{[0]}$, *tol*, *maxiter*`):`
- $k \leftarrow -1$
- $\Delta\omega \leftarrow 2 \times tol$
- **while** $|\Delta\omega| > tol$ **and** $k < maxiter$ **do**
  - $k \leftarrow k + 1$
  - Solve $\mathbf{L}(\omega^{[k]})\mathbf{p} = \lambda\mathbf{C}\mathbf{p}$ to find λ and $\mathbf{p}$
  - Solve $(\mathbf{L}(\omega^{[k]}))^H\mathbf{p}^\dagger = \lambda^*\mathbf{C}\mathbf{p}^\dagger$ to find λ^* and $\mathbf{p}^\dagger$
  - $\lambda' \leftarrow \dfrac{\mathbf{p}^{\dagger H}\mathbf{L}'(\omega^{[k]})\mathbf{p}}{\mathbf{p}^{\dagger H}\mathbf{C}\mathbf{p}}$
  - $\omega^{[k+1]} \leftarrow \omega^{[k]} - \dfrac{\lambda}{\lambda'}$
  - $\Delta\omega \leftarrow \omega^{[k+1]} - \omega^{[k]}$
- **end**
- **return** $\omega^{[k+1]}$, $\mathbf{p}$, $\mathbf{p}^\dagger$

end

3.5 Code description

The code is written using the open-source computing platform FEniCS (Alnæs et al., 2015; Logg et al., 2012). At each iteration of either Algorithm 1 or Algorithm 2, the eigenvalue problem is solved using the SLEPc library (Hernandez et al., 2005). Generalized eigenvalue problems are solved with the Krylov-Schur method, which is a variation of the Arnoldi method (Arnoldi, 1951) with a very effective restarting technique. Polynomial eigenvalue problems

are solved building an Arnoldi factorization of the linearization without explicitly creating the matrices. In both cases, a shift-and-invert transformation is used to enhance the convergence of the eigenvalues in the neighbourhood of a given value. The mesh is generated using Gmsh (Geuzaine and Remacle, 2009) by way of a Delaunay triangulation.

Chapter 4

Shape derivatives

We wish to calculate how small modifications to the geometry of a combustor affect the stability of the thermoacoustic modes. This translates into the problem of finding the derivative of an eigenvalue with respect to arbitrary perturbations to the shape of the domain.

4.1 Shape derivative and Hadamard theorem

Following Schmidt (2010); Schmidt and Schulz (2010), we define a one-parameter family of bijective (invertible) linear mappings

$$T_t \colon \Omega \subset \mathbb{R}^d \times \mathbb{R}^+ \to \mathbb{R}^d, \quad \boldsymbol{x}, t \mapsto T_t(\boldsymbol{x}) \tag{4.1}$$

where t is the non-negative parameter of the transformation. T_t transforms the domain Ω into the deformed domain Ω_t.

$$\Omega_t = T_t(\Omega) = \{T_t(\boldsymbol{x}_0) \mid \boldsymbol{x}_0 \in \Omega\} \tag{4.2}$$

We use the linear transformation called perturbation of identity

$$T_t(\boldsymbol{x}) = \boldsymbol{x} + t\boldsymbol{V}(\boldsymbol{x}) \tag{4.3}$$

where $\boldsymbol{V}$ is a continuous vector field representing the direction of the perturbation. Let $\mathcal{J}$ be a shape functional. The shape derivative of $\mathcal{J}$ at Ω in the direction of the perturbation $\boldsymbol{V}$ is defined as the functional derivative

$$\mathrm{d}\mathcal{J}(\Omega)[\boldsymbol{V}] = \lim_{t \to 0^+} \frac{\mathcal{J}(\Omega_t) - \mathcal{J}(\Omega)}{t} \tag{4.4}$$

A shape functional $\mathcal{J}$ is said to be shape differentiable at Ω if the derivative, Eq. (4.4), exists for all the directions $\boldsymbol{V}$ and if the mapping $\boldsymbol{V} \mapsto \mathrm{d}\mathcal{J}(\Omega)[\boldsymbol{V}]$ is linear and continuous. Under mild smoothness assumptions, the shape derivative $\mathrm{d}\mathcal{J}$ depends only on the normal component of the vector field $\boldsymbol{V}$ at the boundary of the domain.

$$\mathrm{d}\mathcal{J}(\Omega)[\boldsymbol{V}] = \mathrm{d}\mathcal{J}(\Gamma)[C\boldsymbol{n}] = \int_\Gamma C\, G \,\mathrm{d}S \tag{4.5}$$

where Γ is the domain boundary, $C = \boldsymbol{V} \cdot \boldsymbol{n}$, and G is the shape gradient. This result is known as Hadamard theorem (or formula) (Delfour and Zolésio, 2011; Sokolowski and Zolesio, 1992). In Eq. (4.5), the shape derivative is said to be written in Hadamard form. $\boldsymbol{V} \cdot \boldsymbol{n} = G$ is the direction of greatest increase of $\mathcal{J}$.

4.2 Tangential calculus

In this short section we give some definitions from differential geometry that will be used throughout the derivations. Let f be a scalar field and $\boldsymbol{v}$ a vector field. The tangential gradient of f is

$$\boldsymbol{\nabla}_\Gamma f = \boldsymbol{\nabla} f - \frac{\partial f}{\partial n}\boldsymbol{n} = \frac{\partial f}{\partial x_i} - \frac{\partial f}{\partial x_j} n_j n_i \tag{4.6}$$

The tangential gradient is the orthogonal projection of the gradient onto the tangent space. The tangential divergence of $\boldsymbol{v}$ is

$$\mathrm{div}_\Gamma \boldsymbol{v} = \mathrm{div}\boldsymbol{v} - (D\boldsymbol{v}\boldsymbol{n}) \cdot \boldsymbol{n} = \boldsymbol{\nabla} \cdot \boldsymbol{v} - ((\boldsymbol{n} \cdot \boldsymbol{\nabla})\boldsymbol{v}) \cdot \boldsymbol{n} = \frac{\partial v_i}{\partial x_i} - n_j \frac{\partial v_i}{\partial x_j} n_i \tag{4.7}$$

$D\boldsymbol{v}$ is the Jacobian of $\boldsymbol{v}$ and $D\boldsymbol{v}\boldsymbol{n}$ is the matrix product between $D\boldsymbol{v}$ and $\boldsymbol{n}$. In addition to the definitions of tangential gradient and divergence, we give the Tangential Stokes formula (Delfour and Zolésio, 2011)

$$\int_\Gamma f \mathrm{div}_\Gamma \boldsymbol{v} + \nabla_\Gamma f \cdot \boldsymbol{v} \,\mathrm{d}S = \int_\Gamma \kappa f \boldsymbol{v} \cdot \boldsymbol{n} \,\mathrm{d}S \tag{4.8}$$

where $\kappa = \mathrm{div}_\Gamma \boldsymbol{n}$ is the curvature.

4.3 Shape derivatives under a state constraint

We want to derive a formula for the shape derivative in Hadamard form, or equivalently for the shape gradient, of ω, where ω is an eigenvalue of the thermoacoustic Helmholtz equation, (2.23).

We consider Robin boundary conditions, which contain Dirichlet and Neumann boundary conditions as special cases. The boundary Γ is split into a non-deformable and a deformable part. The first is denoted by Γ_0 and the second by Γ_1. The problem reads

$$\mathcal{L}(\omega)\hat{p} = 0 \quad \text{in } \Omega \tag{4.9a}$$

$$\frac{\partial \hat{p}}{\partial n} - \frac{i\omega}{\bar{c}Z}\hat{p} = 0 \quad \text{on } \Gamma = \Gamma_0 \cup \Gamma_1 \tag{4.9b}$$

where $\mathcal{L}$ is the linear operator, acting linearly on the eigenfunction $\hat{p}$, of the thermoacoustic Helmholtz equation (2.23). We apply the perturbation T_t. Instead of solving the problem on the perturbed domain Ω_t, we map the perturbed problem onto the unperturbed domain Ω.

Let $\hat{p}_t$ solve (4.9) in the perturbed domain $\Omega_t = T_t(\Omega)$ and let $\boldsymbol{x}_t = T_t(\boldsymbol{x})$ be a point on the perturbed boundary. The material shape derivative is

$$\mathrm{d}\hat{p}[\boldsymbol{V}](\boldsymbol{x}) = \left.\frac{\mathrm{d}}{\mathrm{d}t}\right|_{t=0} \hat{p}_t(\boldsymbol{x}_t) \tag{4.10}$$

The local shape derivative is

$$\hat{p}'[\boldsymbol{V}](\boldsymbol{x}) = \left.\frac{\mathrm{d}}{\mathrm{d}t}\right|_{t=0} \hat{p}_t(\boldsymbol{x}) \tag{4.11}$$

The relation between the first, which is a total derivative, and the second, which is a partial derivative, is given by the chain rule

$$\mathrm{d}\hat{p}[\boldsymbol{V}] = \hat{p}'[\boldsymbol{V}] + \boldsymbol{V} \cdot \boldsymbol{\nabla}\hat{p} \tag{4.12}$$

The material derivative of any boundary condition is identically zero. In the case of a non-deformable boundary, $\boldsymbol{V} = 0$, and the material derivative is the local derivative. In the case of a deformable boundary, $\boldsymbol{V} \neq 0$.

4.3.1 Shape derivative of the Robin boundary condition

We use the chain rule, Eq. (4.12), to express the material shape derivative of the Robin boundary condition on the deformable boundary, Γ_1, Eq. (4.9b), in terms of the local shape derivative of the eigenfunction, $\hat{p}$. The mean speed of sound, $\bar{c}$, depends on $\boldsymbol{x}$ and the specific acoustic impedance, Z, is assumed to be constant on Γ_1.

$$\boldsymbol{\nabla}\hat{p}' \cdot \boldsymbol{n} + \boldsymbol{\nabla}\hat{p} \cdot \boldsymbol{n}' + \boldsymbol{V} \cdot \boldsymbol{\nabla}(\boldsymbol{\nabla}\hat{p} \cdot \boldsymbol{n}) - \frac{i\omega'}{\bar{c}Z}\hat{p} - \frac{i\omega}{\bar{c}Z}\hat{p}' + \frac{i\omega}{\bar{c}^2 Z}\boldsymbol{V} \cdot \boldsymbol{\nabla}\bar{c}\hat{p} - \frac{i\omega}{\bar{c}Z}\boldsymbol{V} \cdot \boldsymbol{\nabla}\hat{p} = 0 \tag{4.13}$$

Equation (4.13) contains the local shape derivative and the gradient of the unit normal vector, $\boldsymbol{n}$. The unit normal vector is not defined in the interior of the domain, but only on the boundary. In order for $\boldsymbol{n}'$ and $\boldsymbol{\nabla n}$ to exist, we extend $\boldsymbol{n}$ into a tubular neighbourhood of Γ and denote this extension by $\mathcal{N}$. We choose as $\mathcal{N}$ the normalized gradient of the signed distance function, b, i.e. $\mathcal{N} = \boldsymbol{\nabla} b / \|\boldsymbol{\nabla} b\|$ (Schmidt and Schulz, 2010). By definition of signed distance function, $\mathcal{N} = \boldsymbol{n}$ on the boundary. If $\boldsymbol{V} = C\boldsymbol{n}$, the local shape derivative of the unit normal vector then is

$$n_i' = \mathcal{N}_i' = \mathrm{d}\mathcal{N}_i - V_j \frac{\partial \mathcal{N}_i}{\partial x_j} = \mathrm{d}\mathcal{N}_i - C\mathcal{N}_j \frac{\partial \mathcal{N}_i}{\partial x_j} = \mathrm{d}\mathcal{N}_i = \mathrm{d}n_i \tag{4.14}$$

In fact, if we assume that b is twice continuously differentiable, then $\mathcal{N}_j \, \partial \mathcal{N}_i / \partial x_j = 0$, as shown by Eq. (4.15).

$$0 = \frac{1}{2}\frac{\partial}{\partial x_i}(1) = \frac{1}{2}\frac{\partial}{\partial x_i}\left(\mathcal{N}_j \mathcal{N}_j\right) = \mathcal{N}_j \frac{\partial \mathcal{N}_j}{\partial x_i} = \frac{1}{\|b\|^2}\frac{\partial b}{\partial x_j}\frac{\partial}{\partial x_i}\frac{\partial b}{\partial x_j} = \frac{1}{\|b\|^2}\frac{\partial b}{\partial x_j}\frac{\partial}{\partial x_j}\frac{\partial b}{\partial x_i} = \mathcal{N}_j \frac{\partial \mathcal{N}_i}{\partial x_j} \tag{4.15}$$

$\mathrm{d}\mathcal{N}_i = \mathrm{d}n_i$ because the material shape derivative is defined for a point, $\boldsymbol{x}_t$, on the perturbed boundary. If, as is the case, $\boldsymbol{V}$ is orthogonal to Γ, then (Sonntag et al., 2016)

$$\mathrm{d}\boldsymbol{n} = -\boldsymbol{\nabla}_\Gamma (\boldsymbol{V} \cdot \boldsymbol{n}) = -\boldsymbol{\nabla}_\Gamma C \tag{4.16}$$

and the second term of Eq. (4.13) can be written as

$$\boldsymbol{\nabla} \hat{p} \cdot \boldsymbol{n}' = -\boldsymbol{\nabla} \hat{p} \cdot \boldsymbol{\nabla}_\Gamma C \tag{4.17}$$

Using index notation

$$\boldsymbol{V} \cdot \boldsymbol{\nabla}(\boldsymbol{\nabla} \hat{p} \cdot \boldsymbol{n}) = C\boldsymbol{\mathcal{N}} \cdot \boldsymbol{\nabla}(\boldsymbol{\nabla} \hat{p} \cdot \boldsymbol{\mathcal{N}}) = C\mathcal{N}_i \frac{\partial}{\partial x_i}\left(\frac{\partial \hat{p}}{\partial x_j}\mathcal{N}_j\right) = C\mathcal{N}_i \frac{\partial^2 \hat{p}}{\partial x_i \partial x_j}\mathcal{N}_j + \underbrace{C\mathcal{N}_j \frac{\partial \hat{p}}{\partial x_i}\frac{\partial \mathcal{N}_i}{\partial x_j}}_{=0, \text{ Eq. (4.15)}} \tag{4.18}$$

and the third term of Eq. (4.13) reduces to

$$\boldsymbol{V} \cdot \boldsymbol{\nabla}(\boldsymbol{\nabla} \hat{p} \cdot \boldsymbol{n}) = C\frac{\partial^2 \hat{p}}{\partial n^2} \tag{4.19}$$

Combining Eq. (4.13) with Eqs. (4.17) and (4.19), and observing that $\boldsymbol{V} \cdot \boldsymbol{\nabla}(\cdot) = C\, \partial(\cdot)/\partial n$, the material shape derivative of the Robin boundary condition is

$$\frac{\partial \hat{p}'}{\partial n} - \frac{i\omega}{\bar{c}Z}\hat{p}' = \boldsymbol{\nabla}\hat{p} \cdot \boldsymbol{\nabla}_\Gamma C - C\frac{\partial^2 \hat{p}}{\partial n^2} + \frac{i\omega'}{\bar{c}Z}\hat{p} - C\frac{i\omega}{\bar{c}^2 Z}\frac{\partial \bar{c}}{\partial n}\hat{p} + C\frac{i\omega}{\bar{c}Z}\frac{\partial \hat{p}}{\partial n} \tag{4.20}$$

The material shape derivatives of the Dirichlet and Neumann boundary conditions are special cases of Eq. (4.20). For Dirichlet boundary conditions, $Z = 0$ and $\hat{p} = 0$, therefore

$$\hat{p}' = -C\frac{\partial \hat{p}}{\partial n} \tag{4.21}$$

For Neumann boundary conditions, $Z \to \infty$ and $\partial\hat{p}/\partial n = 0$, therefore

$$\frac{\partial \hat{p}'}{\partial n} = \boldsymbol{\nabla}_\Gamma \hat{p} \cdot \boldsymbol{\nabla}_\Gamma C - C\frac{\partial^2 \hat{p}}{\partial n^2} \tag{4.22}$$

4.3.2 Eigenvalue shape derivative

In this section we derive the formula for the shape derivative of the eigenvalues of Eq. (4.9) in Hadamard form. We first consider the case of Robin boundary conditions and then those of Dirichlet and Neumann boundary conditions. We start by taking the material shape derivative of Eq. (4.9). The material shape derivative is equal to the local shape derivative in the domain, Ω, and on the non-deformable boundary, Γ_0.

$$\mathcal{L}'(\omega)\omega'\hat{p} + \mathcal{L}(\omega)\hat{p}' = 0 \quad \text{in } \Omega \tag{4.23a}$$

$$\frac{\partial \hat{p}'}{\partial n} - \frac{i\omega}{\bar{c}Z}\hat{p}' = \frac{i\omega'}{\bar{c}Z}\hat{p} \quad \text{on } \Gamma_0 \tag{4.23b}$$

$$\frac{\partial \hat{p}'}{\partial n} - \frac{i\omega}{\bar{c}Z}\hat{p}' = \boldsymbol{\nabla}\hat{p} \cdot \boldsymbol{\nabla}_\Gamma C - C\frac{\partial^2 \hat{p}}{\partial n^2} + \frac{i\omega'}{\bar{c}Z}\hat{p} - C\frac{i\omega}{\bar{c}^2 Z}\frac{\partial \bar{c}}{\partial n}\hat{p} + C\frac{i\omega}{\bar{c}Z}\frac{\partial \hat{p}}{\partial n} \quad \text{on } \Gamma_1 \tag{4.23c}$$

We multiply (4.23a) by the complex conjugate of the adjoint eigenfunction, $\hat{p}^{\dagger^*}$, and integrate over the domain, Ω. Applying the definition of the adjoint operator, Eq. (3.6)

$$\left\langle \hat{p}^\dagger \middle| \mathcal{L}'(\omega)\hat{p} \right\rangle \omega' + \left\langle \mathcal{L}^\dagger(\omega^*)\hat{p}^\dagger \middle| \hat{p}' \right\rangle + \int_\Gamma \hat{p}^{\dagger^*} \bar{c}^2 \frac{\partial \hat{p}'}{\partial n}\, \mathrm{d}S - \int_\Gamma \frac{\partial \hat{p}^{\dagger^*}}{\partial n} \bar{c}^2 \hat{p}'\, \mathrm{d}S = 0 \tag{4.24}$$

The boundary integral terms arise from integrating twice by parts the operator $\boldsymbol{\nabla} \cdot \bar{c}^2 \boldsymbol{\nabla}(\cdot)$. We substitute Eqs. (4.23b) and (4.23c) into Eq. (4.24). We can eliminate the terms containing the

eigenfunction sensitivity, $\hat{p}'$, by defining the adjoint problem

$$\mathcal{L}^\dagger(\omega^*)\hat{p}^\dagger = 0 \quad \text{in } \Omega \tag{4.25a}$$

$$\frac{\partial \hat{p}^\dagger}{\partial n} + \frac{i\omega^*}{\bar{c}Z^*}\hat{p}^\dagger = 0 \quad \text{on } \Gamma \tag{4.25b}$$

Equation (4.24) becomes

$$\left(\left\langle \hat{p}^\dagger \middle| \mathcal{L}'(\omega)\hat{p} \right\rangle + \int_\Gamma \hat{p}^{\dagger *} \frac{i\bar{c}}{Z}\hat{p}\,\mathrm{d}S\right)\omega' + \int_{\Gamma_1} \hat{p}^{\dagger *}\bar{c}^2\left(\boldsymbol{\nabla}\hat{p}\cdot\boldsymbol{\nabla}_\Gamma C - C\frac{\partial^2\hat{p}}{\partial n^2} - C\frac{i\omega}{\bar{c}^2 Z}\frac{\partial \bar{c}}{\partial n}\hat{p} + \frac{i\omega}{\bar{c}Z}C\frac{\partial \hat{p}}{\partial n}\right)\mathrm{d}S = 0 \tag{4.26}$$

We can impose a normalization condition on the adjoint eigenfunction. For simple eigenvalues

$$\left\langle \hat{p}^\dagger \middle| \mathcal{L}'(\omega)\hat{p} \right\rangle + \int_\Gamma \hat{p}^{\dagger *}\frac{i\bar{c}}{Z}\hat{p}\,\mathrm{d}S = 1 \tag{4.27}$$

We discuss semi-simple degenerate eigenvalues in the next section. We use the direct and the adjoint boundary conditions, Eqs. (4.9b) and (4.25b), to eliminate the eigenvalue, ω, from the last two terms of Eq. (4.26).

$$\omega' = \int_{\Gamma_1}\left(-\hat{p}^{\dagger *}\bar{c}^2\boldsymbol{\nabla}\hat{p}\cdot\boldsymbol{\nabla}_\Gamma C + C\hat{p}^{\dagger *}\bar{c}^2\frac{\partial^2\hat{p}}{\partial n^2} + C\hat{p}^{\dagger *}\bar{c}\frac{\partial\bar{c}}{\partial n}\frac{\partial\hat{p}}{\partial n} - C\frac{\partial\hat{p}^{\dagger *}}{\partial n}\bar{c}^2\frac{\partial\hat{p}}{\partial n}\right)\mathrm{d}S \tag{4.28}$$

The eigenvalue sensitivity, or shape derivative, is now written as a functional of $\hat{p}$ and $\hat{p}^\dagger$. The first term under the integral sign is, however, not yet in Hadamard form. We apply the tangential Stokes formula, Eq. (4.8), with $f = C$ and $\boldsymbol{v} = \hat{p}^{\dagger *}\bar{c}^2\boldsymbol{\nabla}\hat{p}$. We obtain the shape derivative in Hadamard form.

$$\omega' = \int_{\Gamma_1} C\left(-\kappa\hat{p}^{\dagger *}\bar{c}^2\frac{\partial\hat{p}}{\partial n} + \mathrm{div}_\Gamma\left(\hat{p}^{\dagger *}\bar{c}^2\boldsymbol{\nabla}\hat{p}\right) + \hat{p}^{\dagger *}\bar{c}^2\frac{\partial^2\hat{p}}{\partial n^2} + \hat{p}^{\dagger *}\bar{c}\frac{\partial\bar{c}}{\partial n}\frac{\partial\hat{p}}{\partial n} - \frac{\partial\hat{p}^{\dagger *}}{\partial n}\bar{c}^2\frac{\partial\hat{p}}{\partial n}\right)\mathrm{d}S \tag{4.29}$$

Equation (4.29) can be rearranged and possibly simplified. By definition of tangential divergence,

$$\mathrm{div}_\Gamma\left(\hat{p}^{\dagger *}\bar{c}^2\boldsymbol{\nabla}\hat{p}\right) = \boldsymbol{\nabla}\cdot\left(\hat{p}^{\dagger *}\bar{c}^2\boldsymbol{\nabla}\hat{p}\right) - \left((\boldsymbol{n}\cdot\boldsymbol{\nabla})\left(\hat{p}^{\dagger *}\bar{c}^2\boldsymbol{\nabla}\hat{p}\right)\right)\cdot\boldsymbol{n} \tag{4.30}$$

Using index notation, the second term is

$$\begin{aligned}\Big((\boldsymbol{n}\cdot\boldsymbol{\nabla})\Big(\hat{p}^{\dagger^*}\bar{c}^2\boldsymbol{\nabla}\hat{p}\Big)\Big)\cdot\boldsymbol{n} &= n_j\frac{\partial}{\partial x_j}\left(\hat{p}^{\dagger^*}\bar{c}^2\frac{\partial\hat{p}}{\partial x_i}\right)n_i \\ &= n_j\frac{\partial\hat{p}^{\dagger^*}}{\partial x_j}\bar{c}^2\frac{\partial\hat{p}}{\partial x_i}n_i + 2n_j\hat{p}^{\dagger^*}\bar{c}\frac{\partial\bar{c}}{\partial x_j}\frac{\partial\hat{p}}{\partial x_i}n_i + n_j\hat{p}^{\dagger^*}\bar{c}^2\frac{\partial^2\hat{p}}{\partial x_j\partial x_i}n_i \\ &= \frac{\partial\hat{p}^{\dagger^*}}{\partial n}\bar{c}^2\frac{\partial\hat{p}}{\partial n} + 2\hat{p}^{\dagger^*}\bar{c}\frac{\partial\bar{c}}{\partial n}\frac{\partial\hat{p}}{\partial n} + \hat{p}^{\dagger^*}\bar{c}^2\frac{\partial^2\hat{p}}{\partial n^2}\end{aligned} \tag{4.31}$$

And

$$\operatorname{div}_\Gamma\left(\hat{p}^{\dagger^*}\bar{c}^2\boldsymbol{\nabla}\hat{p}\right) = \boldsymbol{\nabla}\cdot\left(\hat{p}^{\dagger^*}\bar{c}^2\boldsymbol{\nabla}\hat{p}\right) - \frac{\partial\hat{p}^{\dagger^*}}{\partial n}\bar{c}^2\frac{\partial\hat{p}}{\partial n} - 2\hat{p}^{\dagger^*}\bar{c}\frac{\partial\bar{c}}{\partial n}\frac{\partial\hat{p}}{\partial n} - \hat{p}^{\dagger^*}\bar{c}^2\frac{\partial^2\hat{p}}{\partial n^2} \tag{4.32}$$

If we substitute Eq. (4.32) into Eq. (4.29), then we obtain the final formula for the shape derivative of the eigenvalues of Eq. (4.9).

$$\omega' = \int_{\Gamma_1} C\left(-\hat{p}^{\dagger^*}\left(\kappa\bar{c}^2 + \bar{c}\frac{\partial\bar{c}}{\partial n}\right)\frac{\partial\hat{p}}{\partial n} + \boldsymbol{\nabla}\cdot\left(\hat{p}^{\dagger^*}\bar{c}^2\boldsymbol{\nabla}\hat{p}\right) - 2\frac{\partial\hat{p}^{\dagger^*}}{\partial n}\bar{c}^2\frac{\partial\hat{p}}{\partial n}\right)\mathrm{d}S \tag{4.33}$$

The shape derivative for the Dirichlet and the Neumann boundary conditions are special cases of Equation (4.33). When applying Dirichlet boundary conditions, $\hat{p} = 0$, $\hat{p}^\dagger = 0$, $\boldsymbol{\nabla}\hat{p} = \partial\hat{p}/\partial n\,\boldsymbol{n}$ and $\boldsymbol{\nabla}\hat{p}^\dagger = \partial\hat{p}^\dagger/\partial n\,\boldsymbol{n}$. In fact, $\hat{p}$ is constant along the boundary and the tangential gradient (derivative in the tangential direction) is zero. We obtain

$$\omega' = -\int_{\Gamma_1} C\left(\frac{\partial\hat{p}^{\dagger^*}}{\partial n}\bar{c}^2\frac{\partial\hat{p}}{\partial n}\right)\mathrm{d}S \tag{4.34}$$

When applying Neumann boundary conditions, $\partial\hat{p}/\partial n = 0$ and $\partial\hat{p}^\dagger/\partial n = 0$, and we obtain

$$\omega' = \int_{\Gamma_1} C\left(\boldsymbol{\nabla}\cdot\left(\hat{p}^{\dagger^*}\bar{c}^2\boldsymbol{\nabla}\hat{p}\right)\right)\mathrm{d}S \tag{4.35}$$

If $\hat{q} = 0$, we obtain from Eq. (2.18)

$$\omega' = \int_{\Gamma_1} C\left(\bar{c}^2\boldsymbol{\nabla}\hat{p}^{\dagger^*}\cdot\boldsymbol{\nabla}\hat{p} - \omega^2\hat{p}^{\dagger^*}\hat{p}\right)\mathrm{d}S \tag{4.36}$$

4.3.3 The 2-fold degenerate case

To illustrate the semi-simple degenerate case, we write the formula for the eigenvalue shape derivative in Hadamard form

$$\int_{\Gamma_1} C\, G(\hat{p}^\dagger, \hat{p})\, \mathrm{d}S - \omega' \left(\left\langle \hat{p}^\dagger \middle| \mathcal{L}'(\omega) \hat{p} \right\rangle + \int_\Gamma \hat{p}^{\dagger *} \frac{i\bar{c}}{Z} \hat{p}\, \mathrm{d}S \right) = 0 \tag{4.37}$$

For repeated eigenvalues, which are two-fold degenerate in this case, the eigenfunction $\hat{p}$ is given by the linear combination (Grinfeld, 2010)

$$\hat{p} = \alpha_1 \hat{p}_1 + \alpha_2 \hat{p}_2 = \sum_{j=1}^{2} \alpha_j \hat{p}_j \tag{4.38}$$

where $\hat{p}_1$ and $\hat{p}_2$ are the independent eigenfunctions associated with the repeated eigenvalue ω and α_1 and α_2 are complex numbers. The same applies to the adjoint eigenfunction $\hat{p}^\dagger$. We substitute these linear combinations into (4.37)

$$\alpha_i^* \left(\int_{\Gamma_1} C\, G(\hat{p}_i^\dagger, \hat{p}_j)\, \mathrm{d}S - \omega' \left(\left\langle \hat{p}^\dagger \middle| \mathcal{L}'(\omega) \hat{p} \right\rangle + \int_\Gamma \hat{p}^{\dagger *} \frac{i\bar{c}}{Z} \hat{p}\, \mathrm{d}S \right) \right) \alpha_j = 0 \tag{4.39}$$

The shape gradient now has four components. We can normalize the bases of the two eigenspaces (direct and adjoint) such that they become biorthonormal

$$\left\langle \hat{p}^\dagger \middle| \mathcal{L}'(\omega) \hat{p} \right\rangle + \int_\Gamma \hat{p}^{\dagger *} \frac{i\bar{c}}{Z} \hat{p}\, \mathrm{d}S = \delta_{ij} \tag{4.40}$$

We are left with a 2×2 eigenvalue problem for the shape derivative ω'

$$\left(\int_{\Gamma_1} C\, G(\hat{p}_i^\dagger, \hat{p}_j)\, \mathrm{d}S - \omega' \delta_{ij} \right) \alpha_j = 0 \tag{4.41}$$

4.4 Shape derivatives of the Helmholtz equation in a unit square

In this section we apply the Hadamard formula/theorem to calculate analytically the shape derivatives of the eigenvalues of the Helmholtz equation in a unit square domain with homogeneous Dirichlet boundary conditions for normal boundary perturbations proportional to the shape gradients. The equation and the boundary conditions read

$$\nabla^2 \hat{p} + k^2 \hat{p} = 0 \quad \text{in } \Omega \tag{4.42}$$

$$\hat{p} = 0 \quad \text{on } \partial\Omega \tag{4.43}$$

The eigenvalues and their associated eigenfunctions are

$$k_{m,n} = \pi\sqrt{m^2 + n^2} \tag{4.44}$$

$$\hat{p}_{m,n}(x, y) = \sin(m\pi x)\sin(n\pi y) \tag{4.45}$$

where m and n are the two wavenumbers. The spectrum, i.e. the set of all the eigenfrequencies, contains both simple and semi-simple degenerate eigenvalues. We focus on the simple eigenmode with wavenumbers (1, 1), and the semi-simple degenerate eigenmode with wavenumbers (1, 2) and (2, 1). The eigenfunctions are orthogonal and (are) normalized such that

$$\left\langle \hat{p}_{m,n} \middle| \hat{p}_{m,n} \right\rangle = \frac{1}{4} \tag{4.46}$$

4.4.1 Uniform boundary perturbations

If we shrink the unit square domain in the y-direction, the width will be $1 - \varepsilon$, with $\varepsilon \ll 1$, and the eigenvalue

$$k_{m,n}(\varepsilon) = \pi\sqrt{m^2 + \left(\frac{n}{1-\varepsilon}\right)^2} \tag{4.47}$$

The first-order eigenvalue sensitivity (shape derivative) is straightforwardly given by the first-order coefficient of the McLaurin series

$$k'_{m,n}(0) = \pi\frac{n^2}{\sqrt{m^2 + n^2}} \tag{4.48}$$

For the first mode, which is simple, the shape derivatives is

$$k'_{1,1}(0) = \frac{\pi}{\sqrt{2}} \approx 2.2 \tag{4.49}$$

For the second eigenmode, which is semi-simple degenerate, the eigenvalues split and the shape derivatives are

$$k'_{1,2}(0) = \frac{4\pi}{\sqrt{5}} \approx 5.6 \tag{4.50}$$

$$k'_{2,1}(0) = \frac{\pi}{\sqrt{5}} \approx 1.4 \tag{4.51}$$

These simple results are useful for example when debugging.

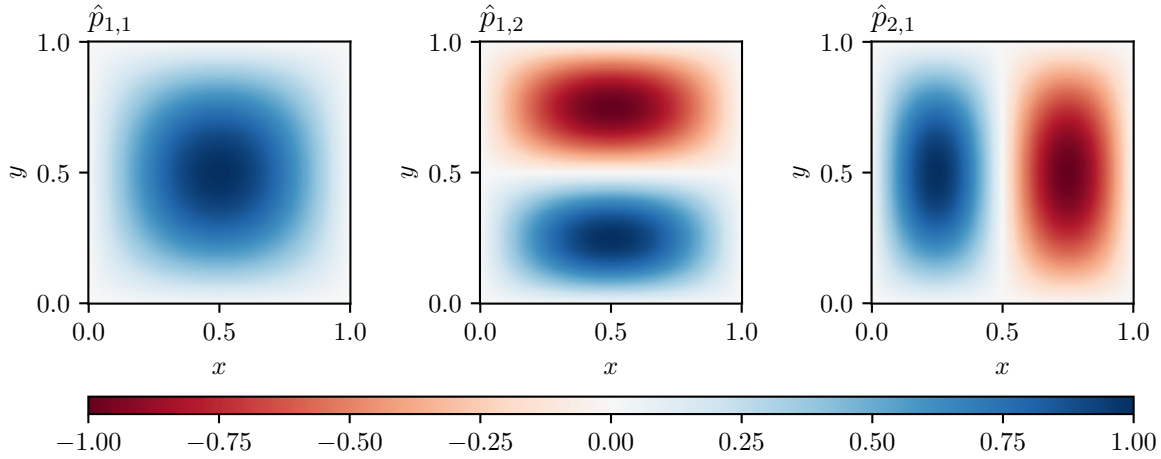

Fig. 4.1 First three eigenfunctions of the Helmholtz equation in a unit square domain with homogeneous Dirichlet boundary conditions. The associated eigenvalues are $k_{1,1} = \pi\sqrt{2}$, $k_{1,2} = \pi\sqrt{5}$ and $k_{2,1} = \pi\sqrt{5}$.

4.4.2 Boundary perturbations proportional to the shape gradients

In this subsection we first calculate the shape gradients for both eigenmodes and then the shape derivatives for normal boundary perturbations proportional to the shape gradients. We start by writing eigenvalues and eigenfunctions.

$$k_{1,1} = \pi\sqrt{2}, \quad \hat{p}_{1,1} = \sin(\pi x)\sin(\pi y) \tag{4.52}$$

$$k_{1,2} = \pi\sqrt{5}, \quad \hat{p}_{1,2} = \sin(\pi x)\sin(2\pi y) \tag{4.53}$$

$$k_{2,1} = \pi\sqrt{5}, \quad \hat{p}_{2,1} = \sin(2\pi x)\sin(\pi y) \tag{4.54}$$

The eigenfunctions are shown in Fig. 4.1. The shape gradient reads

$$G = \frac{2}{k}\frac{\partial \hat{p}^\dagger}{\partial n}\frac{\partial \hat{p}}{\partial n} \tag{4.55}$$

The problem is self-adjoint, therefore $\hat{p}^\dagger \equiv \hat{p}$. We study two cases: case (a) consists in perturbations to the bottom boundary and case (b) in perturbations to the left boundary. The normal derivatives of the eigenfunctions at the two boundaries (bottom and left), remembering that the unit normal vector points outwards, are

a)

$$\frac{\partial \hat{p}}{\partial n} = -\left.\frac{\partial \hat{p}}{\partial y}\right|_{y=0} = -n\pi\sin(m\pi x) \tag{4.56}$$

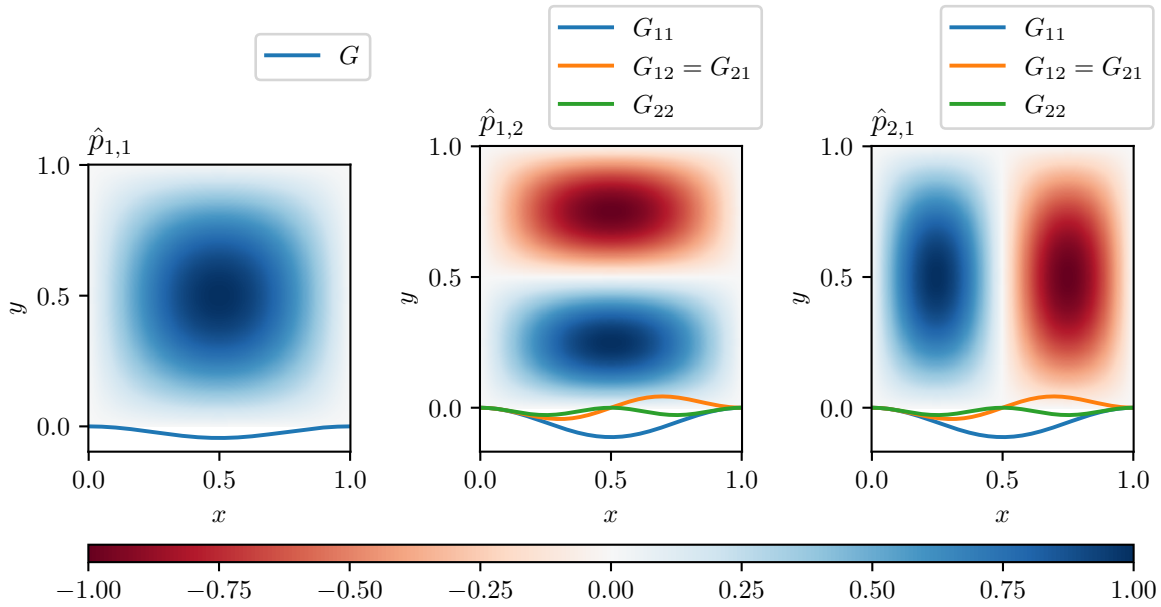

Fig. 4.2 Shape gradients of the first two eigenvalues of the Helmholtz equation at the bottom boundary. For ease of visualizion, we plot the shape gradients with the opposite sign.

b)

$$\frac{\partial \hat{p}}{\partial n} = -\frac{\partial \hat{p}}{\partial x}\bigg|_{x=0} = -m\pi \sin(n\pi y) \tag{4.57}$$

The shape gradient of the first mode is

a)

$$G = \pi\sqrt{2}\sin^2(\pi x) \tag{4.58}$$

b)

$$G = \pi\sqrt{2}\sin^2(\pi y) \tag{4.59}$$

The shape gradients of the second mode are

a)

$$\begin{pmatrix} G_{11} & G_{12} \\ G_{21} & G_{22} \end{pmatrix} = \frac{2\pi}{\sqrt{5}} \begin{pmatrix} 4\sin^2(\pi x) & 2\sin(\pi x)\sin(2\pi x) \\ 2\sin(2\pi x)\sin(\pi x) & \sin^2(2\pi x) \end{pmatrix} \tag{4.60}$$

b)

$$\begin{pmatrix} G_{11} & G_{12} \\ G_{21} & G_{22} \end{pmatrix} = \frac{2\pi}{\sqrt{5}} \begin{pmatrix} \sin^2(2\pi y) & 2\sin(2\pi y)\sin(\pi y) \\ 2\sin(\pi y)\sin(2\pi y) & 4\sin^2(\pi y) \end{pmatrix} \tag{4.61}$$

The shape gradients of the first and second mode for case (a) are shown in Fig. 4.2. Now we want to calculate the shape derivatives for boundary displacements proportional to the shape gradients. We normalize the displacements such that $\int |C| \, \mathrm{d}S = 1$. The normalized

Table 4.1 Shape derivatives for perturbations to the bottom boundary

$C \propto$	$k'_{1,2}$	$k'_{2,1}$
const	5.6	1.4
$G_{11} = 2\sin^2(\pi x)$	8.4	1.4
$G_{12} = G_{21} = \frac{3\pi}{4}\sin(\pi x)\sin(2\pi x)$	3.3	−3.3
$G_{22} = 2\sin^2(2\pi x)$	5.6	2.1

displacement for the first eigenmode is

$$C \propto G = 2\sin^2(\pi x) \tag{4.62}$$

And the shape derivative is

$$k'_{1,1} = \frac{3\pi\sqrt{2}}{4} \approx 3.3 \tag{4.63}$$

This value is larger than the shape derivative for a boundary perturbation that transforms the square into a rectangle. The shape derivatives of the second eigenmode are the eigenvalues of a 2×2 matrix. The normalized displacements and the shape derivatives are

$$C \propto G_{11} = 2\sin^2(\pi x) \tag{4.64}$$

$$\frac{2\pi}{\sqrt{5}}\begin{pmatrix} 3 & 0 \\ 0 & \frac{1}{2} \end{pmatrix} \longrightarrow k'_{1,2} = \frac{6\pi}{\sqrt{5}} \approx 8.4,\ k'_{2,1} = \frac{\pi}{\sqrt{5}} \approx 1.4 \tag{4.65}$$

$$C \propto G_{12} = \frac{3\pi}{4}\sin(\pi x)\sin(2\pi x) \tag{4.66}$$

$$\frac{2\pi}{\sqrt{5}}\begin{pmatrix} 0 & \frac{3\pi}{8} \\ \frac{3\pi}{8} & 0 \end{pmatrix} \longrightarrow k'_{1,2} = k'_{2,1} = \pm\frac{3\pi^2}{4\sqrt{5}} \approx \pm 3.3 \tag{4.67}$$

$$C \propto G_{22} = 2\sin^2(2\pi x) \tag{4.68}$$

$$\frac{2\pi}{\sqrt{5}}\begin{pmatrix} 2 & 0 \\ 0 & \frac{3}{4} \end{pmatrix} \longrightarrow k'_{1,2} = \frac{4\pi}{\sqrt{5}} \approx 5.6,\ k'_{2,1} = \frac{3\pi}{2\sqrt{5}} \approx 2.1 \tag{4.69}$$

The shape derivatives are summarized in Table 4.1 and Table 4.2. Perturbations proportional to G_{11} cause the maximum drift of the eigenvalue $k_{1,2}$, associated with the first eigenvector. Perturbations proportional to G_{22} cause the maximum drift of the eigenvalue $k_{2,1}$, associated with the second eigenvector. The shape derivatives associated with perturbations proportional

Table 4.2 Shape derivatives for perturbations to the left boundary

$C \propto$	$k'_{1,2}$	$k'_{2,1}$
const	1.4	5.6
$G_{11} = 2\sin^2(2\pi y)$	2.1	5.6
$G_{12} = G_{21} = \frac{3\pi}{4}\sin(\pi y)\sin(2\pi y)$	−3.3	3.3
$G_{22} = 2\sin^2(\pi y)$	1.4	8.4

to G_{12} and G_{21} are, apart from the sign, the same for $k_{1,2}$ and $k_{2,1}$. If we consider perturbations applied to the left boundary, rather than the bottom boundary, perturbations proportional to G_{22} have on $k_{2,1}$ the same effect that perturbations proportional to G_{11} have on $k_{1,2}$, and so forth.

In the case of a circumferential geometry, there would not be this difference because there is only one boundary. In addition to this, a boundary perturbation as simple as a radius increase (decrease) would not break the symmetry. This will be explained in detail in Chapter 6.

Chapter 5

Rijke tube and turbulent swirl combustor

This chapter is based on the results published in (Falco and Juniper, 2021a). We consider two-dimensional planar models of an electrically heated Rijke tube and a turbulent swirl combustor. They are both longitudinally unstable. In both cases, we parametrize the combustor walls using B-splines and apply shape changes proportional to the eigenvalue shape derivatives to reduce the eigenvalue growth rate and eventually make the mode stable.

5.1 Rijke tube

The first case is a model of an electrically heated Rijke tube (Rijke, 1859) taken from (Juniper, 2018). The model is based on the experiments conducted by Rigas et al. (2016) to measure the sensitivity of the frequencies and growth rates to passive feedback control in the form of a drag device, previously computed by Magri and Juniper (2013) using adjoint-based sensitivity analysis applied to a Galerkin model of the thermo-acoustic waves. In the experiments, the Mach number was less than 0.003. Therefore the assumption of zero Mach number base flow is valid.

5.1.1 Model description

We impose Neumann boundary conditions at the radial walls and Robin boundary conditions at the inlet and outlet boundaries. Table 5.1 contains all the parameters of the model. x_f denotes the position of the hot wire and a_f is the standard deviation of the heat release rate distribution, which is homogeneous in the radial direction. d_f is the diameter of the duct at the heat source. x_r denotes the reference point and a_r is the standard deviation of the weight function (reference region). The standard deviation is the same in the longitudinal and in the radial direction. $\bar{\rho}_u$

Table 5.1 Rijke tube

l	1.0	[m]
d	0.047	[m]
r	287	[J kg^{-1} K^{-1}]
γ	1.4	
p_a	1.0×10^5	[Pa]
ρ_a	1.22	[kg m^{-3}]
$\bar{\rho}_u$	1.22	[kg m^{-3}]
$\bar{\rho}_d$	0.85	[kg m^{-3}]
R_u	$-0.975 + 0.05i$	
R_d	$-0.975 + 0.05i$	
$\dot{Q}_t$	200	[W]
U_b	0.1	[m s^{-1}]
N	0.014	
τ	1.5×10^{-3}	[s]
x_f	0.25	[m]
a_f	0.025	[m]
x_r	0.2	[m]
a_r	0.0047	[m]

and $\bar{\rho}_d$ denote the mean density in the cold upstream region and in the hot downstream region, respectively.

The mean density, which is homogeneous in the radial direction, is

$$\bar{\rho}(x, y) = \bar{\rho}_d + \frac{\bar{\rho}_d - \bar{\rho}_u}{2}\left[1 + \tanh\left(\frac{x - x_f}{a_f}\right)\right] \tag{5.1}$$

The distribution of the heat release rate across the hot wire is

$$v(x, y) = \frac{1}{d_f a_f \sqrt{2\pi}} \exp\left(-\frac{(x - x_f)^2}{2a_f^2}\right) \tag{5.2}$$

The weight function (reference region) is

$$w(x, y) = \frac{1}{a_r^2 2\pi} \exp\left(-\frac{(x - x_r)^2 + y^2}{2a_r^2}\right) \tag{5.3}$$

w is a Gaussian function. It vanishes at infinity but it does not have compact support. However, its standard deviation, a_r, is small and we restrict w so that it is zero at the boundary.

Figure 5.1 shows the mean density, $\bar{\rho}$, the distribution of the heat release rate, v, and the weight function, w, for the two-dimensional model of the Rijke tube. In two dimensions, the nondimensional interaction index, N, is divided by $\pi/4d_f$.

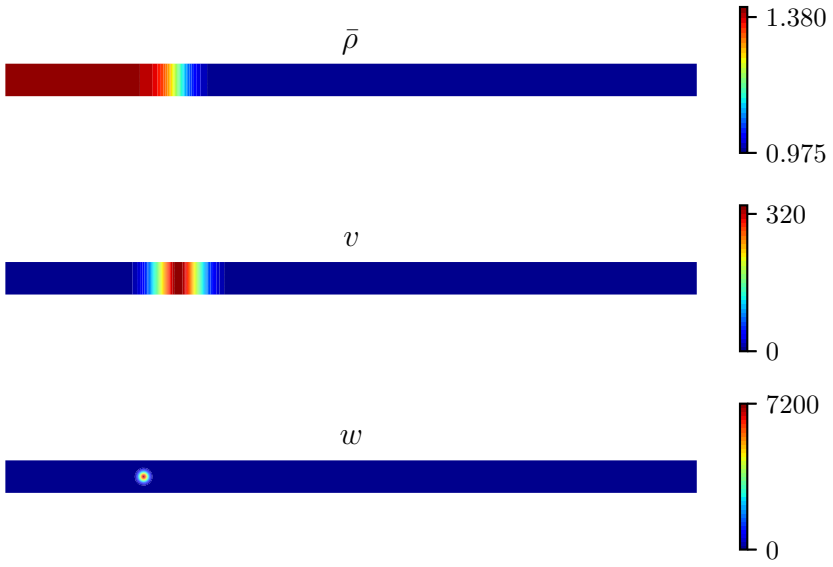

Fig. 5.1 Nondimensional mean density, $\bar{\rho}$, distribution of the heat release rate, v, and weight function (reference region), w, in the two-dimensional model of the electrically heated Rijke tube.

5.1.2 Shape sensitivity analysis and shape changes

We define two sets of control points, one for the top boundary and one for the bottom boundary. Then we parametrize the two boundaries using 3$^{\text{rd}}$ order uniform non-rational B-splines (see Appendix B). The inlet and the outlet boundary are fixed.

We compute the first direct and adjoint eigenmode of the thermoacoustic system, which is unstable. The associated nondimensional eigenvalue is $\omega = 3.539521 + i0.001984$. The results match those of the one-dimensional model in (Juniper, 2018) and have been checked against the finite volume Helmholtz solver AVSP (Nicoud et al., 2007). Then, using Eq. (4.35), we calculate the shape derivatives for each control point. Fig. 5.2 shows the real and the imaginary part of the shape derivatives for each control point as vectors. As expected, they are all orthogonal to the boundary. In fact, a tangential displacement would only result in a reparametrization of the boundary, without changing its shape or affecting the eigenvalue. The real part of the shape derivatives gives the direction of greatest positive change of the angular frequency of the mode. The imaginary part gives the direction of greatest positive change of

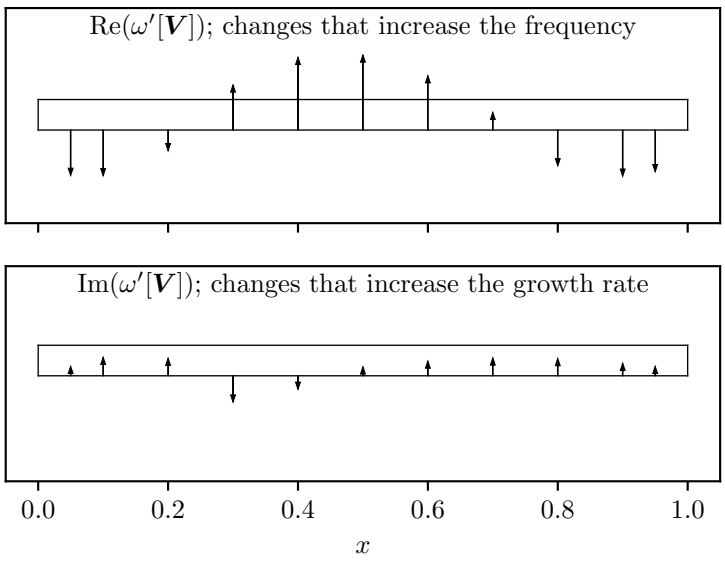

Fig. 5.2 Real (top) and imaginary (bottom) part of the eigenvalue shape derivatives for each control point at the bottom boundary of the Rijke tube. The real part gives the influence on the frequency and the imaginary part gives the influence on the growth rate.

the growth rate of the mode. Therefore, we move the control points in the opposite direction of the imaginary part of the shape derivatives. This reduces the growth rate and eventually makes the mode stable. The eigenvalue becomes stable after 3 iterations. However, we continue to iterate in order to accentuate the boundary deformations so that the differences between the two shapes and between the two eigenvectors are more visible. Fig. 5.3 shows the non-deformed and the deformed boundary after 10 iterations. Fig. 5.4 shows the modulus of the pressure eigenvector, along the longitudinal axis, before and after the iteration.

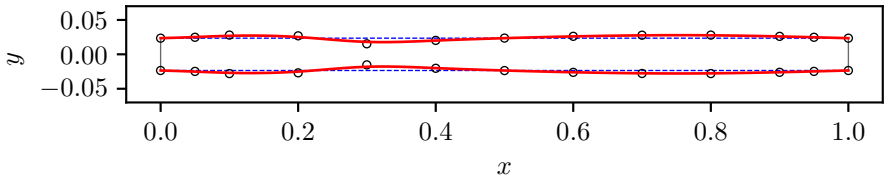

Fig. 5.3 Initial (- -) and final (—) boundary of the Rijke tube after 10 iterations. The circles represent the control points of the final boundary. The control points at the inlet and outlet boundary are fixed.

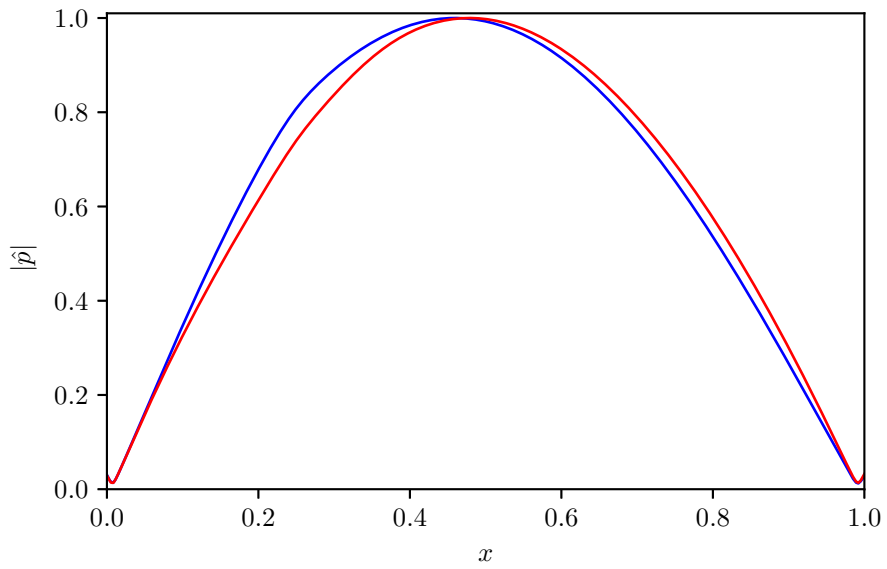

Fig. 5.4 Modulus of the pressure eigenfunction, $\hat{p}$, associated with the first thermoacoustic mode of the electrically heated Rijke tube, for the initial (—) and the final domain (—), after 10 iterations. The associated nondimensional eigenvalues are $\omega_\Omega = 3.539521 + i0.001984$ and $\omega_{\Omega_t} = 3.688497 - i0.009876$, respectively.

5.1.3 Results interpretation

We use Eq. (2.36) to interpret the results. In the $n-\tau$ model, the gain of the flame transfer function is constant and equal to the interaction index, N. Both the modulus of the pressure at the position of the heat source, $\boldsymbol{x}_f$, and the modulus of the longitudinal component of the velocity at the reference point, $\boldsymbol{x}_r$, are smaller in the final domain than in the initial domain. The phase angle difference between the heat release rate and the pressure at the position of the heat source, $\boldsymbol{x}_f$, increases from $\sim 12°$ to $\sim 16°$. Finally, the quantity $\left|\hat{p}^2\right|$ increases at the outlet boundary and slightly decreases at the inlet boundary. Overall, in the final domain, the heat release rate oscillations are smaller in absolute value and less in phase with the pressure oscillations than in the initial domain, and the acoustic losses due to acoustic radiation from the boundaries are larger.

5.2 Turbulent swirl combustor

The second case is a model of a laboratory-scale turbulent swirl combustor at Laboratoire EM2C (CentraleSupélec) in Paris, France. This combustor has been extensively studied in the context of combustion instabilities. In particular, experimental, theoretical and numerical nonlinear stability analysis of limit cycles (Palies et al., 2010; Silva et al., 2013), dynamics of turbulent

Table 5.2 Turbulent swirl combustor

l_1	0.096	[m]
l_2	0.0675	[m]
l_3	0.078	[m]
l_4	0.4	[m]
d_1	0.065	[m]
d_3	0.022	[m]
d_4	0.07	[m]
r	287	[J kg^{-1} K^{-1}]
γ	1.4	
p_{amb}	1.01325×10^5	[Pa]
T_{amb}	300	[K]
T_u	300	[K]
T_d	1600	[K]
R_d	−0.6	
$\dot{Q}_t$	3.03×10^3	[W]
U_b	4.16	[m s^{-1}]
N	1.5	
τ	4.73×10^{-3}	[s]
x_f	0.2515	[m]
a_f	0.002	[m]
x_r	0.2259	[m]
a_r	0.0022	[m]

premixed swirling flames (Palies et al., 2011a) and uncertainty quantification (Avdonin et al., 2018; Mensah et al., 2018a; Silva et al., 2017). It consists of a cylindrical plenum, a convergent duct, a swirler, and a cylindrical combustion chamber. A mixture of methane and air at an equivalence ratio of 0.8 is injected upstream of the plenum. The total power of the flame at the operating point considered in this study is 3.03 kW.

5.2.1 Model description

The parameters of the model, taken from (Avdonin et al., 2018), are given in Table 5.2. This system exhibits an unstable longitudinal mode. The eigenvalue we found with our 2D planar code is $181 + 3.33i$ s^{-1}. We computed the same case in 2D with AVSP and found a complex angular frequency of $182 + 3.28i$ s^{-1}. We impose Neumann boundary conditions at the walls and Robin boundary conditions at the outlet boundary. Figure 5.6 shows the mean density, $\bar{\rho}$, the distribution of the heat release rate, v, and the weight function, w, for the two-dimensional

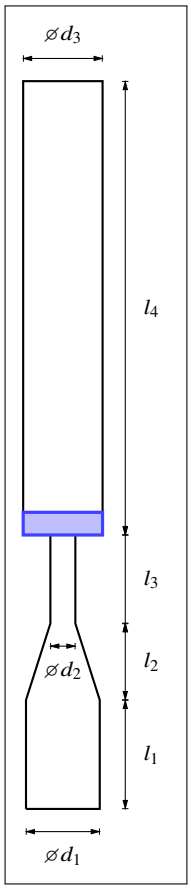

Fig. 5.5 Turbulent swirl combustor

model of the turbulent swirl combustor. Their analytical expression are given in Eqs. (5.1), (5.2) and (5.3), respectively.

5.2.2 Shape sensitivity analysis and shape changes

We parametrize the entire geometry except for the outlet boundary, including more control points where there are sharp corners. We compute the direct and the adjoint eigenmode and apply Eq. (4.35) to find the shape derivatives. Figure 5.7 shows the eigenvalue shape derivatives for each control point. The eigenvalue is more sensitive in the plenum and much more sensitive in the burner than in the combustion chamber. Because the gas is cooler upstream of the temperature jump across the flame, the local wavelength is shorter and therefore geometry modifications have more influence. The shape derivatives indicate that reducing the size of the plenum and increasing the cross sectional area of the burner in the reference region reduces the growth rate. Manufacturers are usually reluctant to alter the geometry of the burner and the

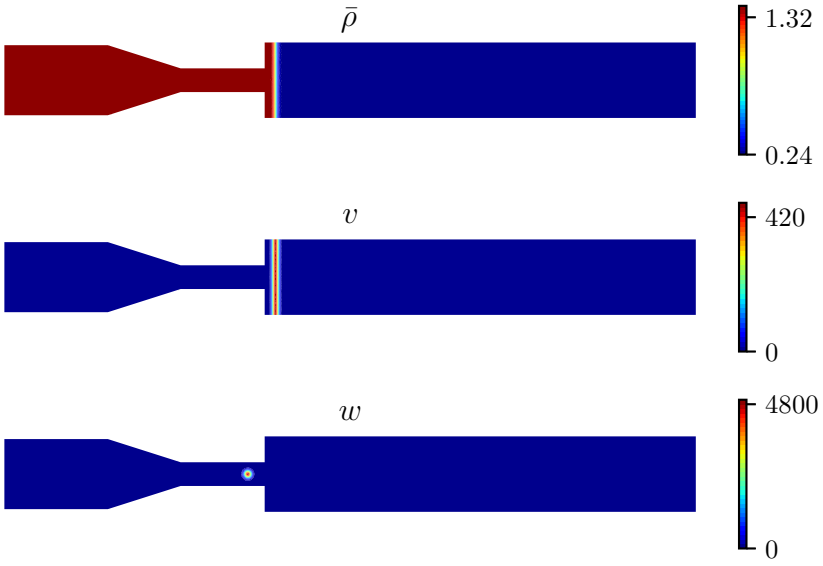

Fig. 5.6 Nondimensional mean density, $\bar{\rho}$, distribution of the heat release rate, v, and weight function (reference region), w, in the two-dimensional model of the turbulent swirl combustor.

combustion chamber because they are determined by other considerations, but they could be willing to modify the geometry of the plenum.

For this reason, we fix the geometry of both the burner and the combustion chamber and allow the geometry of the plenum to vary. The eigenvalue becomes stable after five iterations. Fig. 5.8 (top) shows the initial and the final shape of the turbulent swirl combustor. In the final shape, the control points of the plenum are moved inwards. Fig. 5.8 (bottom) shows the direct and adjoint eigenfunctions for the initial and final domain.

5.2.3 Results interpretation

While the modulus of the pressure at the position of the flame, $\boldsymbol{x}_f$, is bigger in the final domain than in the initial domain, the modulus of the longitudinal component of the velocity at the reference point, $\boldsymbol{x}_r$, is smaller. The phase angle difference between the heat release rate and the pressure at the position of the flame, $\boldsymbol{x}_f$, increases from $\sim 43°$ to $\sim 49°$. Finally, the quantity $\left|\hat{p}^2\right|$ increases at the outlet boundary. Overall, in the final domain, the heat release rate oscillations are less in phase with the pressure oscillations than in the initial domain, and the acoustic losses due to acoustic radiation from the boundaries are larger.

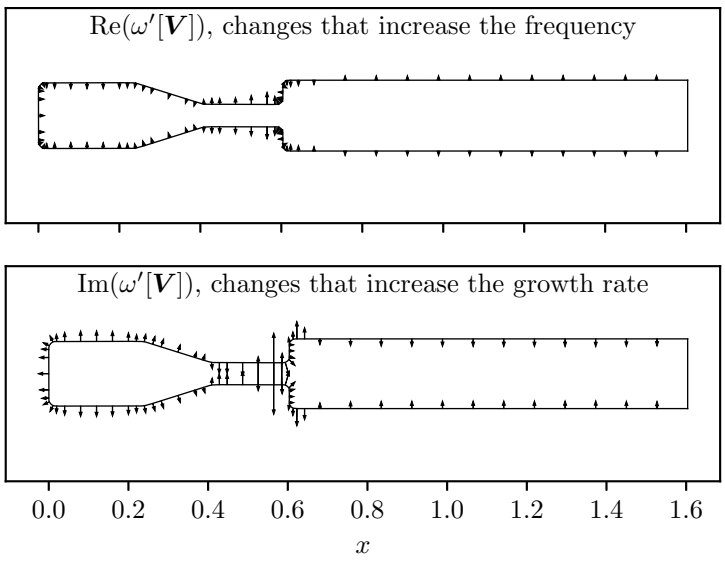

Fig. 5.7 Real (top) and imaginary (bottom) part of the eigenvalue shape derivatives for each control point at the bottom boundary of the turbulent swirl combustor. The real part gives the influence on the frequency and the imaginary part gives the influence on the growth rate.

5.3 Conclusion

In this chapter we have studied two thermoacoustic systems found in the literature: an electrically heated Rijke tube and a turbulent swirl combustor, using two-dimensional planar models. They are both longitudinally unstable. We have parametrized the shapes using B-splines. Then we have expressed the eigenvalue shape derivative in Hadamard form, i.e. for arbitrary shape changes, by combining the direct and the adjoint eigenvector. We have used the Hadamard formula to calculate the derivatives of the eigenvalue with respect to the B-spline parameters. We have stabilized both systems by making small changes to the geometry in the most influential regions, exploiting the fact that thermoacoustic systems are sensitive to small modifications.

We have assumed that the flame transfer function is unaffected by geometry changes. This is reasonable only for changes to the plenum. If geometry changes were to be considered in practice, then a more realistic model of the flame response would need to be included. This would be a flame transfer function with different gain and phase or different geometries.

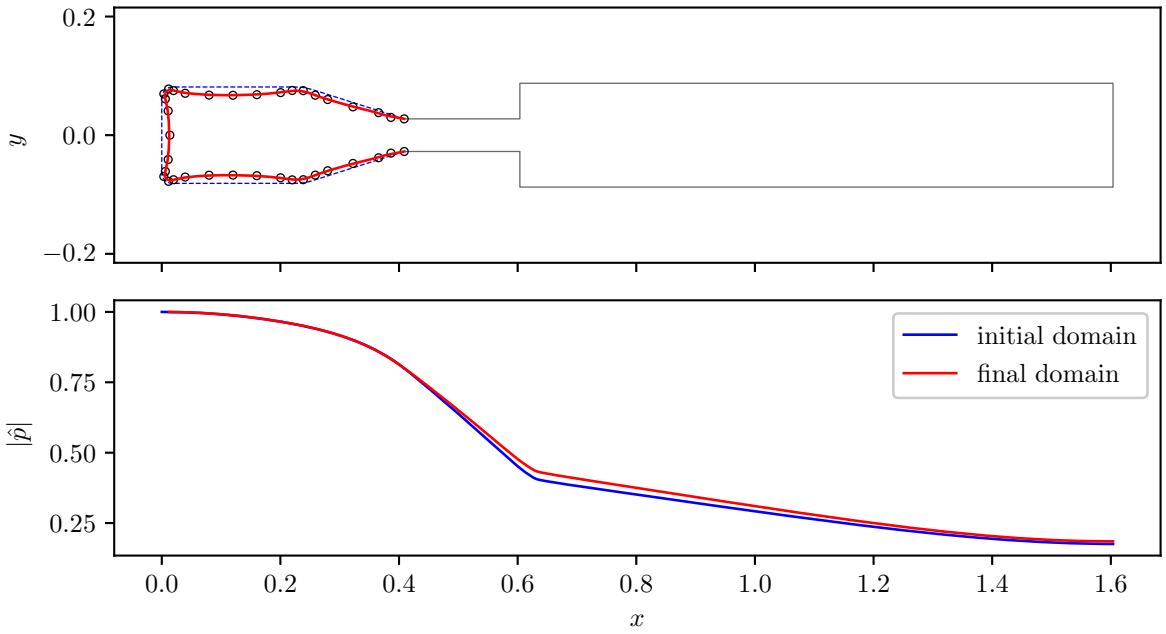

Fig. 5.8 (Top) Initial (- -) and final (—) boundary of the turbulent swirl combustor after 5 iterations. The circles represent the control points of the final boundary. (Bottom) Modulus of the pressure eigenfunction, $\hat{p}$, associated with the first thermoacoustic mode of the turbulent swirl combustor, for the initial (—) and the final domain (—), after 5 iterations. The associated nondimensional eigenvalues are $\omega_\Omega = 1.3157 + 0.0241i$ and $\omega_{\Omega_t} = 1.3644 - 0.0978i$, respectively.

Chapter 6

MICCA annular combustor

Annular combustors, such as gas turbine combustors, feature azimuthal modes. These modes have two travelling directions: clockwise and anticlockwise. Unlike axial combustors, the acoustic modes interact with N flames. Since the length and the circumference of annular chambers are of the same order, the frequency of longitudinal and azimuthal modes can be similar. Azimuthal modes can be standing or spinning, depending on whether the clockwise and anticlockwise modes have similar or different amplitudes. Standing modes have nodes and antinodes, with the result that different burners are subjected to different flucutation amplitudes (or levels). At a pressure antinode, the flame receives axial perturbations, while at a pressure node, the perturbation is transverse. Spinning modes, on the other hand, do not have nodes and antinodes. The fluctuation amplitude is the same for all burners. A standing mode can turn into a spinning mode and vice versa, as demonstrated experimentally by Krebs et al. (2002) in real gas turbines. This phenomenon is called mode switching. It was studied by Staffelbach et al. (2009); Wolf et al. (2012) using large eddy simulation: at the same operating point, azimuthal modes randomly switched between standing and spinning; and experimentally by Worth and Dawson (2013a,b) in a laboratory-scale annular combustor at Cambridge University. A third type of mode, called slanted mode, which is the combination of a standing azimuthal mode and longitudinal mode with the same frequency, was observed experimentally by Bourgouin et al. (2015a).

In this chapter, based on the results in (Falco and Juniper, 2021b), we study the case of a laboratory-scale annular combustor (MICCA), which features an unstable azimuthal standing mode. We perform a shape sensitivity analysis for both symmetry-breaking and symmetry-preserving boundary perturbations. The first are proportional to the elements of the shape gradient matrix. The second consist in changes to lengths and radii. We fix the geometry of the burner and apply symmetry-preserving changes to the plenum and the combustion chamber. By

doing so, we manage to reduce the thermoacoustic growth rate by increasing the phase angle difference between the pressure and heat release rate fluctuations.

6.1 The MICCA combustor

The MICCA combustor is a laboratory-scale annular combustor at Laboratoire EM2C (CentraleSupélec) in Paris, France. Stable thermoacoustic limit cycles of standing and spinning azimuthal modes are observed at some operating conditions (Bourgouin et al., 2015a,b; Durox et al., 2013). The MICCA combustor consists of an annular plenum, 16 injectors and an annular combustion chamber. Each injector consists of a cylinder and a perforated plate.

Following (Laera et al., 2017), we replace in the discrete model the perforated plate with a cylindrical volume. Fig. 6.1 shows a slice section view of one sector of the numerical model of the MICCA combustor. We consider the same operating conditions as operating point B in Laera et al. (2017). A standing mode with a stable limit cycle at a frequency of 489 Hz is observed in the experiments. The equivalence ratio of the mixture of propane and air is $\phi = 1.11$. The total power of the flame for each burner is $\dot{Q}_t = 2.08$ kW, and the bulk flow velocity is $U_b = 0.66$ m/s. The mean temperature in the plenum and in the injectors is $\bar{T} = 300$ K. The temperature profile in the combustion chamber is parabolic, monotonically decreasing between the values $\bar{T} = 1520$ K at the chamber back plane and $\bar{T} = 1200$ K at the chamber outlet.

The experimental flame describing function (FDF) depends on the frequency of the excitation and on the ratio of the root mean square of the velocity fluctuation measured at the reference point, u', to the average flow velocity in the injector, $\bar{u}$. We obtain the experimental flame transfer function (FTF) from the FDF, considering a small forcing amplitude, $|u'/\bar{u}| = 0.1$. As explained in Section 2.2, the experimental FTF is the frequency response given at real-valued frequencies, while the transfer function, $F(\omega)$, is defined in the complex plane. In order to calculate the first derivative of the linear operator, $\mathcal{L}(\omega)$, with respect to the eigenvalue, ω, exactly, we need the transfer function to be analytic in the complex plane. We obtain an analytic transfer function by applying the Vector Fitting algorithm (Gustavsen, 2006; Gustavsen and Semlyen, 1999) to the frequency response. The experimental FTF and the transfer function (of the linear state-space model) are shown in Fig. 6.2.

We impose Neumann boundary conditions at the combustor walls. Laera et al. (2017) added in the discrete model an end correction to the length of the combustion chamber and imposed Dirichlet boundary conditions at the outlet boundary. We do not add any end correction and instead we impose Robin boundary conditions. We tune the specific acoustic impedance by matching the angular frequency and the absolute value of the normalized eigenvector of the first

longitudinal (1L) and first azimuthal (1A) acoustic modes with the case with end correction and Dirichlet boundary conditions. The value of the reflection coefficient is $R = -0.875 - 0.210i$.

Symmetric annular combustors present a discrete rotational symmetry. When generating the mesh, we start with half sector and apply a reflection. Then we copy and rotate the single sector ($n - 1$ times). The mesh we obtain features a rotational symmetry of order n.

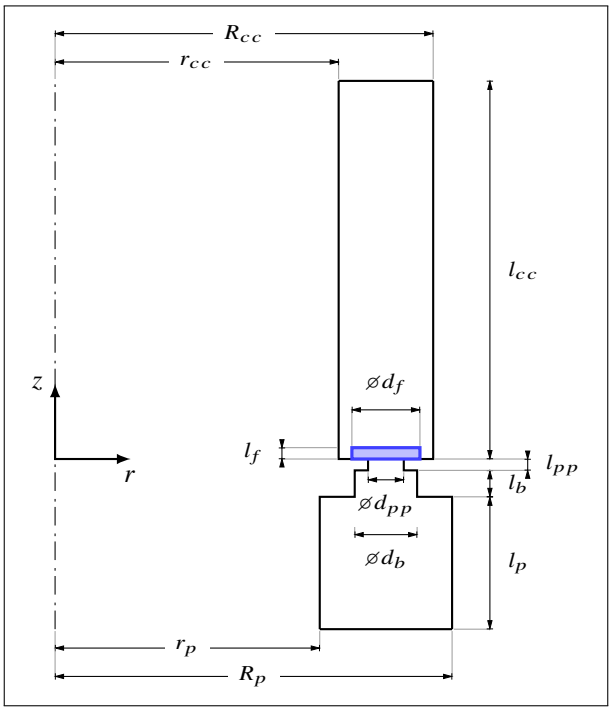

Fig. 6.1 Slice section view of one sector of the MICCA combustor. The dash-dotted line is the axis of symmetry. The subscripts stand for: plenum (p), burner (b), perforated plate (pp), flame (f), combustion chamber (cc).

The thermoacoustic mode we examine is a plenum-dominant azimuthal mode (1A) with frequency of 506 Hz and growth rate of 504 rad s^{-1}. Because of the discrete rotational symmetry of the annular combustor, the mode is degenerate with algebraic and geometric multiplicity equal to 2. We normalize the eigenvector, $\hat{p}$, such that $\langle \hat{p} | \hat{p} \rangle = 1$. Fig. 6.3 shows the real part of the eigenvector, $\hat{p}$. We want to reduce the growth rate of this mode by modifying the geometry of the annular combustor.

6.2 Preliminary shape sensitivity analysis

When using a non-parametric approach, the boundary displacement is proportional to the shape gradient. When using a parametric approach, as in the case of B-spline or NURBS surfaces,

Table 6.1 MICCA annular combustor

r_p	0.14	[m]
R_p	0.21	[m]
l_p	0.07	[m]
d_b	0.033	[m]
l_b	0.014	[m]
d_{pp}	0.0189	[m]
l_{pp}	0.006	[m]
d_f	0.036	[m]
l_f	0.006	[m]
r_{cc}	0.15	[m]
R_{cc}	0.2	[m]
l_{cc}	0.2	[m]
r	287	[J kg^{-1} K^{-1}]
γ	1.4	
p_{amb}	1.01325×10^5	[Pa]
T_{amb}	300	[K]
T_u	300	[K]
T_d	$1521 - 321(z/l_{cc})^2$	[K]
R	$-0.875 - 0.210i$	
$\dot{Q}_t$	2.08×10^3	[W]
U_b	0.66	[m s^{-1}]
z_f	0.0	[m]
z_r	-0.02	[m]

the set of admissible boundary displacements and shapes is reduced (see Appendix B for more details). The boundary perturbation, $\boldsymbol{V}_i$, is the derivative of the surface with respect to the position of the i-th control point. The shape derivative in the direction $\boldsymbol{V}_i$ is the shape derivative with respect to the i-th control point.

In the case of simple eigenvalues, the shape gradient is the eigenvalue sensitivity to normal boundary perturbations. The upper bound of the shape derivative is given by the shape derivative for a boundary perturbation proportional to the shape gradient. We obtain an upper bound for the angular frequency drift from the real part of G and for the growth rate drift from the imaginary part of G. In other words, shape changes proportional to the real part of the shape gradient have the maximum effect on the angular frequency and shape changes proportional to the imaginary part of the shape gradient have the maximum effect on the growth rate.

In the case of semi-simple two-fold degenerate eigenvalues, the shape gradient, G_{ij}, has four entries and the shape derivatives are the eigenvalues of the matrix $\int CG_{ij}\,\mathrm{d}S$, where C is the normal boundary perturbation. G_{11} gives the upper bound for ω_1 and G_{22} gives the upper

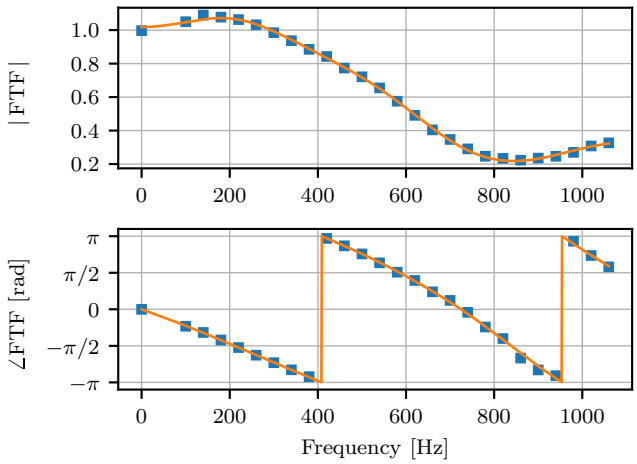

Fig. 6.2 Gain and phase of the flame transfer function ($|u'/\bar{u}| = 0.1$) as a function of the frequency. The squares are the values obtained from the experiments (Laera et al., 2017), and the solid line is the transfer function of the linear state-space model, evaluated at real values of ω.

bound for ω_2. For boundary perturbations proportional to G_{12} and G_{21}, either their real or imaginary parts, the diagonal elements of the matrix $\int CG_{ij}\,\mathrm{d}S$ are equal to zero. Therefore, its eigenvalues, i.e. the shape derivatives, take the form $\omega' = \pm(a + bi)$. The shape derivative is the same for the two eigenvalues, ω_1 and ω_2, but with opposite sign. In other words, at first order the eigenvalues split in opposite directions. The off-diagonal elements also have the property that:

$$\int G_{ij}\,\mathrm{d}S = 0 \quad \text{if } i \neq j \tag{6.1}$$

which means that the volume of the combustor does not change if we apply boundary perturbations proportional to the off-diagonal elements. Interestingly, this is conceptually similar to what was observed by Mensah et al. (2019a) for the same annular combustor. When the injectors are perturbed such that the FTF perturbations have the same phase and their average is zero, the eigenvalue perturbation for the two modes is the same but with opposite sign. Bauerheim et al. (2014) studied symmetry-breaking using burners of different type, specifically different interaction index and time delay. They derived an analytical formulation where the frequency and growth rate depend on two terms, a coupling and a splitting strength. Splitting eigenvalues results in one eigenvalue becoming less unstable and the other becoming more unstable. The eigenvalue drift is the same, except for the sign. The optimal burner pattern is such that the coupling strength is minimized and the splitting strength is zero. In this way, the symmetry is broken but the degeneracy is preserved.

In the simple case, the eigenvalues are shape differentiable, i.e. the derivative $\mathrm{d}\omega(\Omega)$ exists for all directions $\boldsymbol{V}$ and the mapping $\boldsymbol{V} \mapsto \mathrm{d}\omega(\Omega)$ is linear and continuous. In the

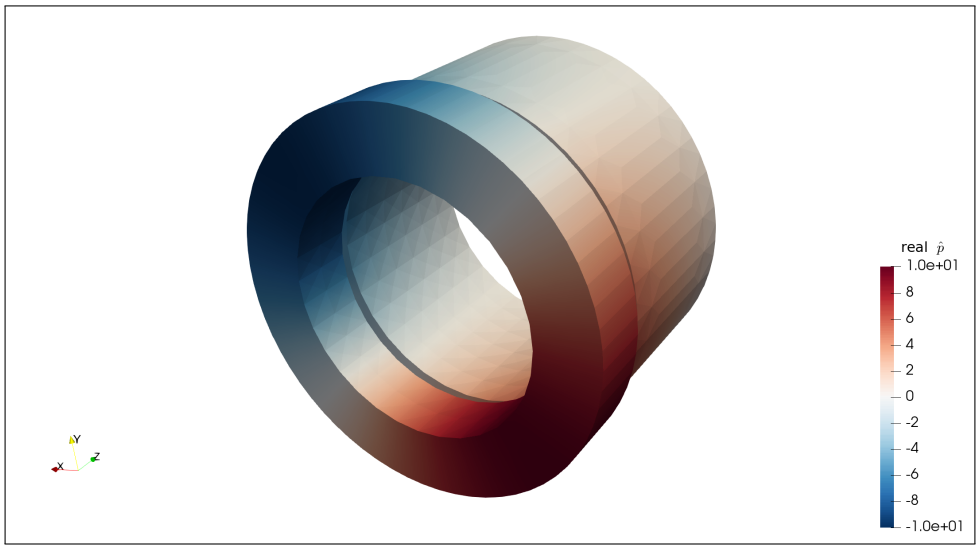

Fig. 6.3 Real part of the eigenvector, $\hat{p}$, of the first azimuthal mode of the MICCA combustor. It is a weakly coupled plenum mode. The associate eigenvalue is $\omega = 3181 + 504i$ rad s^{-1}.

semi-simple degenerate case, the eigenvalues are not shape differentiable because the mapping $\boldsymbol{V} \mapsto \mathrm{d}\omega(\Omega)$ is nonlinear due to the possible eigenvalue splitting. This can be an obstacle in optimization problems because the gradients are in general discontinuous and the cost functional is non-convex. Strictly speaking, however, this is not an optimization problem, in the sense that we are not trying to find the minimum of a cost functional. We are instead trying to reduce the eigenvalue growth rate using the information provided by the gradient and avoiding eigenvalue splitting.

6.3 Results - Shape sensitivity analysis

In this chapter we consider changes that do not break the discrete rotational symmetry of the annular combustor. In particular, we consider changes to the length and to the radii of plenum and combustion chamber and changes to the diameter of the burners and to the total flow passage area of the injectors.

We partition the boundary into boundary patches, $\partial\Omega_i$: rear, front, inner and outer plenum, etc. For each boundary patch, we use Eq. (6.2) to compute the shape derivatives for a unitary boundary displacement

$$C = \begin{cases} 1 & \text{on } \partial\Omega_i \\ 0 & \text{elsewhere} \end{cases} \tag{6.2}$$

Then we divide the shape derivatives by the surface area of the patch. In this way we obtain a local average of the derivatives that does not depend on the area of the patch. When applying symmetry-preserving changes, the two repeated eigenvalues do not split and the two shape derivatives have the same value. We point out, however, that more elaborate shape changes could be considered with the same approach, the only challenge being the parametrization of the shape.

Figure 6.4 shows the real and the imaginary part of the shape derivatives for the plenum and the combustion chamber as virtual boundary displacements proportional to the shape derivatives. The real part represents changes that reduce the angular frequency and the imaginary part represents changes that reduce the growth rate. We observe that changes to the shape of the combustion chamber have little or no effect on the angular frequency, which we expect since this is a plenum mode. We also observe that the sensitivity of the eigenvalue growth rate in the plenum is higher than in the combustion chamber. This can be explained by the fact that the gas is cooler, so the local wavelength is shorter and therefore geometry modifications of a given size have more influence. We can also compute shape derivatives for changes to the diameter of the burner and to the total flow passage area of the perforated plate. However, such changes would alter the flame transfer function. In this chapter we have used an experimentally-derived flame transfer function. We do not know how it would change due to these changes, so we do not consider them further. For an estimate of this in a different burner, the reader is referred to (Aguilar and Juniper, 2020).

6.4 Results - Shape changes

When we modify the shape, we fix the geometry of the burner and allow changes only in the plenum and in the combustion chamber. Our goal is to reduce the eigenvalue growth rate by following the steps below.

(i) We compute the shape derivatives for each boundary patch with C such that $\int_{\partial\Omega_i} C \, \mathrm{d}S = 1$, as explained in Section 6.3.

(ii) We take the imaginary part and normalize such that the maximum absolute value among all the shape derivatives is 1.

(iii) We subtract from the geometric parameters the imaginary part of the shape derivatives multiplied by the step size, which in this case is 0.0025 mm. This step size is arbitrary.

Here we present the results when the growth rate has reduced by 20%, which is after 4 iterations. Although the process can be continued, the salient points are most easily demonstrated before the geometry has changed significantly.

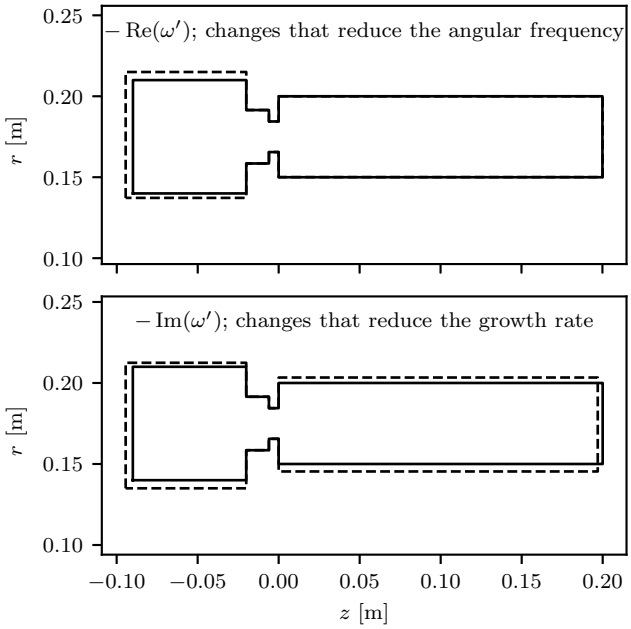

Fig. 6.4 Real (top) and imaginary (bottom) part of the eigenvalue shape derivatives for changes to the length and the radii of the plenum and the combustion chamber. The real part gives the influence on the angular frequency and the imaginary part the influence on the growth rate.

Fig. 6.5 (top) shows the initial and the final shape of a sector of the annular combustor. The size of the plenum has increased. The only boundary that has moved inwards is the combustion chamber outlet. Fig. 6.5 (bottom) shows the modulus of the corresponding pressure eigenvectors along the dotted line at $r = 0.175$ m, where the absolute value of the eigenvector is maximum.

The physical mechanism behind the growth rate's reduction can be explained by using the generalized Rayleigh criterion, Section 2.4. According to the Rayleigh criterion, a thermoacoustic system is unstable if the average of the product between the pressure, p', and the heat release rate perturbation, $\dot{q}'$, over the volume and over one period of oscillation is greater than the average of the losses due to acoustic radiation from the boundaries, Eq. (2.32). If we expand the Rayleigh index, $p'\dot{q}'$, we see that it depends on the modulus of the pressure in the flame volume, $|\hat{p}|$, and of the component of the velocity along the reference direction at the reference point, $|\hat{\boldsymbol{u}}(\boldsymbol{x}_r) \cdot \boldsymbol{n}_r|$, and on the phase angle difference between the heat release rate perturbation and the pressure perturbation as well as on the modulus of the flame transfer function. If we expand the acoustic energy flux, $p'\boldsymbol{u}'$, we see that this only depends on the modulus of the pressure at the boundary. On the other hand, Fig. 6.6 shows the phase difference between heat release rate and pressure perturbation for all sixteen burners. We see that, by changing the geometry, the algorithm increases the phase difference between the pressure, $\hat{p}$,

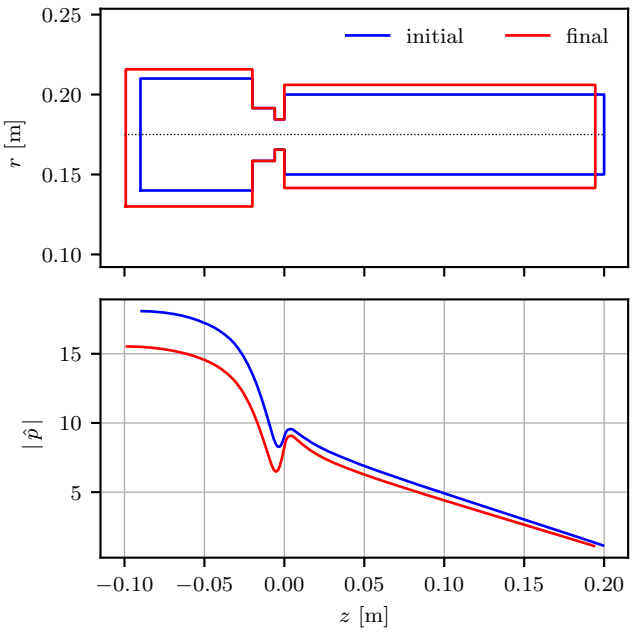

Fig. 6.5 (Top) Slice section view of one sector of the MICCA combustor before (blue) and after (red) applying pplying the shape changes to the plenum and the combustion chamber to reduce the growth rate. (Bottom) Absolute value of the eigenvector of the first azimuthal mode of the MICCA combustor, along the black dotted line in the top figure, before (blue) and after (red) the optimization. The sector is that in which the pressure is maximum. The associated eigenvalues are $\omega_\Omega = 3181 + 504.8i$ rad s^{-1} and $\omega_{\Omega_t} = 3050 + 401.3i$ rad s^{-1}

.

and the heat release rate, $\hat{q}$. This reduces the heat converted to work each cycle and therefore reduces the growth rate of the system, Eq. (2.36).

In this process the pressure within the flame volume and the velocity along the reference direction at the reference point do not change. They would change, however, if we were to allow the shape of the injector to change. The algorithm would try to decouple the plenum and the combustion chamber by expanding the diameter of the burner, d_b, and contracting the diameter of the perforated plate, d_{pp}. Consequently it would reduce the modulus of the velocity perturbation at the reference point and of the pressure perturbation within the flame volume.

This analysis shows how to significantly alter the growth rate of thermoacoustic oscillations by changing the geometry of a combustion chamber and plenum. In most practical devices, it would be possible to alter the geometry of the plenum without extensive re-design. It would be less feasible to alter the geometry of the combustion chamber, which is constrained by other considerations such as cooling and high altitude re-light. Nevertheless, as seen here and in (Aguilar and Juniper, 2020), the most influential component is the burner, due to its effect both on the flow rate through the burner and the heat release rate response of the flame. Any changes

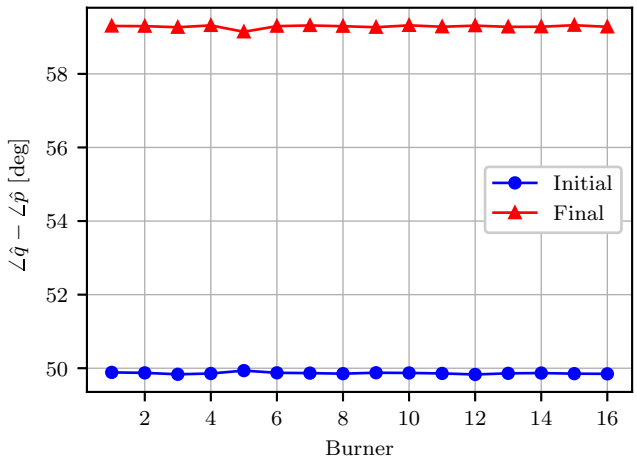

Fig. 6.6 Phase angle difference between the heat release rate, $\hat{q}$, and the pressure perturbation, $\hat{p}$, for all sixteen burners of the MICCA combustor before and after the optimization. This shows that the geometry changes have increased the phase difference between the flame and the pressure, thereby reducing the growth rate.

to the burner require, however, extensive re-design and re-certification. Although this would be worthwhile in the long term, it is likely that plenum modifications, as identified with the method in this chapter, would identify useful and easily-implemented changes to reduce or eliminate thermoacoustic oscillations in practical devices without affecting other aspects of their performance.

6.5 Conclusion

We have combined a thermoacoustic Helmholtz solver with adjoint-based shape optimization to reduce the growth rate of a linearly unstable thermaocustic mode in a symmetric annular combustor. The mode is azimuthal and therefore two-fold degenerate. We express the shape derivative of the eigenvalue in Hadamard form, i.e. for arbitrary shape changes. We preserve the symmetry by restricting the shape changes to modifications applied to lengths and radii. We use an experimentally-derived flame transfer function and, because we do not know how this would change with the burner geometry, we fix the burner geometry. After modifying the shape, we use the analysis to reveal the physical mechanism that causes the growth rate's reduction. The shape changes increase the phase difference between the pressure and the heat release rate fluctuations.

This study shows how to calculate the shape derivatives and iteratively modify the shape of a laboratory-scale annular combustor using a Helmholtz solver with adjoints. It explains the effect

on the eigenvalues of both symmetry-breaking and symmetry-preserving shape changes and how the eigenvalue growth rate can be reduced. The method can be applied to the plenum, the burner, and the combustion chamber. In practical devices, modifying the burner and combustion chamber may be impractical in the short term because of their influence on other factors, such as high altitude relight. Therefore modifying the plenum may be the most practical option and, as shown in this chapter, has a strong influence on the thermoacoustic growth rate.

The most influential, but hardest to change, component on thermoacoustic behaviour is the burner. If adjoint methods are to be used for combustor design, then these methods must include the influence of the burner shape on the flow behaviour, as in Tammisola and Juniper (2016), and hence on the flame. This is a significantly larger challenge and we leave it for future work. The methods in this chapter can now be applied to more complex geometries such as those on aircraft gas turbines, in which the plenum surrounds the combustion chamber and is connected to it by dilution holes. Although the conceptual challenge of this has been answered by this paper, the extra geometric complexity presents a significant technical challenge. A possible strategy to deal with the geometric complexity would be to use parametric shapes and consider a displacement field of the form $\boldsymbol{V}(z)$ (independent of the azimuthal coordinate).

Chapter 7

Conclusions and Future work

This thesis is on the shape sensitivity analysis of thermoacoustic oscillations in laboratory-scale combustors, both axial and annular. The physics is modelled with an inhomogeneous Helmholtz equation for the flame-acoustics interaction, assuming a zero Mach number base flow, and acoustic impedance boundary conditions. The differential problem is discretized using the finite element method. The sensitivity of the thermoacoustic oscillations to the domain shape is determined using shape calculus. We derive formulae for the shape derivatives of both simple and semi-simple degenerate eigenvalues for different boundary conditions (Dirichlet, Neumann and Robin). These formulae have the structure of a projection of the shape gradient onto the direction of the boundary perturbation. The shape gradient, which does not depend on the direction, is a function of the direct and adjoint eigenfunctions. We compute the shape gradient for the unperturbed problem, and then the shape derivative for a boundary displacement. We study three cases: an electrically heated Rijke tube, a turbulent swirl combustor and an annular combustor (MICCA).

The first two systems are longitudinally unstable. We model the two systems as two-dimensional planar and parametrize the shapes using B-spline curves. We compute the eigenvalue shape derivatives for each control point, i.e. we project the shape gradient onto the direction given by the displacement field associated with each control point. We stabilize both systems by making small geometry changes proportional to the eigenvalue growth rate's shape derivatives. These small changes have the effect of increasing the phase angle difference between the pressure and the heat release rate oscillations.

The third case is the MICCA annular combustor, which is azimuthally unstable. The azimuthal mode is two-fold degenerate due to the discrete rotational symmetry. We study the sensitivity to both symmetry-breaking and symmetry-preserving shape changes. The first are proportional to the shape gradient and the second consists in changes to lengths and radii. Compared to symmetry-breaking, when applying symmetry-preserving boundary perturbations

(the perturbations are normalized such that they sweep the same volume) the eigenvalues do not split, and the growth rate of the most unstable eigenvalue is smaller. We restrict the geometry modifications to changes to the length and the radii of the plenum and the combustion chamber. We reduce the growth rate of the unstable mode. As in the case of the axial combustors, the growth rate's reduction is achieved by increasing the phase angle difference between pressure and heat release rate fluctuations in the reaction zone.

In practical devices, modifying the burners or the combustion chamber would be impractical because of their influence on other factors, such as high altitude relight. Therefore, modifying the plenum may be the most practical option and, as shown in this thesis, has a strong influence on the growth rate of the thermoacoustic oscillations. Throughout this thesis we assume that the flame transfer function is not affected by geometry modifications, which is reasonable only for plenum modifications. If adjoint methods are to be used for combustor design, then these methods must include the influence of the burner on the flow behaviour, as in (Tammisola and Juniper, 2016), and hence on the flame. This is a significantly bigger challenge, and we leave it for future work.

The methods developed in this thesis can now be applied to more complex geometries such as those in aircraft gas turbines, in which the plenum surrounds the combustions chamber and is connected to it through dilution holes. Although the conceptual challenge is addressed in this thesis, the extra geometric complexity presents a significant technical challenge. A strategy to deal with the geometric complexity would be to use parametric shapes, e.g. NURBS surfaces, and consider boundary perturbations independent of the azimuthal coordinate.

References

Aguilar, J. G. and Juniper, M. P. (2018). Adjoint Methods for Elimination of Thermoacoustic Oscillations in a Model Annular Combustor via Small Geometry Modifications. In *Volume 4A: Combustion, Fuels, and Emissions*, page V04AT04A054, Oslo, Norway. American Society of Mechanical Engineers. 6, 8

Aguilar, J. G. and Juniper, M. P. (2020). Thermoacoustic stabilization of a longitudinal combustor using adjoint methods. *Physical Review Fluids*, 5(8):083902. 6, 8, 65, 67

Aguilar, J. G., Magri, L., and Juniper, M. P. (2017). Adjoint-based sensitivity analysis of low-order thermoacoustic networks using a wave-based approach. *Journal of Computational Physics*, 341:163–181. 6

Alnæs, M., Blechta, J., Hake, J., Johansson, A., Kehlet, B., Logg, A., Richardson, C., Ring, J., Rognes, M. E., and Wells, G. N. (2015). The FEniCS Project Version 1.5. *Archive of Numerical Software*, 3(100). 33

Arnoldi, W. E. (1951). The principle of minimized iterations in the solution of the matrix eigenvalue problem. *Quarterly of Applied Mathematics*, 9(1):17–29. 33

Avdonin, A., Jaensch, S., Silva, C. F., Češnovar, M., and Polifke, W. (2018). Uncertainty quantification and sensitivity analysis of thermoacoustic stability with non-intrusive polynomial chaos expansion. *Combustion and Flame*, 189:300–310. 54

Balasubramanian, K. and Sujith, R. I. (2008). Thermoacoustic instability in a Rijke tube: Non-normality and nonlinearity. *Physics of Fluids*, 20(4):044103. 3

Bauerheim, M., Cazalens, M., and Poinsot, T. (2015). A theoretical study of mean azimuthal flow and asymmetry effects on thermo-acoustic modes in annular combustors. *Proceedings of the Combustion Institute*, 35(3):3219–3227. 3

Bauerheim, M., Ndiaye, A., Constantine, P., Moreau, S., and Nicoud, F. (2016). Symmetry breaking of azimuthal thermoacoustic modes: the UQ perspective. *Journal of Fluid Mechanics*, 789:534–566. 3

Bauerheim, M., Salas, P., Nicoud, F., and Poinsot, T. (2014). Symmetry breaking of azimuthal thermo-acoustic modes in annular cavities: a theoretical study. *Journal of Fluid Mechanics*, 760:431–465. 2, 63

Bellucci, V., Schuermans, B., Nowak, D., Flohr, P., and Paschereit, C. O. (2005). Thermoacoustic Modeling of a Gas Turbine Combustor Equipped With Acoustic Dampers. *Journal of Turbomachinery*, 127(2):372–379. 3

Bothien, M. R., Moeck, J. P., Lacarelle, A., and Paschereit, C. O. (2007). Time domain modelling and stability analysis of complex thermoacoustic systems. *Proceedings of the Institution of Mechanical Engineers, Part A: Journal of Power and Energy*, 221(5):657–668. 2, 17

Bottaro, A., Corbett, P., and Luchini, P. (2003). The effect of base flow variation on flow stability. *Journal of Fluid Mechanics*, 476:293–302. 5

Boujo, E., Fani, A., and Gallaire, F. (2019). Second-order sensitivity in the cylinder wake: Optimal spanwise-periodic wall actuation and wall deformation. *Physical Review Fluids*, 4(5):053901. 8

Bourgouin, J., Durox, D., Moeck, J., Schuller, T., and Candel, S. (2015a). A new pattern of instability observed in an annular combustor: The slanted mode. *Proceedings of the Combustion Institute*, 35(3):3237–3244. 59, 60

Bourgouin, J.-F., Durox, D., Moeck, J. P., Schuller, T., and Candel, S. (2015b). Characterization and Modeling of a Spinning Thermoacoustic Instability in an Annular Combustor Equipped With Multiple Matrix Injectors. *Journal of Engineering for Gas Turbines and Power*, 137(2):021503. 60

Brewster, J. and Juniper, M. P. (2020). Shape sensitivity of eigenvalues in hydrodynamic stability, with physical interpretation for the flow around a cylinder. *European Journal of Mechanics - B/Fluids*, 80:80–91. 8

Camarri, S. (2015). Flow control design inspired by linear stability analysis. *Acta Mechanica*, 226(4):979–1010. 6

Camporeale, S. M., Fortunato, B., and Campa, G. (2011). A Finite Element Method for Three-Dimensional Analysis of Thermo-acoustic Combustion Instability. *Journal of Engineering for Gas Turbines and Power*, 133(1):011506. 3

Candel, S., Durox, D., Schuller, T., Bourgouin, J.-F., and Moeck, J. P. (2014). Dynamics of Swirling Flames. *Annual Review of Fluid Mechanics*, 46(1):147–173. 14

Crocco, L. and Cheng, S.-I. (1956). *Theory of Combustion Instability in Liquid Propellant Rocket Motors*. Buttherworths Scientific Publications. 16

Culick, F. E. C. (1988). Combustion Instabilities in Liquid-Fueled Propulsion Systems - An Overview. 3

Culick, F. E. C. (2006). *Unsteady Motions in Combustion Chambers for Propulsion Systems*. Number AG-AVT-039 in RTO AGARDograph. The Research and Technology Organisation (RTO) of NATO. 1, 3

Culick, F. E. C. and Yang, V. (1995). Instability Phenomenology and Case Studies: Overview of Combustion Instabilities in Liquid-Propellant Rocket Engines. In *Liquid Rocket Engine Combustion Instability*, Progress in Astronautics and Aeronautics, pages 3–37. American Institute of Aeronautics and Astronautics. 3

Cuquel, A., Durox, D., and Schuller, T. (2013). Impact of flame base dynamics on the non-linear frequency response of conical flames. *Comptes Rendus Mécanique*, 341(1):171–180. 14

Delfour, M. C. and Zolésio, J. P. (2011). *Shapes and Geometries: Metrics, Analysis, Differential Calculus, and Optimization, Second Edition*. Society for Industrial and Applied Mathematics. 36

Dowling, A. P. (1997). Nonlinear self-excited oscillations of a ducted flame. *Journal of Fluid Mechanics*, 346:271–290. 14

Dowling, A. P. and Stow, S. R. (2003). Acoustic Analysis of Gas Turbine Combustors. *Journal of Propulsion and Power*, 19(5):751–764. 2

Durox, D., Bourgouin, J. F., Moeck, J. P., Philip, M., Schuller, T., and Candel, S. (2013). Nonlinear interactions in combustion instabilities coupled by azimuthal acoustic modes. In *n3l - Int'l Summer School and Workshop on Non-Normal and Nonlinear Effects in Aero- and Thermoacoustics*, Munich. 60

Emmert, T., Meindl, M., Jaensch, S., and Polifke, W. (2016). Linear State Space Interconnect Modeling of Acoustic Systems. *Acta Acustica united with Acustica*, 102(5):824–833. 2

Evesque, S. and Polifke, W. (2002). Low-Order Acoustic Modelling for Annular Combustors: Validation and Inclusion of Modal Coupling. In *Volume 1: Turbo Expo 2002*, pages 321–331, Amsterdam, The Netherlands. American Society of Mechanical Engineers. 2

Falco, S. and Juniper, M. P. (2021a). Shape Optimization of Thermoacoustic Systems Using a Two-Dimensional Adjoint Helmholtz Solver. *Journal of Engineering for Gas Turbines and Power*, 143(7). 7, 49

Falco, S. and Juniper, M. P. (2021b). Shape Sensitivity of Thermoacoustics Oscillations in an Annular Combustor With an Adjoint Helmholtz Solver. *Journal of Engineering for Gas Turbines and Power*. Submitted. 59

Geuzaine, C. and Remacle, J.-F. (2009). Gmsh: A 3-D finite element mesh generator with built-in pre- and post-processing facilities. *International Journal for Numerical Methods in Engineering*, 79(11):1309–1331. 34

Ghirardo, G., Juniper, M. P., and Moeck, J. P. (2016). Weakly nonlinear analysis of thermoacoustic instabilities in annular combustors. *Journal of Fluid Mechanics*, 805:52–87. 3

Giannetti, F., Camarri, S., and Luchini, P. (2010). Structural sensitivity of the secondary instability in the wake of a circular cylinder. *Journal of Fluid Mechanics*, 651:319–337. 5

Giannetti, F. and Luchini, P. (2006). Leading-edge receptivity by adjoint methods. *Journal of Fluid Mechanics*, 547:21–53. 5

Giannetti, F. and Luchini, P. (2007). Structural sensitivity of the first instability of the cylinder wake. *Journal of Fluid Mechanics*, 581:167–197. 5

Giauque, A., Selle, L., Gicquel, L., Poinsot, T., Buechner, H., Kaufmann, P., and Krebs, W. (2005). System identification of a large-scale swirled partially premixed combustor using LES and measurements. *Journal of Turbulence*, 6:N21. 4

Gicquel, L. Y. M., Staffelbach, G., and Poinsot, T. (2012). Large Eddy Simulations of gaseous flames in gas turbine combustion chambers. *Progress in Energy and Combustion Science*, 38(6):782–817. 4

Giusti, A., Andreini, A., Facchini, B., Vitale, I., and Turrini, F. (2013). Thermoacoustic Analysis of a Full Annular Aero-engine Lean Combustor with Multi-perforated Liners. In *19th AIAA/CEAS Aeroacoustics Conference*, Berlin, Germany. American Institute of Aeronautics and Astronautics. 4

Grinfeld, P. (2010). Hadamard's Formula Inside and Out. *Journal of Optimization Theory and Applications*, 146(3):654–690. 42

Gullaud, E. and Nicoud, F. (2012). Effect of Perforated Plates on the Acoustics of Annular Combustors. *AIAA Journal*, 50(12):2629–2642. 4

Gustavsen, B. (2006). Improving the Pole Relocating Properties of Vector Fitting. *IEEE Transactions on Power Delivery*, 21(3):1587–1592. 17, 60

Gustavsen, B. and Semlyen, A. (1999). Rational approximation of frequency domain responses by vector fitting. *IEEE Transactions on Power Delivery*, 14(3):1052–1061. 17, 60

Güttel, S. and Tisseur, F. (2017). The nonlinear eigenvalue problem. *Acta Numerica*, 26:1–94. 29

Han, X., Li, J., and Morgans, A. S. (2015). Prediction of combustion instability limit cycle oscillations by combining flame describing function simulations with a thermoacoustic network model. *Combustion and Flame*, 162(10):3632–3647. 3

Hernandez, V., Roman, J. E., and Vidal, V. (2005). SLEPc: A scalable and flexible toolkit for the solution of eigenvalue problems. *ACM Transactions on Mathematical Software*, 31(3):351–362. 33

Heuveline, V. and Strauß, F. (2009). Shape optimization towards stability in constrained hydrodynamic systems. *Journal of Computational Physics*, 228(4):938–951. 7

Hill, D. (1992). A theoretical approach for analyzing the restabilization of wakes. American Institute of Aeronautics and Astronautics. 5

Hill, D. C. (1995). Adjoint systems and their role in the receptivity problem for boundary layers. *Journal of Fluid Mechanics*, 292:183–204. 5

Huerre, P. and Monkewitz, P. A. (1990). Local and Global Instabilities in Spatially Developing Flows. *Annual Review of Fluid Mechanics*, 22(1):473–537. 5

Jameson, A. (2003). Aerodynamic Shape Optimization Using the Adjoint Method. *Lectures at the Von Karman Institute, Brussels*. 1

Jamieson, N. P., Rigas, G., and Juniper, M. P. (2017). Experimental sensitivity analysis via a secondary heat source in an oscillating thermoacoustic system. *International Journal of Spray and Combustion Dynamics*, 9(4):230–240. 6

Juniper, M. P. (2011). Triggering in the horizontal Rijke tube: non-normality, transient growth and bypass transition. *Journal of Fluid Mechanics*, 667:272–308. 3

Juniper, M. P. (2018). Sensitivity analysis of thermoacoustic instability with adjoint Helmholtz solvers. *Physical Review Fluids*, 3(11):110509. 7, 15, 19, 21, 49, 51

Juniper, M. P. and Sujith, R. (2018). Sensitivity and Nonlinearity of Thermoacoustic Oscillations. *Annual Review of Fluid Mechanics*, 50(1):661–689. 1, 21

Kato, T. (1995). *Perturbation Theory for Linear Operators*. Classics in Mathematics. Springer-Verlag, Berlin Heidelberg. 83

Kirillov, O. N. (2021). *Nonconservative Stability Problems of Modern Physics*. Number 14 in De gruyter studies in mathematical physics. De Gruyter, Boston. 83

Kiriyama, Y., Katamine, E., and Azegami, H. (2018). Shape optimisation problem for stability of Navier–Stokes flow field. *International Journal of Computational Fluid Dynamics*, 32(2-3):68–87. 8

Krebs, W., Flohr, P., Prade, B., and Hoffmann, S. (2002). Thermoacoustic Stability Chart for High-Intensity Gas Turbine Combustion Systems. *Combustion Science and Technology*, 174(7):99–128. 59

Kungurtsev, P. V. and Juniper, M. P. (2019). Adjoint-based shape optimization of the microchannels in an inkjet printhead. *Journal of Fluid Mechanics*, 871:113–138. 8

Laera, D., Schuller, T., Prieur, K., Durox, D., Camporeale, S. M., and Candel, S. (2017). Flame Describing Function analysis of spinning and standing modes in an annular combustor and comparison with experiments. *Combustion and Flame*, 184:136–152. xvi, 4, 60, 63

Larson, M. G. and Bengzon, F. (2013). *The Finite Element Method: Theory, Implementation, and Applications*, volume 10 of *Texts in Computational Science and Engineering*. Springer, Berlin, Heidelberg. 25

Laurent, C., Bauerheim, M., Poinsot, T., and Nicoud, F. (2019). A novel modal expansion method for low-order modeling of thermoacoustic instabilities in complex geometries. *Combustion and Flame*, 206:334–348. 3

Levine, H. and Schwinger, J. (1948). On the Radiation of Sound from an Unflanged Circular Pipe. *Physical Review*, 73(4):383–406. 17

Lieuwen, T. C. and Yang, V. (2005). *Combustion Instabilities In Gas Turbine Engines: Operational Experience, Fundamental Mechanisms, and Modeling*. American Institute of Aeronautics and Astronautics, Reston ,VA. 1

Logg, A., Mardal, K.-A., and Wells, G., editors (2012). *Automated Solution of Differential Equations by the Finite Element Method: The FEniCS Book*. Lecture Notes in Computational Science and Engineering. Springer-Verlag, Berlin Heidelberg. 33

Luchini, P. and Bottaro, A. (1998). Görtler vortices: a backward-in-time approach to the receptivity problem. *Journal of Fluid Mechanics*, 363:1–23. 5

Luchini, P. and Bottaro, A. (2014). Adjoint Equations in Stability Analysis. *Annual Review of Fluid Mechanics*, 46(1):493–517. 1, 6, 21

Magina, N., Shin, D.-H., Acharya, V., and Lieuwen, T. (2013). Response of non-premixed flames to bulk flow perturbations. *Proceedings of the Combustion Institute*, 34(1):963–971. 14

Magina, N. A. and Lieuwen, T. C. (2016). Effect of axial diffusion on the response of diffusion flames to axial flow perturbations. *Combustion and Flame*, 167:395–408. 14

Magri, L. (2019). Adjoint Methods as Design Tools in Thermoacoustics. *Applied Mechanics Reviews*, 71(2):020801. 7, 21

Magri, L., Bauerheim, M., and Juniper, M. P. (2016a). Stability analysis of thermo-acoustic nonlinear eigenproblems in annular combustors. Part I. Sensitivity. *Journal of Computational Physics*, 325:395–410. 7

Magri, L., Bauerheim, M., Nicoud, F., and Juniper, M. P. (2016b). Stability analysis of thermo-acoustic nonlinear eigenproblems in annular combustors. Part II. Uncertainty quantification. *Journal of Computational Physics*, 325:411–421. 7

Magri, L. and Juniper, M. (2014). Global modes, receptivity, and sensitivity analysis of diffusion flames coupled with duct acoustics. *Journal of Fluid Mechanics*, 752:237–265. 6

Magri, L. and Juniper, M. P. (2013). Sensitivity analysis of a time-delayed thermo-acoustic system via an adjoint-based approach. *Journal of Fluid Mechanics*, 719:183–202. 6, 49

Marquet, O., Sipp, D., and Jacquin, L. (2008). Sensitivity analysis and passive control of cylinder flow. *Journal of Fluid Mechanics*, 615:221–252. 5

Martin, C. E., Benoit, L., Sommerer, Y., Nicoud, F., and Poinsot, T. (2006). Large-Eddy Simulation and Acoustic Analysis of a Swirled Staged Turbulent Combustor. *AIAA Journal*, 44(4):741–750. 4

Martinez-Cava, A., Chávez-Modena, M., Valero, E., de Vicente, J., and Ferrer, E. (2020). Sensitivity gradients of surface geometry modifications based on stability analysis of compressible flows. *Physical Review Fluids*, 5(6):063902. 8

Mehrmann, V. and Voss, H. (2004). Nonlinear eigenvalue problems: a challenge for modern eigenvalue methods: Nonlinear eigenvalue problems: a challenge for modern eigenvalue methods. *GAMM-Mitteilungen*, 27(2):121–152. 29

Mejia, D., Miguel-Brebion, M., Ghani, A., Kaiser, T., Duchaine, F., Selle, L., and Poinsot, T. (2018). Influence of flame-holder temperature on the acoustic flame transfer functions of a laminar flame. *Combustion and Flame*, 188:5–12. 14

Meliga, P., Sipp, D., and Chomaz, J.-M. (2010a). Effect of compressibility on the global stability of axisymmetric wake flows. *Journal of Fluid Mechanics*, 660:499–526. 6

Meliga, P., Sipp, D., and Chomaz, J.-M. (2010b). Open-loop control of compressible afterbody flows using adjoint methods. *Physics of Fluids*, 22(5):054109. 6

Mensah, G. A. (2019). *Efficient Computation of Thermoacoustic Modes*. PhD thesis, Technische Universität Berlin, Berlin, Germany. 8, 21, 31

Mensah, G. A., Campa, G., and Moeck, J. P. (2016). Efficient Computation of Thermoacoustic Modes in Industrial Annular Combustion Chambers Based on Bloch-Wave Theory. *Journal of Engineering for Gas Turbines and Power*, 138(8):081502. 4

Mensah, G. A., Magri, L., and Moeck, J. P. (2018a). Methods for the Calculation of Thermoacoustic Stability Boundaries and Monte Carlo-Free Uncertainty Quantification. *Journal of Engineering for Gas Turbines and Power*, 140(6):061501. 7, 54, 83

Mensah, G. A., Magri, L., Orchini, A., and Moeck, J. P. (2019a). Effects of Asymmetry on Thermoacoustic Modes in Annular Combustors: A Higher-Order Perturbation Study. *Journal of Engineering for Gas Turbines and Power*, 141(4):041030. 7, 16, 63

Mensah, G. A., Magri, L., Silva, C. F., Buschmann, P. E., and Moeck, J. P. (2018b). Exceptional points in the thermoacoustic spectrum. *Journal of Sound and Vibration*, 433:124–128. 7

Mensah, G. A. and Moeck, J. P. (2017). Acoustic Damper Placement and Tuning for Annular Combustors: An Adjoint-Based Optimization Study. *Journal of Engineering for Gas Turbines and Power*, 139(6):061501. 7

Mensah, G. A., Orchini, A., and Moeck, J. P. (2019b). Adjoint-based computation of shape sensitivity in a Rijke-tube. In *Proceedings of the 23rd International Congress on Acoustics*, Aachen, Germany. 7

Mensah, G. A., Orchini, A., and Moeck, J. P. (2020). Perturbation theory of nonlinear, non-self-adjoint eigenvalue problems: Simple eigenvalues. *Journal of Sound and Vibration*, 473:115200. 83

Merk, M., Gaudron, R., Silva, C., Gatti, M., Mirat, C., Schuller, T., and Polifke, W. (2019). Prediction of combustion noise of an enclosed flame by simultaneous identification of noise source and flame dynamics. *Proceedings of the Combustion Institute*, 37(4):5263–5270. 14

Mongia, H. C., Held, T. J., Hsiao, G. C., and Pandalai, R. P. (2003). Challenges and Progress in Controlling Dynamics in Gas Turbine Combustors. *Journal of Propulsion and Power*, 19(5):822–829. 1

Motheau, E., Nicoud, F., and Poinsot, T. (2014a). Mixed acoustic–entropy combustion instabilities in gas turbines. *Journal of Fluid Mechanics*, 749:542–576. 4

Motheau, E., Selle, L., and Nicoud, F. (2014b). Accounting for convective effects in zero-Mach-number thermoacoustic models. *Journal of Sound and Vibration*, 333(1):246–262. 4

Nakazawa, T. and Azegami, H. (2016). Shape optimization of flow field improving hydrodynamic stability. *Japan Journal of Industrial and Applied Mathematics*, 33(1):167–181. 8

Ni, F., Nicoud, F., Méry, Y., and Staffelbach, G. (2018). Including Flow–Acoustic Interactions in the Helmholtz Computations of Industrial Combustors. *AIAA Journal*, 56(12):4815–4829. 4

Nicoud, F., Benoit, L., Sensiau, C., and Poinsot, T. (2007). Acoustic Modes in Combustors with Complex Impedances and Multidimensional Active Flames. *AIAA Journal*, 45(2):426–441. 3, 12, 14, 51

Nicoud, F. and Poinsot, T. (2005). Thermoacoustic instabilities: Should the Rayleigh criterion be extended to include entropy changes? *Combustion and Flame*, 142(1-2):153–159. 18

Nicoud, F. and Wieczorek, K. (2009). About the Zero Mach Number Assumption in the Calculation of Thermoacoustic Instabilities. *International Journal of Spray and Combustion Dynamics*, 1(1):67–111. 13

Noiray, N., Bothien, M., and Schuermans, B. (2011). Investigation of azimuthal staging concepts in annular gas turbines. *Combustion Theory and Modelling*, 15(5):585–606. 3

Noiray, N., Durox, D., Schuller, T., and Candel, S. (2008). A unified framework for nonlinear combustion instability analysis based on the flame describing function. *Journal of Fluid Mechanics*, 615:139–167. 14

Orchini, A. and Juniper, M. P. (2016). Linear stability and adjoint sensitivity analysis of thermoacoustic networks with premixed flames. *Combustion and Flame*, 165:97–108. 6

Orchini, A., Magri, L., Silva, C. F., Mensah, G. A., and Moeck, J. P. (2020a). Degenerate perturbation theory in thermoacoustics: high-order sensitivities and exceptional points. *Journal of Fluid Mechanics*, 903. 7

Orchini, A., Mensah, G. A., and Moeck, J. P. (2021). Perturbation theory of nonlinear, non-self-adjoint eigenvalue problems: Semisimple eigenvalues. *Journal of Sound and Vibration*, 507:116150. 83

Orchini, A., Silva, C. F., Mensah, G. A., and Moeck, J. P. (2020b). Thermoacoustic modes of intrinsic and acoustic origin and their interplay with exceptional points. *Combustion and Flame*, 211:83–95. 7

Palies, P., Durox, D., Schuller, T., and Candel, S. (2010). The combined dynamics of swirler and turbulent premixed swirling flames. *Combustion and Flame*, 157(9):1698–1717. 53

Palies, P., Durox, D., Schuller, T., and Candel, S. (2011a). Nonlinear combustion instability analysis based on the flame describing function applied to turbulent premixed swirling flames. *Combustion and Flame*, 158(10):1980–1991. 54

Palies, P., Schuller, T., Durox, D., and Candel, S. (2011b). Modeling of premixed swirling flames transfer functions. *Proceedings of the Combustion Institute*, 33(2):2967–2974. 14

Piegl, L. and Tiller, W. (1995). *The NURBS Book*. Monographs in Visual Communications. Springer, Berlin, Heidelberg. 85

Poinsot, T. (2017). Prediction and control of combustion instabilities in real engines. *Proceedings of the Combustion Institute*, 36(1):1–28. 1, 4

Poinsot, T. and Veynante, D. (2012). *Theoretical and Numerical Combustion*. CNRS, Toulouse, 3rd edition. 18

Pralits, J., Airiau, C., Hanifi, A., and Henningson, D. (2000). Sensitivity Analysis Using Adjoint Parabolized Stability Equations for Compressible Flows. *Flow, Turbulence and Combustion*, 65(3):321–346. 5

Qadri, U. A. (2014). *Global stability and control of swirling jets and flames*. PhD thesis, University of Cambridge, Cambridge, United Kingdom. 6

Qadri, U. A., Chandler, G. J., and Juniper, M. P. (2015). Self-sustained hydrodynamic oscillations in lifted jet diffusion flames: origin and control. *Journal of Fluid Mechanics*, 775:201–222. 6

Qadri, U. A., Chandler, G. J., and Juniper, M. P. (2018). Passive control of global instability in low-density jets. *European Journal of Mechanics - B/Fluids*, 72:311–319. 6

Qadri, U. A., Mistry, D., and Juniper, M. P. (2013). Structural sensitivity of spiral vortex breakdown. *Journal of Fluid Mechanics*, 720:558–581. 6

Rayleigh (1878). The Explanation of Certain Acoustic Phenomena. *Nature*, 18(455):319–321. 1

Rienstra, S. W. and Hirschberg, A. (2004). *An Introduction to Acoustics*. Eindhoven University of Technology. 17

Rigas, G., Jamieson, N. P., Li, L. K. B., and Juniper, M. P. (2016). Experimental sensitivity analysis and control of thermoacoustic systems. *Journal of Fluid Mechanics*, 787:R1. 6, 49

Rijke, P. L. (1859). LXXI. Notice of a new method of causing a vibration of the air contained in a tube open at both ends. *The London, Edinburgh, and Dublin Philosophical Magazine and Journal of Science*, 17(116):419–422. 49

Schmidt, S. (2010). *Efficient Large Scale Aerodynamic Design Based on Shape Calculus*. PhD thesis, Universität Trier, Trier, Germany. 35

Schmidt, S. and Schulz, V. (2010). Shape derivatives for general objective functions and the incompressible Navier–Stokes equations. *Control and Cybernetics*, 39(3):677–713. 35, 38

Schuermans, B., Bellucci, V., and Paschereit, C. O. (2003). Thermoacoustic Modeling and Control of Multi Burner Combustion Systems. In *Volume 2: Turbo Expo 2003*, pages 509–519, Atlanta, Georgia, USA. American Society of Mechanical Engineers. 2, 3

Schuller, T., Durox, D., and Candel, S. (2003). A unified model for the prediction of laminar flame transfer functions: comparisons between conical and V-flame dynamics. *Combustion and Flame*, 134(1):21–34. 14

Silva, C. F., Magri, L., Runte, T., and Polifke, W. (2017). Uncertainty Quantification of Growth Rates of Thermoacoustic Instability by an Adjoint Helmholtz Solver. *Journal of Engineering for Gas Turbines and Power*, 139(1):011901. 7, 54

Silva, C. F., Nicoud, F., Schuller, T., Durox, D., and Candel, S. (2013). Combining a Helmholtz solver with the flame describing function to assess combustion instability in a premixed swirled combustor. *Combustion and Flame*, 160(9):1743–1754. 4, 53

Sipp, D., Marquet, O., Meliga, P., and Barbagallo, A. (2010). Dynamics and Control of Global Instabilities in Open-Flows: A Linearized Approach. *Applied Mechanics Reviews*, 63(3). 6

Sokolowski, J. and Zolesio, J.-P. (1992). *Introduction to Shape Optimization*, volume 16 of *Springer Series in Computational Mathematics*. Springer, Berlin, Heidelberg. 36

Sonntag, M., Schmidt, S., and Gauger, N. R. (2016). Shape derivatives for the compressible Navier–Stokes equations in variational form. *Journal of Computational and Applied Mathematics*, 296:334–351. 38

Staffelbach, G., Gicquel, L. Y. M., Boudier, G., and Poinsot, T. (2009). Large Eddy Simulation of self excited azimuthal modes in annular combustors. *Proceedings of the Combustion Institute*, 32(2):2909–2916. 4, 59

Stow, S. R. and Dowling, A. P. (2001). Thermoacoustic Oscillations in an Annular Combustor. In *Volume 2: Coal, Biomass and Alternative Fuels; Combustion and Fuels; Oil and Gas Applications; Cycle Innovations*, page V002T02A004, New Orleans, Louisiana, USA. American Society of Mechanical Engineers. 2

Strykowski, P. J. and Sreenivasan, K. R. (1990). On the formation and suppression of vortex 'shedding' at low Reynolds numbers. *Journal of Fluid Mechanics*, 218:71–107. 5

Tammisola, O., Giannetti, F., Citro, V., and Juniper, M. P. (2014). Second-order perturbation of global modes and implications for spanwise wavy actuation. *Journal of Fluid Mechanics*, 755:314–335. 5

Tammisola, O. and Juniper, M. P. (2016). Coherent structures in a swirl injector at Re = 4800 by nonlinear simulations and linear global modes. *Journal of Fluid Mechanics*, 792:620–657. 69, 72

Wolf, P., Staffelbach, G., Gicquel, L. Y. M., Müller, J.-D., and Poinsot, T. (2012). Acoustic and Large Eddy Simulation studies of azimuthal modes in annular combustion chambers. *Combustion and Flame*, 159(11):3398–3413. 4, 59

Worth, N. A. and Dawson, J. R. (2013a). Modal dynamics of self-excited azimuthal instabilities in an annular combustion chamber. *Combustion and Flame*, 160(11):2476–2489. 59

Worth, N. A. and Dawson, J. R. (2013b). Self-excited circumferential instabilities in a model annular gas turbine combustor: Global flame dynamics. *Proceedings of the Combustion Institute*, 34(2):3127–3134. 59

Xia, Y., Laera, D., Jones, W. P., and Morgans, A. S. (2019). Numerical prediction of the Flame Describing Function and thermoacoustic limit cycle for a pressurised gas turbine combustor. *Combustion Science and Technology*, 191(5-6):979–1002. 3

Zinn, B. T. and Lores, M. E. (1971). Application of the Galerkin Method in the Solution of Non-linear Axial Combustion Instability Problems in Liquid Rockets. *Combustion Science and Technology*, 4(1):269–278. 3

Appendix A

First-order eigenvalue sensitivity

In this appendix we derive the formula for the first-order sensitivity to parameter changes of the eigenvalues of a nonlinear, non-self-adjoint eigenvalue problem. Useful references are the textbooks on perturbation theory for self-adjoint linear operators by Kato (1995) and non-self-adjoint linear operators by Kirillov (2021). A detailed account of single-parameter perturbation theory of arbitrary order for non-linear, non-self-adjoint eigenvalue problems can be found in (Mensah et al., 2020) for simple eigenvalues and in (Orchini et al., 2021) for semi-simple eigenvalues, with some applications in thermoacoustics. An application of multi-parameter perturbation theory for simple eigenvalues for uncertainty quantification in thermoacoustics can be found in (Mensah et al., 2018a).

We apply single-parameter perturbation theory to the nonlinear eigenvalue problem

$$\mathbf{L}(\omega;\varepsilon)\mathbf{p} = 0 \tag{A.1}$$

The matrix $\mathbf{L}$ is a linear operator that depends nonlinearly on ω and is analytic with respect to ε. ω is the eigenvalue, ε is a parameter and $\mathbf{p}$ is the eigenvector. $(\omega_0, \mathbf{p}_0)$ is an eigenpair of Eq. (A.1) for $\varepsilon = \varepsilon_0$. It can be either simple or degenerate, provided that the degeneracy is retained after the perturbation is applied. We add a small perturbation $\Delta\varepsilon = \varepsilon - \varepsilon_0$ to the parameter ε_0. We expand the perturbed eigenvalue, ω, and the perturbed eigenvector, $\mathbf{p}$, in power series around the unperturbed eigenpair.

$$\omega(\varepsilon) = \sum_{n=0}^{\infty} \omega_n(\varepsilon - \varepsilon_0)^n = \omega_0 + \omega_1\Delta\varepsilon + O(\Delta\varepsilon^2) \tag{A.2}$$

$$\mathbf{p}(\varepsilon) = \sum_{n=0}^{\infty} \mathbf{p}_n(\varepsilon - \varepsilon_0)^n = \mathbf{p}_0 + \mathbf{p}_1\Delta\varepsilon + O(\Delta\varepsilon^2) \tag{A.3}$$

We also expand the perturbed operator, $\mathbf{L}$, in Taylor series around the unperturbed matrix/operator.

$$\mathbf{L}(\omega;\varepsilon) = \mathbf{L}(\omega_0;\varepsilon_0) + \frac{\partial \mathbf{L}(\omega_0;\varepsilon_0)}{\partial \omega}\omega_1 \Delta\varepsilon + \frac{\partial \mathbf{L}(\omega_0;\varepsilon_0)}{\partial \varepsilon}\Delta\varepsilon + O(\Delta\varepsilon^2) \tag{A.4}$$

We substitute Eqs. (A.2), (A.3) and (A.4) into Eq. (A.1).

$$\begin{aligned}\mathbf{L}(\omega;\varepsilon)\mathbf{p} = {} & \mathbf{L}(\omega_0;\varepsilon_0)\mathbf{p}_0 \\ & + \left(\mathbf{L}(\omega_0;\varepsilon_0)\mathbf{p}_1 + \frac{\partial \mathbf{L}(\omega_0;\varepsilon_0)}{\partial \omega}\omega_1\mathbf{p}_0 + \frac{\partial \mathbf{L}(\omega_0;\varepsilon_0)}{\partial \varepsilon}\mathbf{p}_0\right)\Delta\varepsilon \\ & + O(\Delta\varepsilon^2) = 0\end{aligned} \tag{A.5}$$

At order $\Delta\varepsilon^1$ (first order), we obtain

$$\mathbf{L}(\omega_0;\varepsilon_0)\mathbf{p}_1 + \frac{\partial \mathbf{L}(\omega_0;\varepsilon_0)}{\partial \omega}\omega_1\mathbf{p}_0 + \frac{\partial \mathbf{L}(\omega_0;\varepsilon_0)}{\partial \varepsilon}\mathbf{p}_0 = 0 \tag{A.6}$$

We left-multiply Eq. (A.6) by the conjugate transpose of the unperturbed left (or adjoint) eigenvector, $\mathbf{p}_0^\dagger$.

$$\mathbf{p}_0^{\dagger H}\mathbf{L}(\omega_0;\varepsilon_0)\mathbf{p}_1 + \mathbf{p}_0^{\dagger H}\frac{\partial \mathbf{L}(\omega_0;\varepsilon_0)}{\partial \omega}\omega_1\mathbf{p}_0 + \mathbf{p}_0^{\dagger H}\frac{\partial \mathbf{L}(\omega_0;\varepsilon_0)}{\partial \varepsilon}\mathbf{p}_0 = 0 \tag{A.7}$$

The first term of Eq. (A.7) is zero, regardless of $\mathbf{p}_1$. In fact,

$$(\mathbf{L}(\omega_0;\varepsilon_0))^H\mathbf{p}_0^\dagger = 0 \tag{A.8}$$

Equation (A.8) is the unperturbed adjoint eigenproblem. The formula for the first-order eigenvalue sensitivity with respect to the parameter ε is

$$\omega_1 \equiv \frac{\mathrm{d}\omega}{\mathrm{d}\varepsilon} = -\frac{\mathbf{p}_0^{\dagger H}\ \partial \mathbf{L}(\omega_0;\varepsilon_0)/\partial\varepsilon\ \mathbf{p}_0}{\mathbf{p}_0^{\dagger H}\ \partial \mathbf{L}(\omega_0;\varepsilon_0)/\partial\omega\ \mathbf{p}_0} \tag{A.9}$$

By knowing the adjoint eigenvector, we can calculate the eigenvalue sensitivity with respect to any parameter, without having to solve the perturbed eigenproblem.

Appendix B

B-spline curves

In this appendix we define the B-spline basis functions and the non-rational B-spline curves (Piegl and Tiller, 1995), and illustrate some of their properties. We then explain how to obtain the admissible displacement fields of a B-spline curve.

B.1 Definition and Properties of B-spline Basis Functions

There are a number of ways to define the B-spline basis functions. We use the recurrence formula, since it is the most useful for computer implementation.

Let $U = \{u_0, \ldots, u_m\}$ be a non-decreasing sequence of real numbers, i.e., $u_i \leq u_{i+1}$ for $i = 0, \ldots, m-1$. U is the knot vector and its elements, u_i, are called knots. The i-th B-spline basis function of degree p, denoted by $N_{i,p}(u)$, is defined as

$$N_{i,0}(u) = \begin{cases} 1 & \text{if } u_i \leq u < u_{i+1} \\ 0 & \text{otherwise} \end{cases} \tag{B.1}$$

$$N_{i,p}(u) = \frac{u - u_i}{u_{i+p} - u_i} N_{i,p-1}(u) + \frac{u_{i+p+1} - u}{u_{i+p+1} - u_{i+1}} N_{i+1,p-1}(u) \tag{B.2}$$

For $p > 0$, $N_{i,p}(u)$ is a linear combination of two basis functions of degree $p-1$. A set of basis functions is uniquely defined by the knot vector, U, and the degree, p. The half-open interval, $[u_i, u_{i+1})$, is called the i-th knot span; it can have zero length since the knots need not be distinct.

B.2 Definition and Properties of B-spline Curves

A p-th degree B-spline curve is defined as

$$\mathbf{C}(u) = \sum_{i=0}^{n} N_{i,p}(u)\mathbf{P}_i, \quad a \leq u \leq b \tag{B.3}$$

where $\mathbf{P}_i$ are the control points, and $N_{i,p}(u)$ are the p-th degree B-spline basis functions defined on the non-periodic (and in general non-uniform) knot vector

$$U = \{\underbrace{a, \ldots, a}_{p+1}, u_{p+1}, \ldots, u_{m-p-1}, \underbrace{b, \ldots, b}_{p+1}\} \tag{B.4}$$

with $m + 1$ knots. The polygon defined by the control points, $\mathbf{P}_i$, is called the control polygon.

Properties:

- $\mathbf{C}(u)$ is a piecewise polynomial curve, since $N_{i,p}(u)$ are piecewise polynomial basis functions. The number of control points (basis functions), $n + 1$, the degree, p, and the number of knots, $m + 1$, satisfy
$$m = n + p + 1 \tag{B.5}$$
A basis function of degree p spans $p + 1$ knot intervals.

- With this choice of the knot vector, Eq. (B.4), $N_{0,0}(a), \ldots, N_{p-1,0}(a) = 0$, and $N_{p,0}(a) = 1$. Therefore, $N_{0,p}(a) = 1$, and, since $N_{i,p}(a) = 0$ for $i \neq 0$, from Eq. (B.3), $\mathbf{C}(a) = \mathbf{P}_0$. Similarly, $\mathbf{C}(b) = \mathbf{P}_n$. The B-spline curve is clamped.

- $N_{i,p}(u) = 0$ outside the interval $[u_i, u_{i+p+1})$. If we shift the control point, $\mathbf{P}_i$, the curve $\mathbf{C}(u)$ is modified only in the interval $[u_i, u_{i+p+1})$.

- All the derivatives of $N_{i,p}(u)$, and $\mathbf{C}(u)$, exist in the interior of a knot span. At a knot, $N_{i,p}(u)$, and $\mathbf{C}(u)$, are $p - k$ times continuously differentiable, where k is the multiplicity of the knot. Therefore, increasing the degree increases the continuity and increasing the knot multiplicity decreases the continuity.

We use a uniform knot vector, structured as a non-decreasing sequence of natural numbers (non-negative integers). If $n = 10$, i.e., the control points are 11, and $p = 3$, $U = \{0, 0, 0, 0, 1, 2, 3, 4, 5, 6, 7, 8, 8, 8, 8\}$. Given a set of control points, and a degree, the knot vector is uniquely defined, and we can create the uniform non-rational B-spline curve.

B.3 Displacement fields

$\mathbf{P} = \{\mathbf{P}_i\}$ is a set of $n + 1$ points, the control points. In two-dimensions, each control point has two components, P_i^1 and P_i^2 or P_i^j. We are interested in the admissible displacement fields of a B-spline curve. The shape morphs in accordance with the position of the control points. The Cartesian components of the displacement fields are given by the derivative of the B-spline curve with respect to the coordinates of the position of the control points.

$$V_i(u) = \frac{\partial C^j(u)}{\partial P_i^j} = N_{i,p}(u) \tag{B.6}$$

Each displacement field has compact support (B-spline properties). We have a set of admissible normal boundary perturbations $\boldsymbol{V}_i$. The shape derivative in the direction $\boldsymbol{V}_i$ is equivalent to the shape derivative with respect to $\mathbf{P}_i$.